# TECHNICAL MEMORANDUM
## X-366

# EFFECTS OF CENTERBODY LENGTH AND NOSE SHAPE ON THE TRANSONIC CHARACTERISTICS OF LOW-FINENESS-RATIO BODIES OF REVOLUTION WITH A FLARED AFTERBODY

By Roy M. Wakefield, Stuart L. Treon,
and Earl D. Knechtel

Ames Research Center
Moffett Field, Calif.



NATIONAL AERONAUTICS AND SPACE ADMINISTRATION

WASHINGTON May 1960

NATIONAL AERONAUTICS AND SPACE ADMINISTRATION

TECHNICAL MEMORANDUM X-366

# EFFECTS OF CENTERBODY LENGTH AND NOSE SHAPE ON THE TRANSONIC CHARACTERISTICS OF LOW-FINENESS-RATIO BODIES OF REVOLUTION WITH A FLARED AFTERBODY*

By Roy M. Wakefield, Stuart L. Treon,
and Earl D. Knechtel

## SUMMARY

An investigation in a transonic wind tunnel has been conducted to determine the static aerodynamic characteristics of low-fineness-ratio flared bodies of revolution with various centerbody lengths and nose shapes which ranged from a sharp, pointed cone to a spherical segment of large radius. The effects of varying the centerbody length from 0 to 2 body diameters are shown for angles of attack from -2° to +14° at ten Mach numbers from 0.60 to 1.40. The test Reynolds number was either 0.375 million or 0.50 million, based upon the cylindrical-body diameter.

## INTRODUCTION

Demand for aerodynamic data for low-fineness-ratio bodies of revolution at transonic speeds stems not only from interest in atmosphere-entry vehicles and aircraft escape capsules, but also from an awareness that the stability of such bodies can vary greatly in the transonic speed range. An experimental investigation of a few specific low-fineness-ratio bodies at transonic speeds is reported in reference 1.

The present report is one of a series presenting the results of an investigation being conducted at the Ames Research Center to determine the effects of systematic changes in model geometry on the aerodynamic characteristics of low-fineness-ratio bodies at transonic speeds. References 2, 3, 4, and 5 present the results of four phases of the investigation which have been completed. In reference 2, the effectiveness of a flared afterbody is compared with that of blunt cruciform fins for stabilizing a cylindrical body with a blunt conical nose. In references 3 and 4 are

*Title, Unclassified

[redacted]

presented the effects of systematic changes in afterbody flare geometry for cylinder-flare models with either a blunt conical nose or an oblate ellipsoidal nose. In reference 5 are reported the effects of nose shape for a body with a cylindrical or flared afterbody. In the present report are the results of an investigation of the effects of centerbody length on the static aerodynamic characteristics at transonic speeds of a low-fineness-ratio body of revolution with a flared afterbody and various nose shapes. The centerbody lengths of the models were 0, 1, and 2 body diameters, and the nose shapes were a sharp cone, a blunted cone, four semi-ellipsoids of varying degrees of bluntness, and a spherical segment of large radius.

The results are presented without detailed discussion.



## NOTATION

$B$ model base area

$C_{A_b}$ base axial-force coefficient, $\dfrac{(p_\infty - p_b)B}{qS}$

$C_{A_f}$ forebody axial-force coefficient, $\dfrac{\text{forebody axial force}}{qS}$

$C_m$ pitching-moment coefficient about nose-body juncture, $\dfrac{\text{pitching moment}}{qSd}$

$C_N$ normal-force coefficient, $\dfrac{\text{normal force}}{qS}$

$\dfrac{C_N}{\alpha}$ slope of the straight line drawn from $C_N$ at $\alpha = 0^\circ$ to any point on the $C_N$ vs. $\alpha$ curve

c.p. center-of-pressure location, body diameters ahead of moment reference shown in figure 1

$d$ cylindrical-body diameter

$M$ Mach number

$p_b$ base pressure

$p_\infty$ test-section static pressure

[redacted]

$q$ dynamic pressure

$S$ cross-sectional area of cylindrical centerbody

$\alpha$ angle of attack, deg

Model Component Designations

$N_X$ nose, with subscript denoting nose profile shown in figure 1

$B_X$ cylindrical centerbody, with subscript denoting length in body diameters

A
3
3
0

$F_{20-4}$ flared afterbody, semivertex angle = 20° and ratio of flare base area to cylindrical body cross-sectional area = 4

## APPARATUS AND MODELS

The investigation was conducted in the Ames 2- by 2-Foot Transonic Wind Tunnel, which is of the closed-circuit, variable-pressure type. This facility (ref. 6) has a perforated test section which permits continuous choke-free operation from subsonic speeds up to a Mach number of 1.4.

The 21 models were combinations of the 3 body and flare arrangements and the 7 nose shapes shown in figure 1. The centerbodies were 0, 1, and 2 body diameters in length. The noses included a sharp cone, a blunted cone, a spherical segment of large radius, and a series of four semiellipsoidal noses for which the ratios of lengths of longitudinal axes to transverse axes of the complete ellipsoids were 0.25, 0.50, 1.0, and 2.0 (fig. 1). Each model had a 20° flared afterbody.

The models were mounted in the test section on a sting-supported strain-gage balance which was shielded by a metal shroud as shown in figure 1. The position of the shroud with respect to the base of the flare was the same for all models. Photographs of three of the models installed in the test section are shown in figure 2.

## TESTS AND DATA REDUCTION

The investigation was conducted at ten Mach numbers from 0.6 to 1.4 at angles of attack from approximately -2° to +14°. The procedure for traversing the angle-of-attack range was dependent upon the type of flow anticipated for the various models. For all models at all test Mach numbers, the angle of attack was decreased from an initial 0° to approximately -2°, then increased progressively to about +14°. For models with noses $N_6$ through $N_{10}$, the angle of attack at Mach numbers greater than 0.90 was then decreased from +14° to -2° to determine the possible occurrence of flow hysteresis of the type reported in reference 7 for blunt-nosed bodies. The Reynolds number based on the cylindrical body diameter was 0.375 million for models with the $N_1$ and $N_2$ noses and 0.50 million for models with the $N_6$, $N_7$, $N_8$, $N_9$, and $N_{10}$ noses.

In order to restrict the variation of transition location, boundary-layer trip wires were affixed to the foreparts of the models as shown in figure 1. The models with noses $N_1$ and $N_2$ had wires located on the noses. The models with noses $N_6$ through $N_{10}$ and centerbody lengths of 1 or 2 diameters had wires located on the cylindrical bodies; whereas the models without centerbodies were tested without trip wires. The effectiveness of the trip wires was determined from flow visualization studies, employing shadowgraphs and the technique of reference 8, on various models at the test Reynolds numbers. On the models with the $N_1$ and $N_2$ noses, the flow became turbulent ahead of or at the trip wires.[1] On the models with noses $N_6$ through $N_{10}$, the flow was either: (1) attached, with transition occurring ahead of or at the trip wires, (2) attached behind a small separation bubble in the vicinity of the nose-body juncture, becoming turbulent ahead of or in the region of attachment, or (3) fully separated from the vicinity of the nose-body juncture.

A330

The axial forces were resolved to forebody and base coefficients. For the forebody coefficients, the measured axial forces were adjusted to account for the difference between the base pressures and an assumed condition of free-stream static pressure acting at the base of the model.

The results of reference 10 for models with cylindrical afterbodies and of reference 11 for models with flared afterbodies indicate that the presence of a sting may have a significant effect on base axial force. However, there is evidence in references 7 and 10 that the forebody axial force is not significantly affected. The magnitude of the sting interference on base axial force is not known for the present models.

The angles of attack have been corrected for elastic deflection of the balance and sting under aerodynamic loads. Stream angularity corrections are negligible.

---

[1]On the models with the $N_1$ and $N_2$ noses, with a centerbody length of 2 diameters, there appeared to be a region of laminar flow approximately 1/4-body diameter in length immediately behind the nose-body juncture, although the flow over the model noses appeared to be turbulent behind the trip wires. The phenomenon of a turbulent boundary layer reverting to a laminar boundary layer in the presence of a strong expansion is discussed in reference 9.

Although the model base area was 0.85 percent of the cross-sectional area of the test section, no corrections were made for possible interference effects of the perforated test-section walls. Such interference effects are believed to be relatively small, in view of the results of transonic tests of various sizes of sharp- and blunt-nosed bodies reported in the appendix to reference 12.

In addition to the possible systematic errors from neglecting some of the above corrections, certain random errors exist which influence the precision, or repeatability, of the results. The precision of the data was determined by the method of reference 13 and the average deviations in values of Mach number, angle of attack, and aerodynamic coefficients presented herein were found to be approximately as follows:

| | | | |
|---|---|---|---|
| $M$ | $\pm 0.003$ | $C_m$ | $\pm 0.03$ |
| $\alpha$ | $\pm 0.05^{\circ}$ | $C_{A_f}$ | $\pm 0.02$ |
| $C_N$ | $\pm 0.02$ | $C_{A_b}$ | $\pm 0.01$ |

## RESULTS

The variations with angle of attack of coefficients of normal force, pitching moment, forebody axial force, and base axial force are presented in figures 3 to 9 for the various models and Mach numbers of this investigation. Results are presented for both increasing and decreasing angles of attack for those models and Mach numbers for which hysteresis loops appear in the variations of aerodynamic coefficients with angle of attack (in many cases in the figures data points for decreasing $\alpha$ are coincident with those for increasing $\alpha$). This hysteresis phenomenon, which is associated with regions of separated flow, has been shown in reference 7 to be a common and undesirable feature of transonic flow over blunt-nosed bodies, since the introduction into the pitching cycle of the energy represented by the hysteresis loop may lead to large pitching oscillations.

In figures 10 and 11, respectively, are summarized the variations with Mach number of $C_N/\alpha$ and c.p. location at three selected angles of attack. In figure 12 are presented the forebody and base axial-force coefficients at $0^{\circ}$ angle of attack.

Shadowgraphs presented in figure 13 show the effects of centerbody length on the flow patterns for models with blunt noses $N_6$ and $N_8$. For models with the bluntest ellipsoidal nose ($N_6$), the flow was attached on the zero and two diameter centerbody configurations and was separated on the model with one diameter centerbody (fig. 13(a)). The flow patterns shown for models with the hemispherical nose ($N_8$) are typical of models with the less blunt noses. For the three models with the $N_8$ nose, the flow was attached, the principal differences in the flow patterns being in the shape of the shock wave associated with the flared afterbody (fig. 13(b)).

Ames Research Center
National Aeronautics and Space Administration
Moffett Field, Calif., Feb. 8, 1960

REFERENCES

1. Fisher, Lewis R., Keith, Arvid R., Jr., and DiCamillo, Joseph R.: Aerodynamic Characteristics of Some Families of Blunt Bodies at Transonic Speeds. NASA MEMO 10-28-58L, 1958.

2. Knechtel, Earl D., Treon, Stuart L., and Wakefield, Roy M.: Transonic Static Aerodynamic Characteristics of a Blunt Cone-Cylinder Body With Flared Afterbody or Blunt Cruciform Fins. NASA TM X-40, 1959.

3. Wakefield, Roy M., Knechtel, Earl D., and Treon, Stuart L.: Transonic Static Aerodynamic Characteristics of a Blunt Cone-Cylinder Body With Flared Afterbodies of Various Angles and Base Areas. NASA TM X-106, 1959.

4. Knechtel, Earl D., Wakefield, Roy M., and Treon, Stuart L.: Transonic Static Aerodynamic Characteristics of a Low-Fineness-Ratio Body of Revolution Having a Blunt Ellipsoidal Nose and Flared Afterbodies of Various Angles and Base Areas. NASA TM X-113, 1959.

5. Treon, Stuart L., Wakefield, Roy M., and Knechtel, Earl D: Effects of Nose Shape and Afterbody Flare on the Transonic Characteristics of a Low-Fineness-Ratio Body of Revolution. NASA TM X-164, 1960.

6. Spiegel, Joseph M., and Lawrence, Leslie F.: A Description of the Ames 2- by 2-Foot Transonic Wind Tunnel and Preliminary Evaluation of Wall Interference. NACA RM A55I21, 1956.

7. Reese, David E., Jr., and Wehrend, William R., Jr.: An Investigation of the Static and Dynamic Aerodynamic Characteristics of a Series of Blunt-Nosed Cylinder-Flare Models at Mach Numbers From 0.65 to 2.20. NASA TM X-110, 1959.

8. Main-Smith, J. D.: Chemical Solids as Diffusible Coating Films for Visual Indications of Boundary-Layer Transition in Air and Water. R. & M. No. 2755, British, A.R.C., 1954.

9. Sternberg, Joseph: The Transition From a Turbulent to a Laminar Boundary Layer. B.R.L. Rep. 906.

10. Lee, George, and Summers, James L.: Effects of Sting-Support Interference on the Drag of an Ogive-Cylinder Body With and Without a Boattail at 0.6 to 1.4 Mach Number. NACA RM A57I09, 1957.

11. Reese, David E., Jr., and Wehrend, William R., Jr.: Effects of Sting-Support Interference on the Base Pressures of a Model Having a Blunt-Nosed Cylinder Body and a Conical Flare at Mach Numbers From 0.65 to 2.20. NASA TM X-161, 1960.

12. Treon, Stuart L.: The Effect of Nose Shape on the Static Aerodynamic Characteristics of Ballistic-Type Missile Models at Mach Numbers From 0.6 to 1.4. NASA MEMO 5-17-59A, 1959.

13. Beers, Yardley: Introduction to the Theory of Error. Addison-Wesley Pub. Co., Cambridge, Mass., 1953.

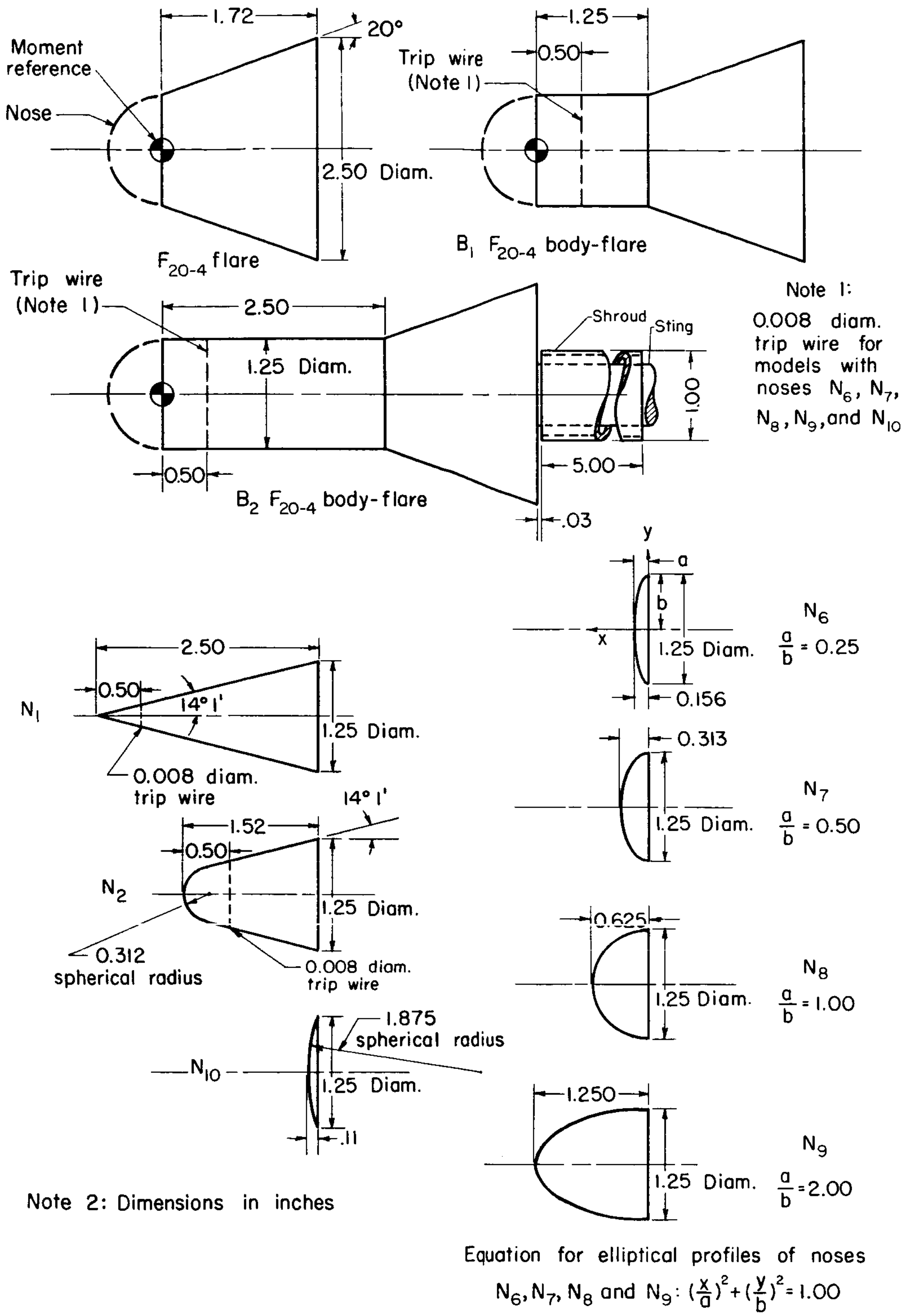


Figure 1.- Sketches and dimensions of models and components.

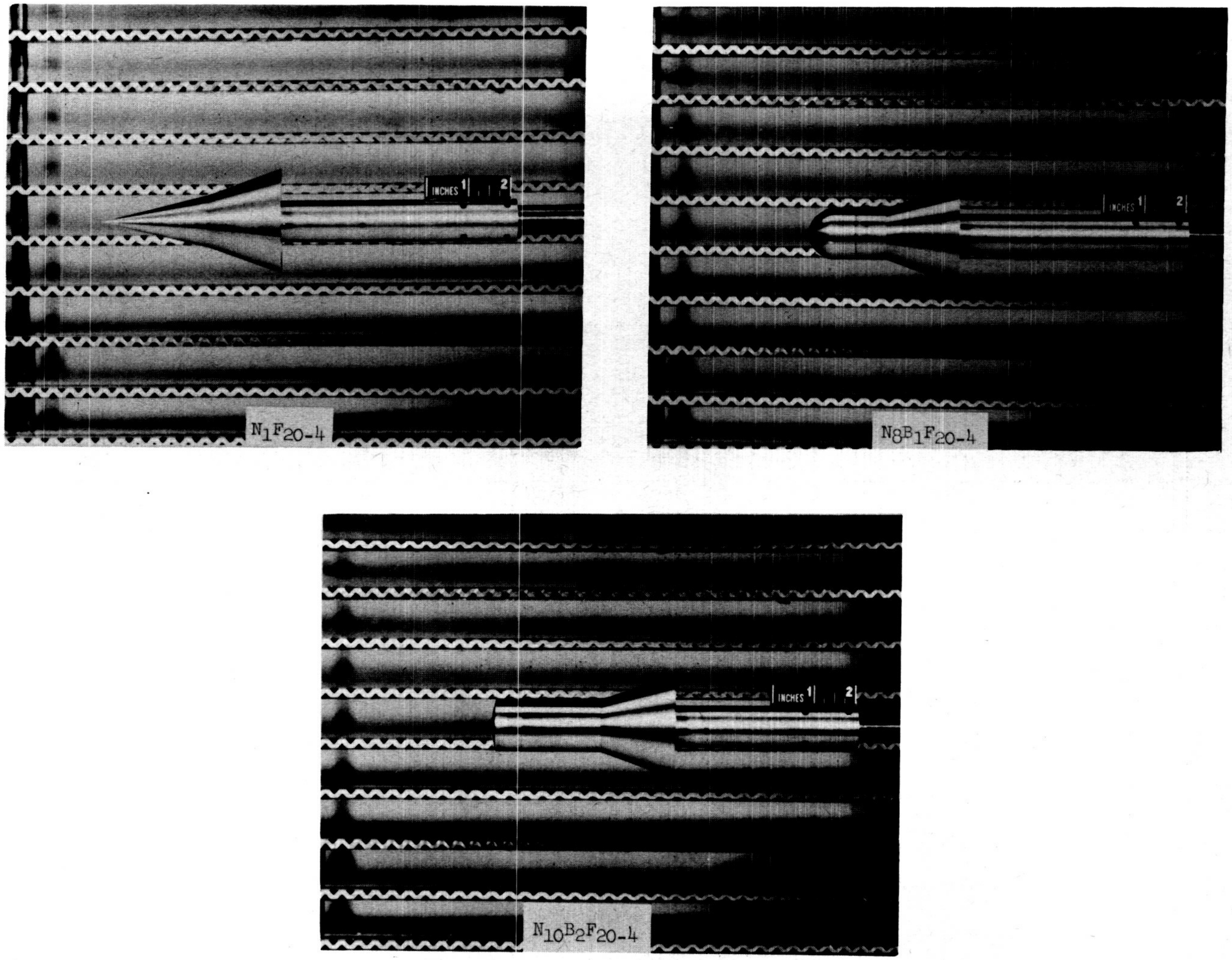


Figure 2.- Models installed in the test section of the Ames 2- by 2-Foot Transonic Wind Tunnel.

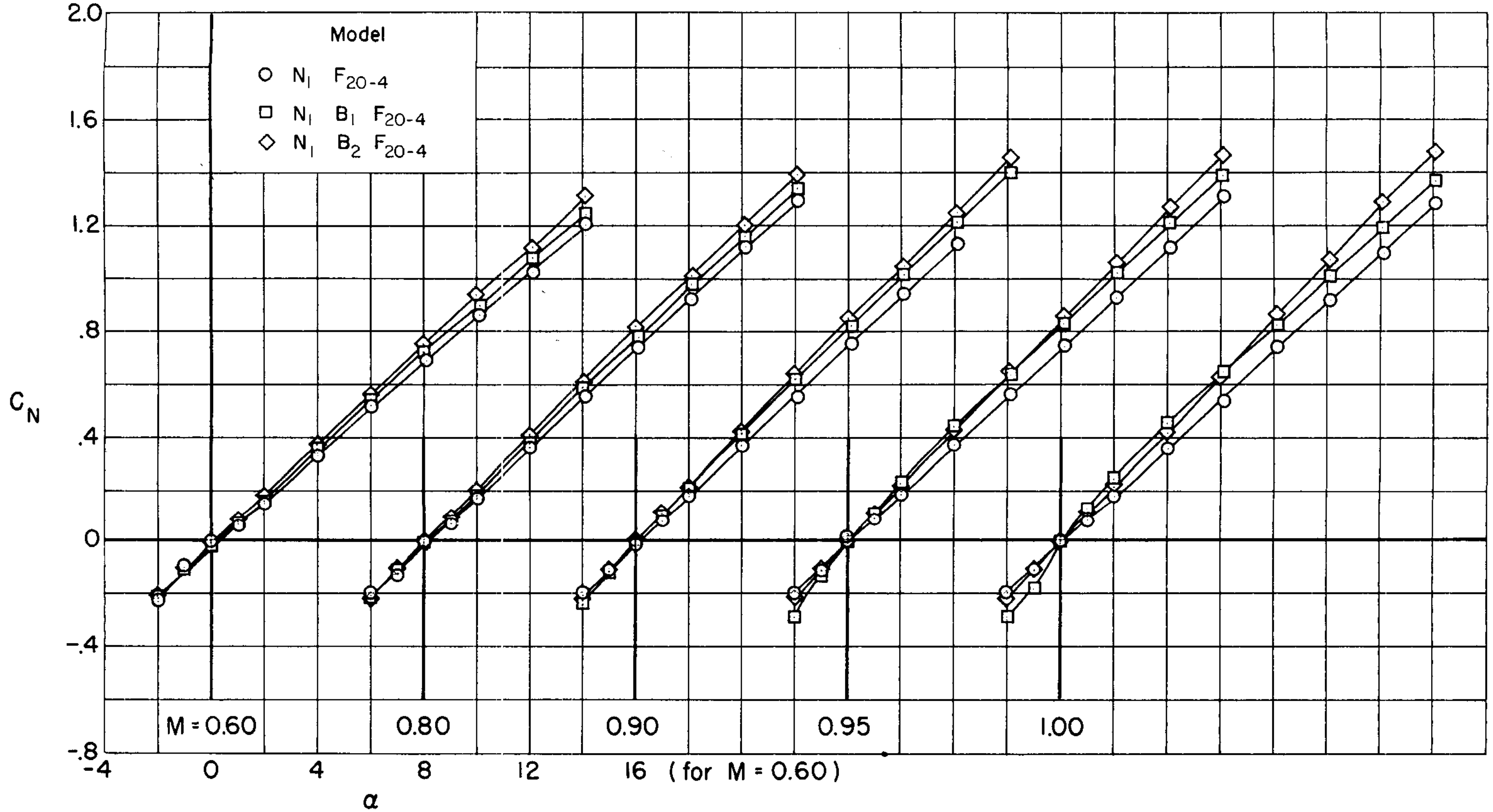


(a) Normal-force coefficient; M = 0.60 to 1.00.

Figure 3.- Static longitudinal aerodynamic coefficients for models with the $N_1$ nose.

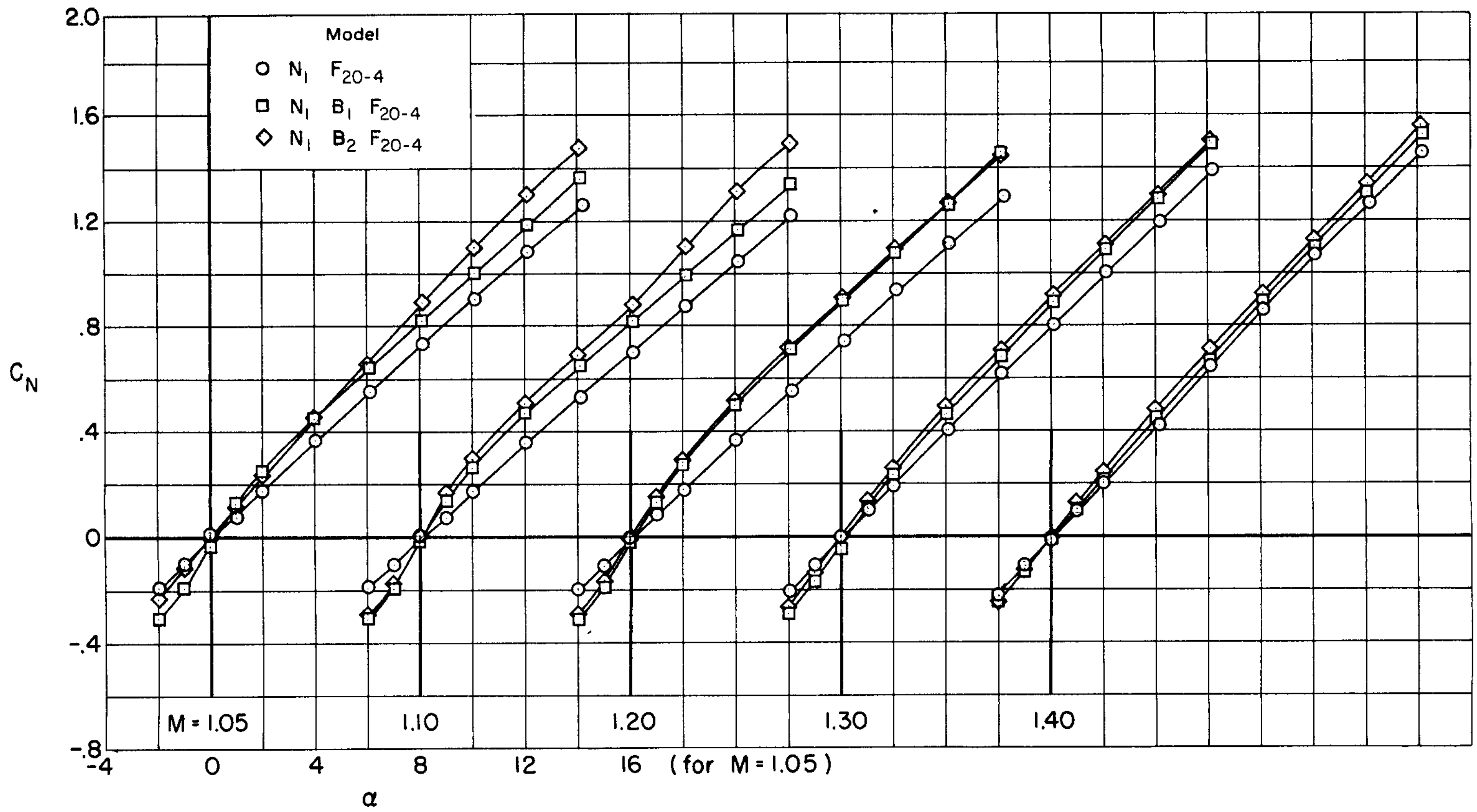


(b) Normal-force coefficient; M = 1.05 to 1.40.

Figure 3.- Continued.

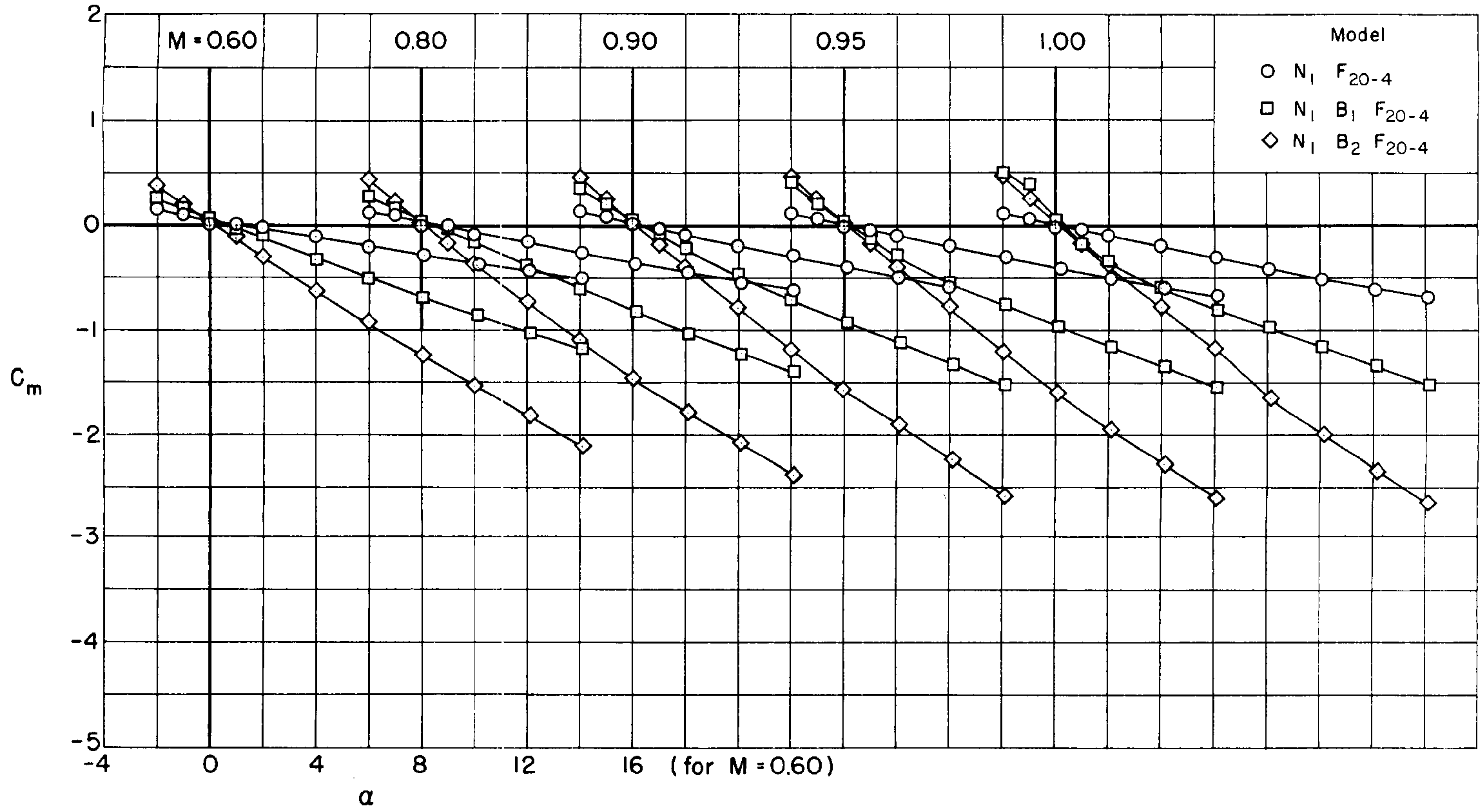


(c) Pitching-moment coefficient; M = 0.60 to 1.00.

Figure 3.- Continued.

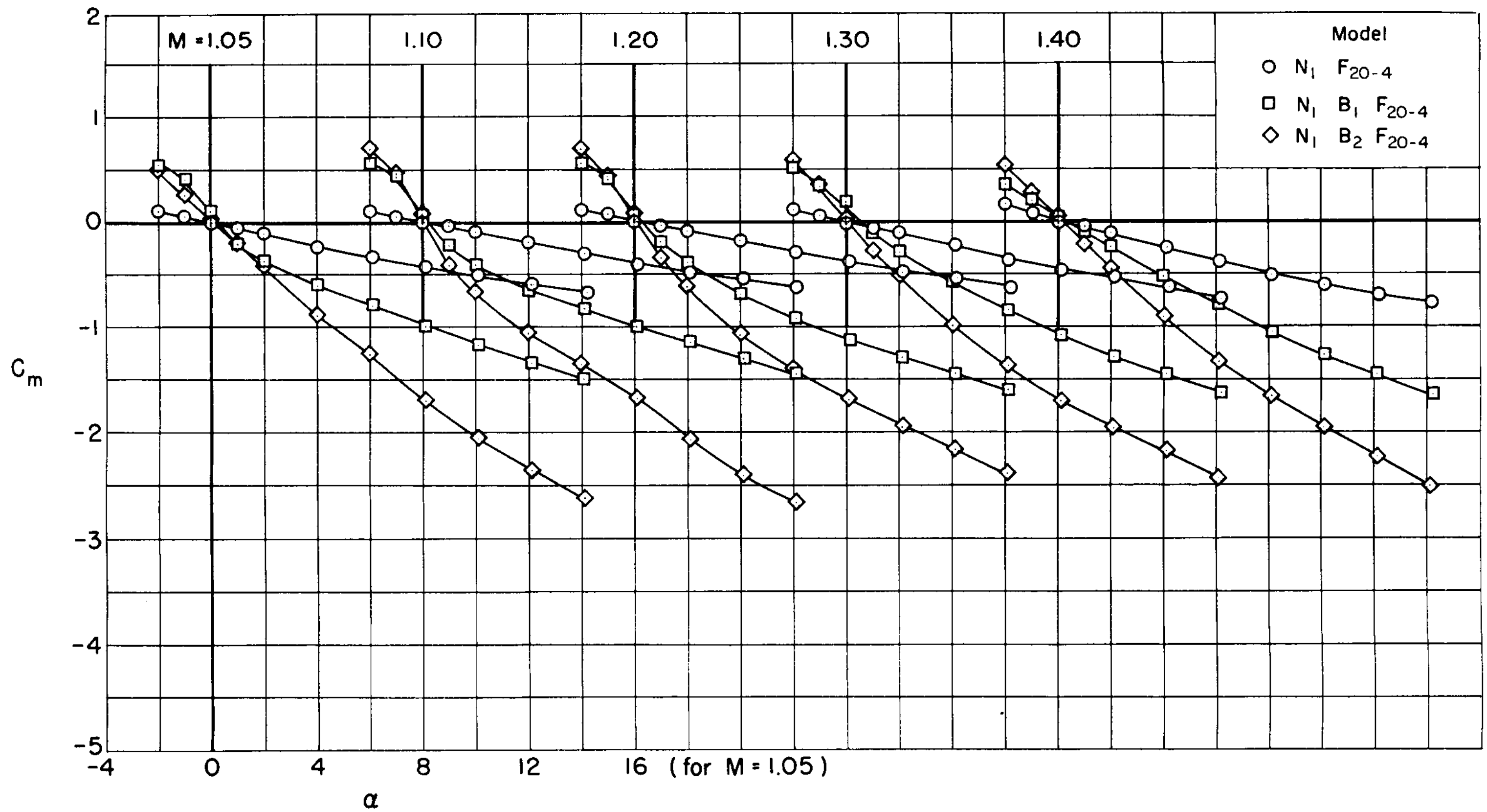


(d) Pitching-moment coefficient; M = 1.05 to 1.40.

Figure 3.- Continued.

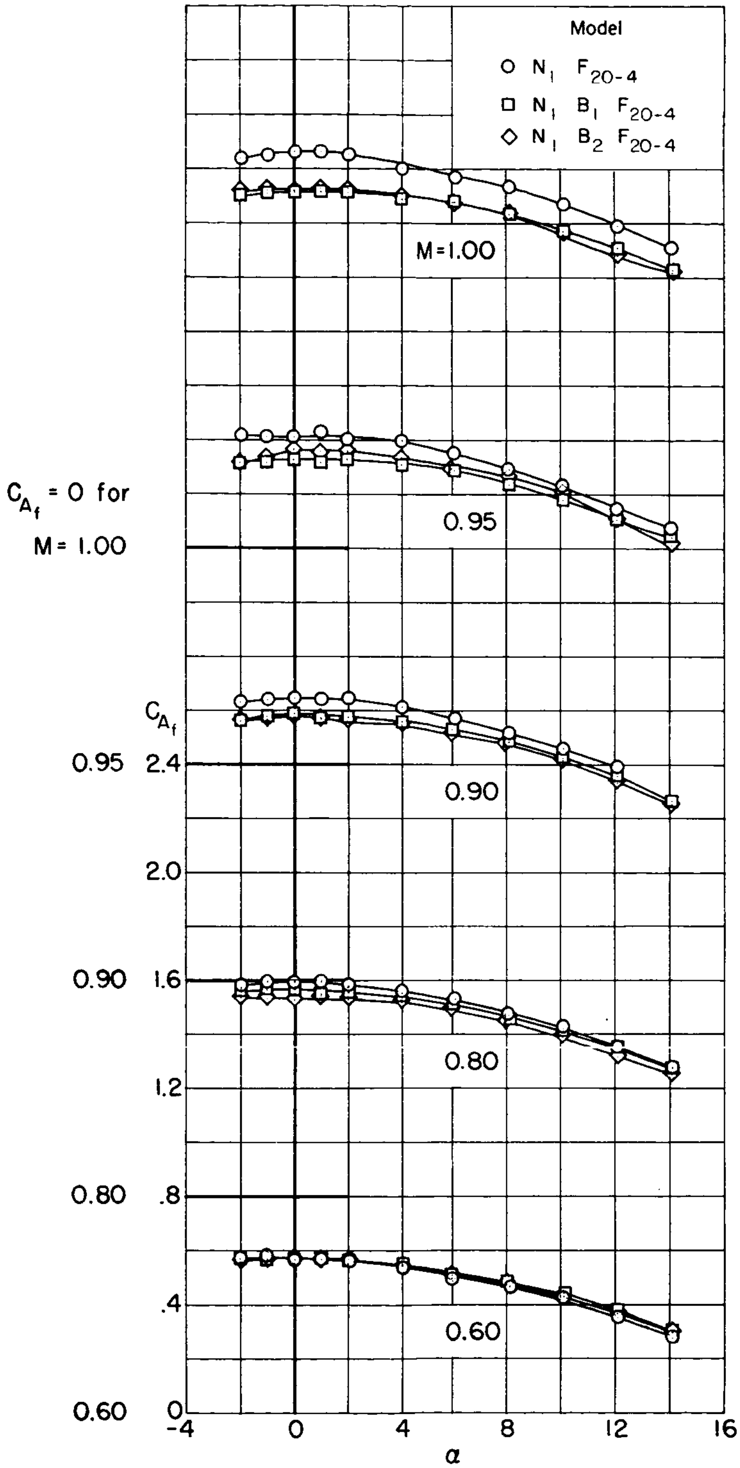


(e) Forebody axial-force coefficient; M = 0.60 to 1.00.

Figure 3.- Continued.

[redacted]

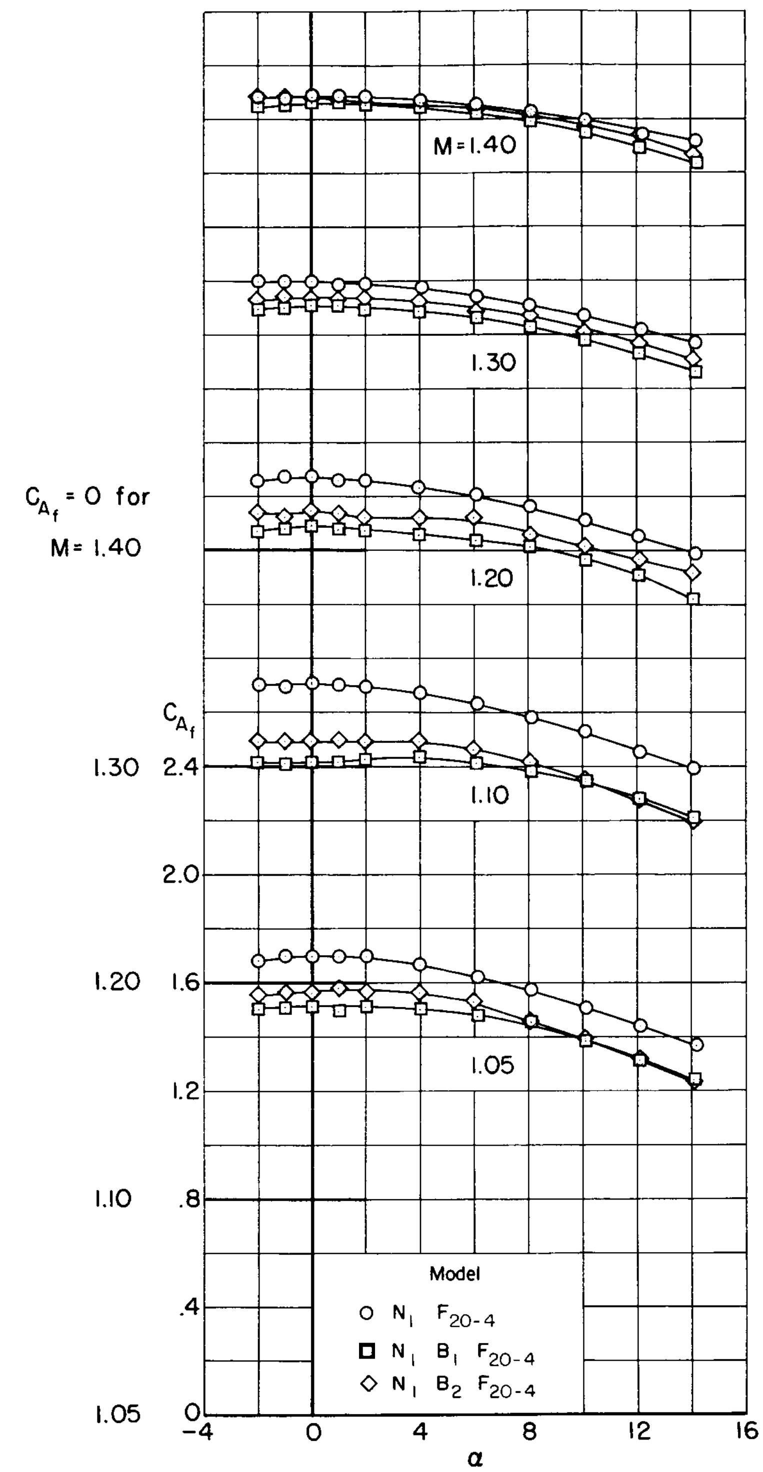


(f) Forebody axial-force coefficient; M = 1.05 to 1.40.

Figure 3.- Continued.

[redacted]

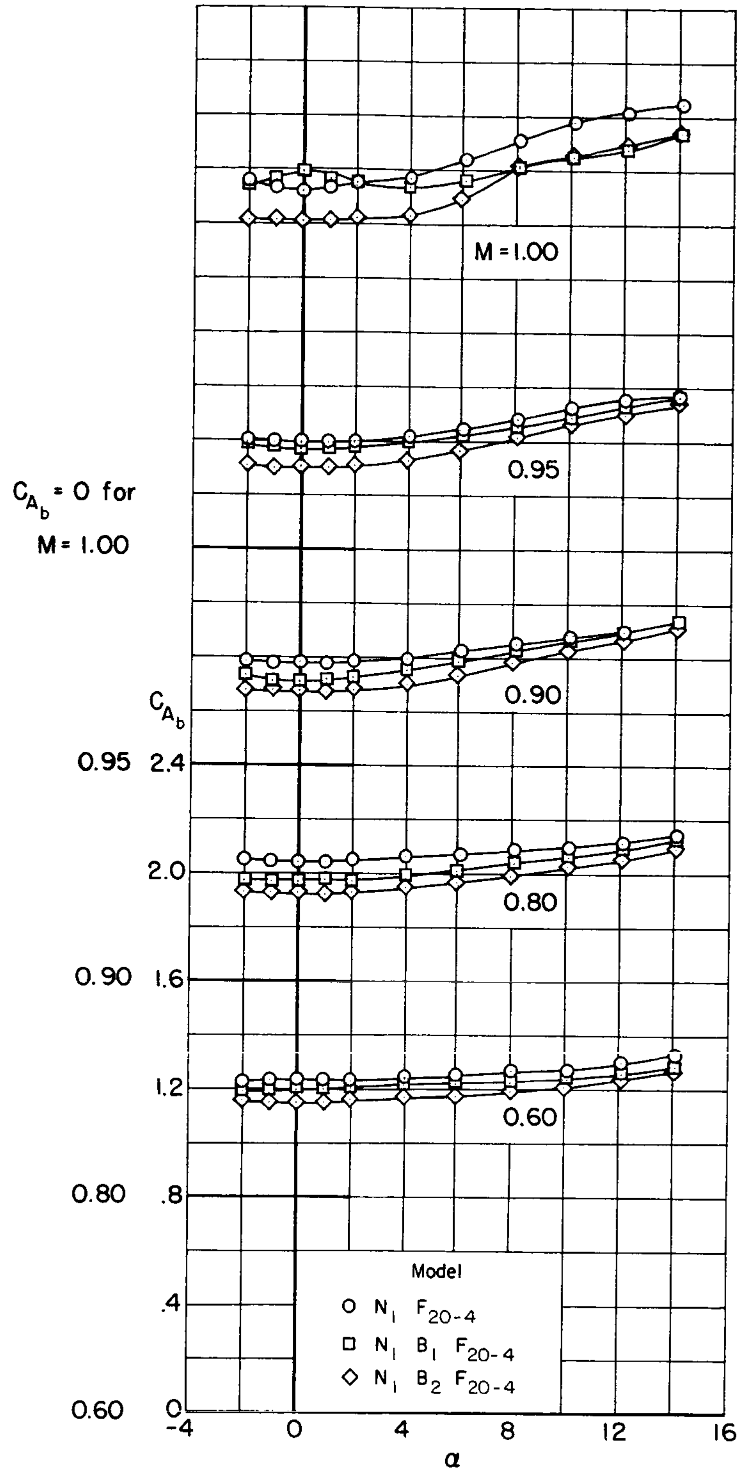


(g) Base axial-force coefficient; M = 0.60 to 1.00.

Figure 3.- Continued.

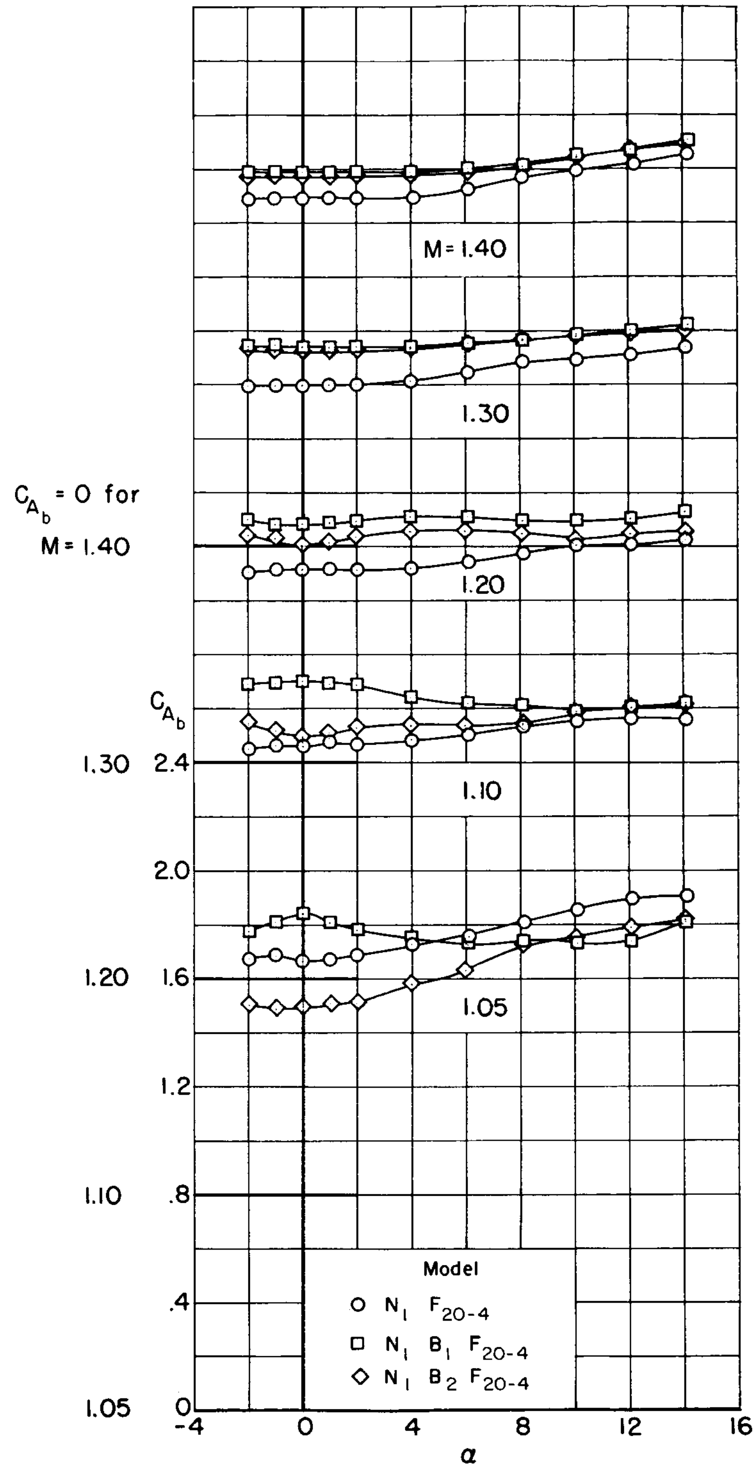


(h) Base axial-force coefficient; M = 1.05 to 1.40.

Figure 3.- Concluded.

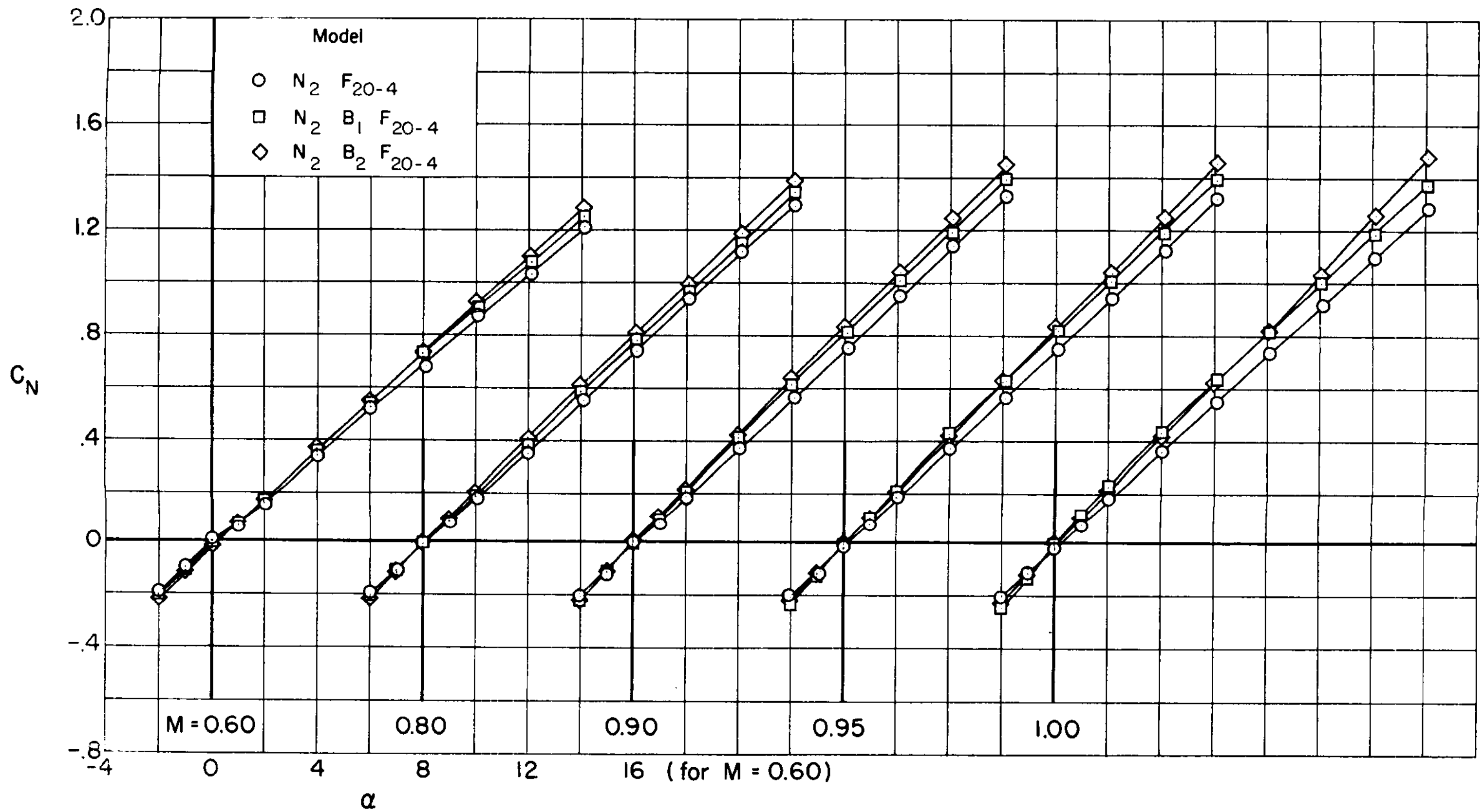


(a) Normal-force coefficient; M = 0.60 to 1.00.

Figure 4.- Static longitudinal aerodynamic coefficients for models with the N2 nose.

[redacted]

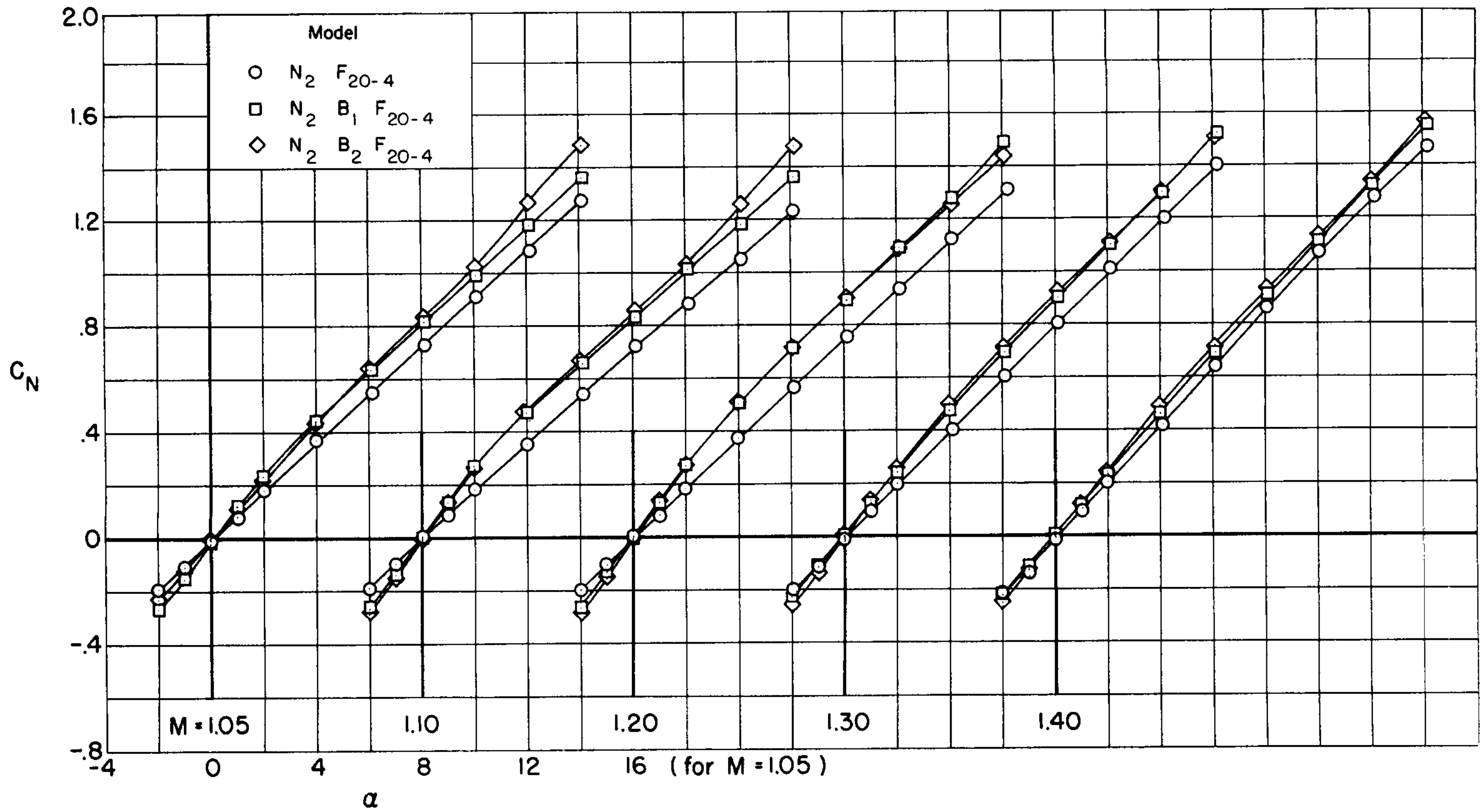


(b) Normal-force coefficient; M = 1.05 to 1.40.

Figure 4.- Continued.

[redacted]

A330

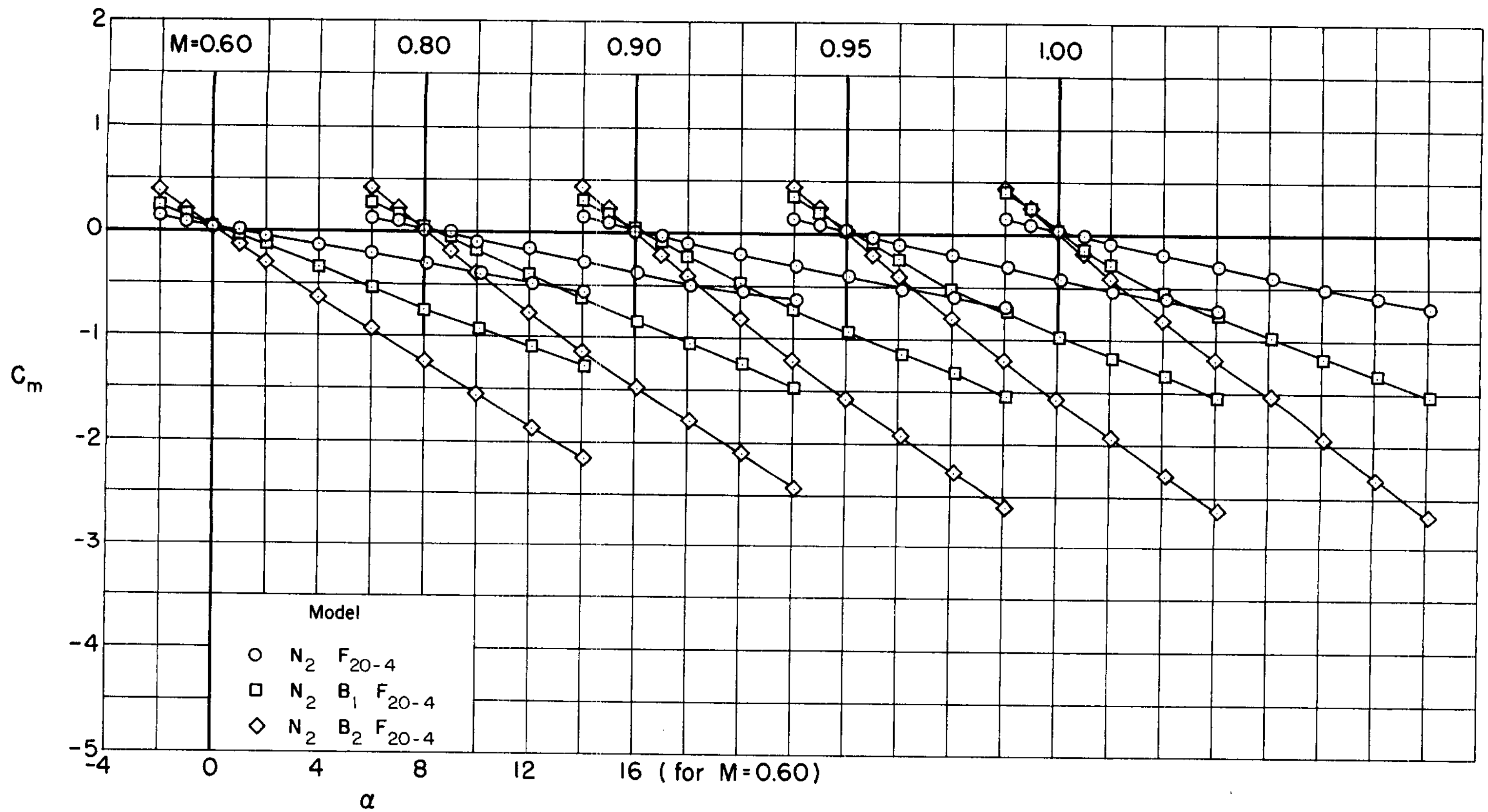


(c) Pitching-moment coefficient; M = 0.60 to 1.00.

Figure 4.- Continued.

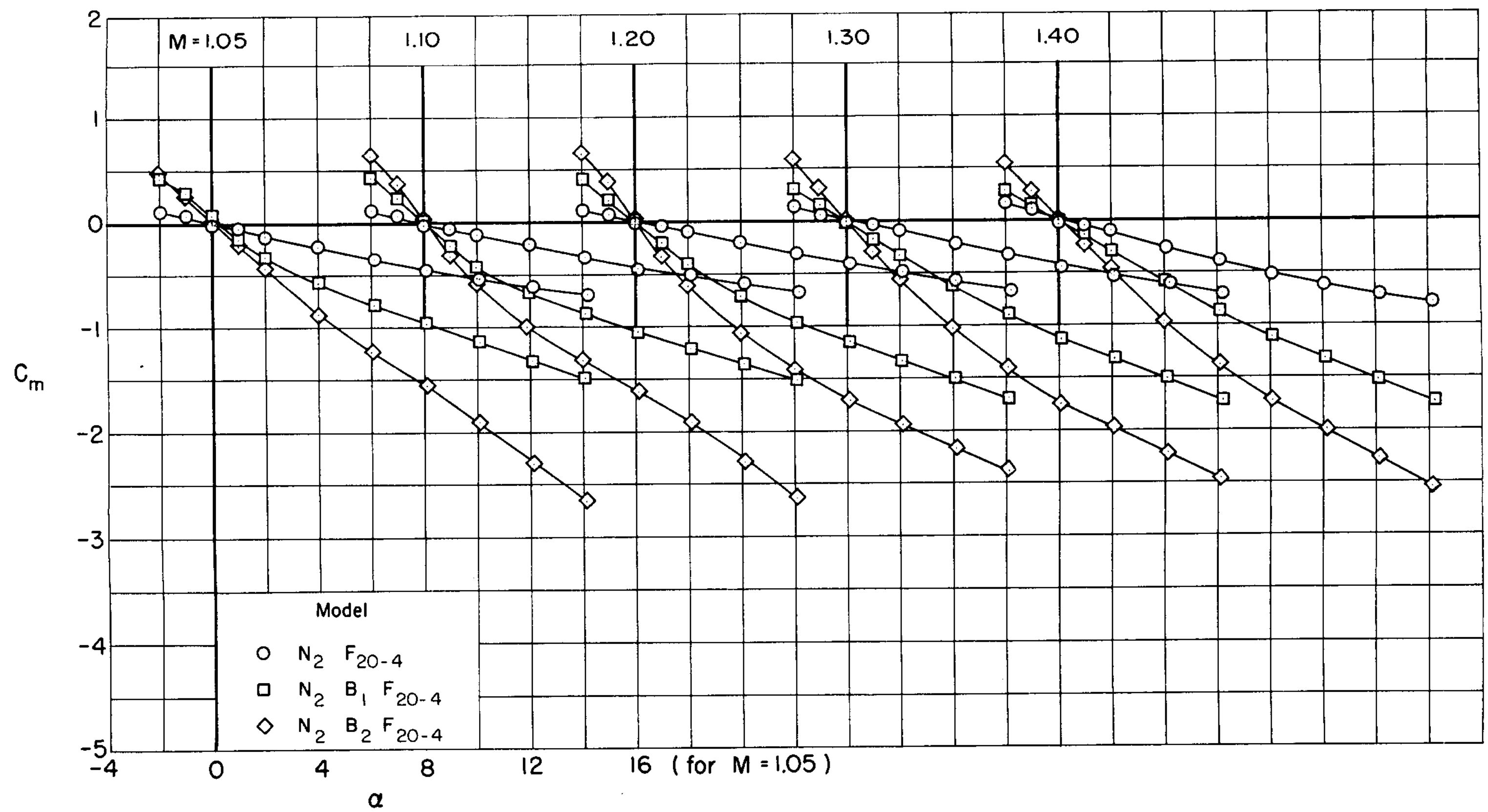


(d) Pitching-moment coefficient; M = 1.05 to 1.40.

Figure 4.- Continued.

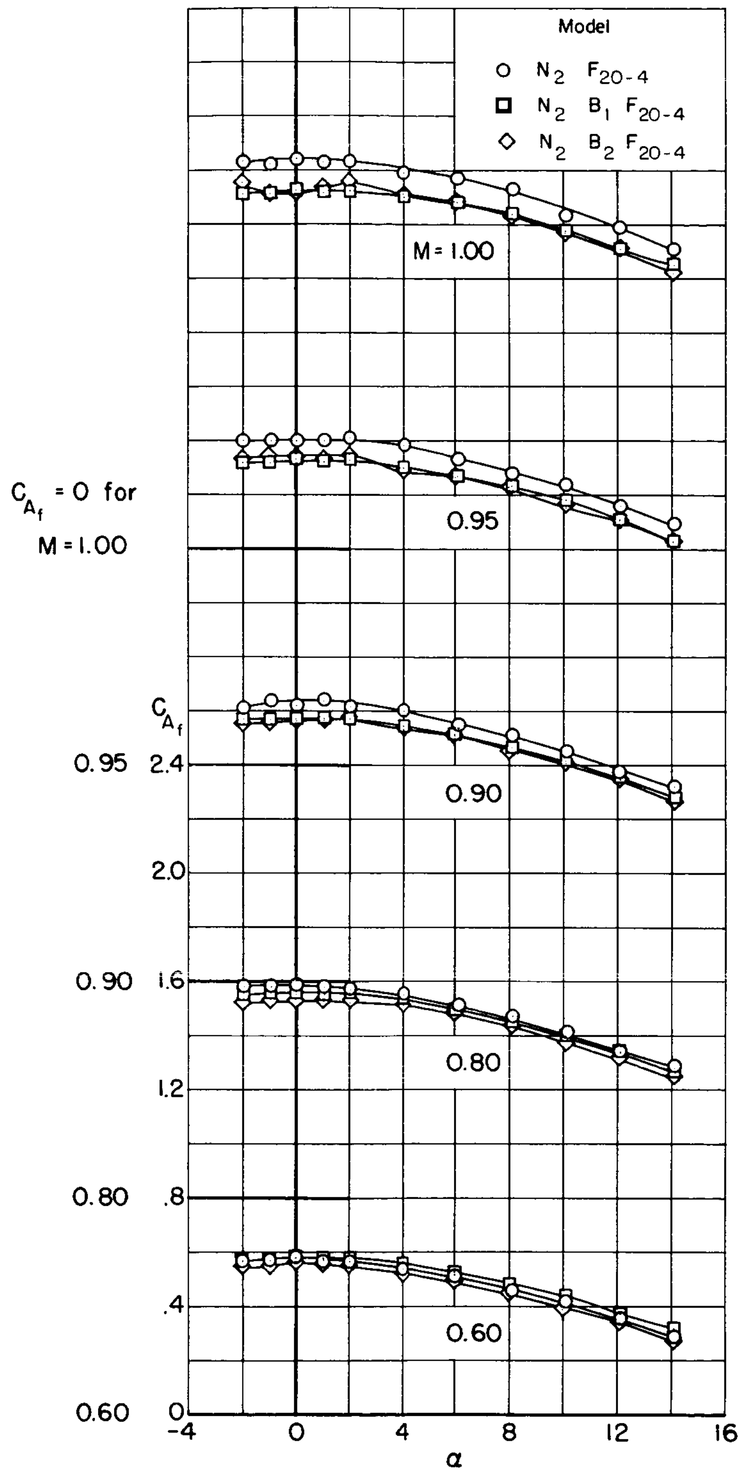


(e) Forebody axial-force coefficient; M = 0.60 to 1.00.

Figure 4.- Continued.

[redacted]

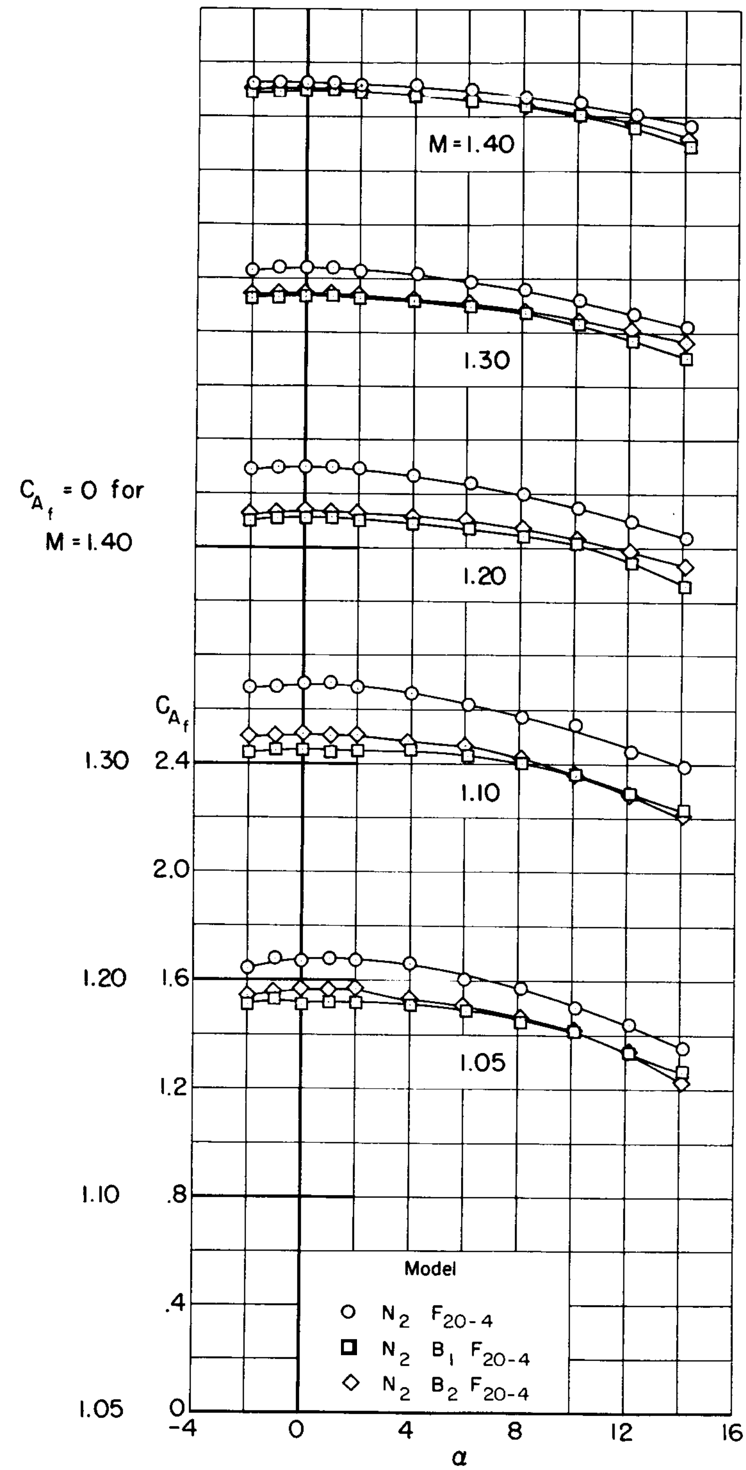


(f) Forebody axial-force coefficient; M = 1.05 to 1.40.

Figure 4.- Continued.

[redacted]

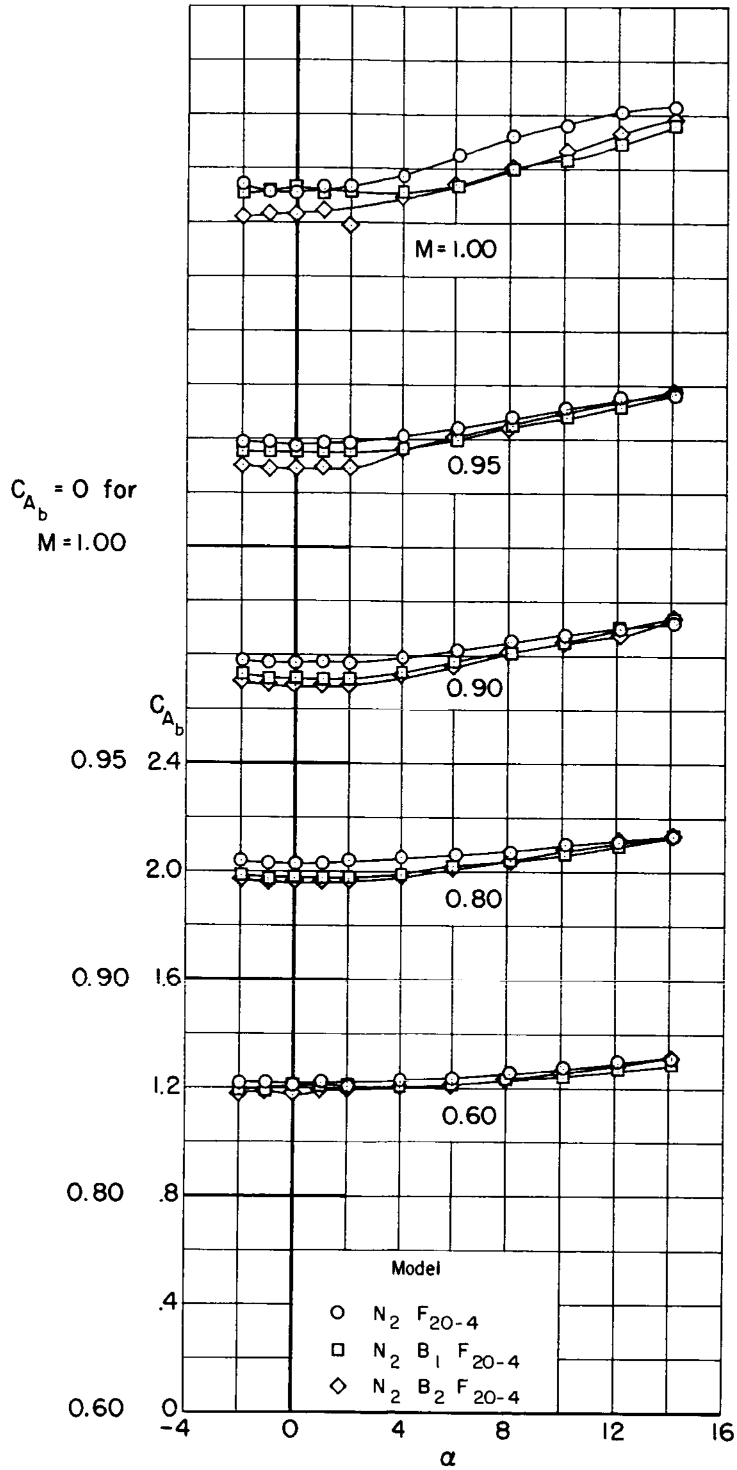


(g) Base axial-force coefficient; M = 0.60 to 1.00.

Figure 4.- Continued.

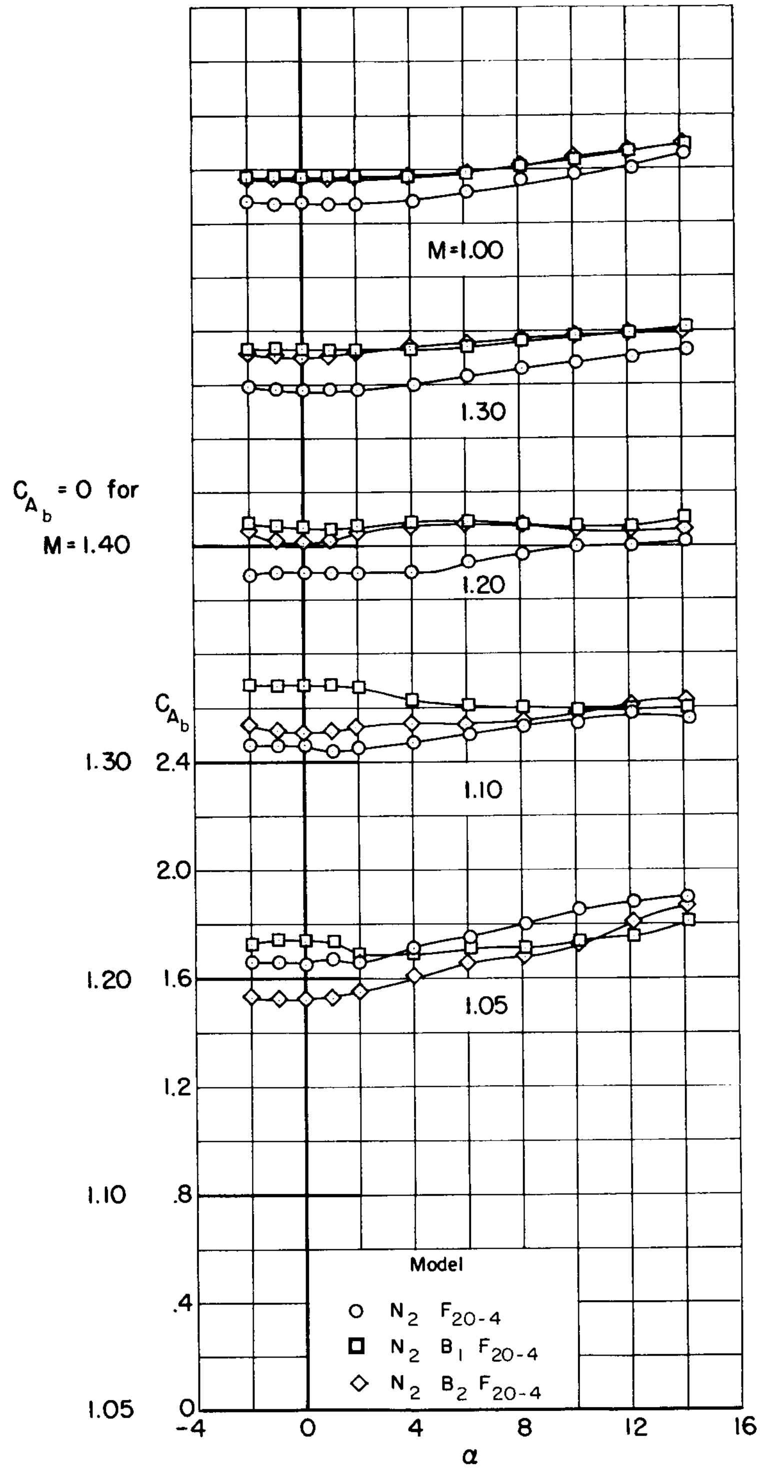


(h) Base axial-force coefficient; M = 1.05 to 1.40.

Figure 4.- Concluded.

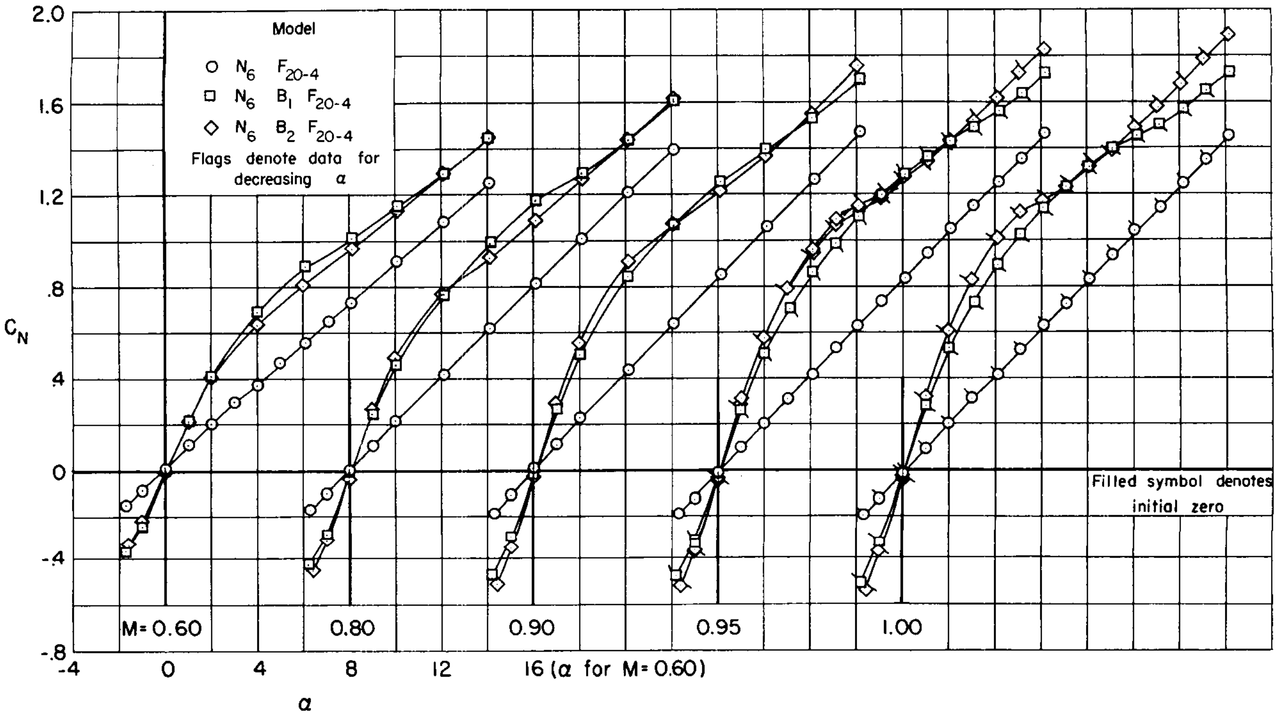


(a) Normal-force coefficient; M = 0.60 to 1.00.

Figure 5.- Static longitudinal aerodynamic coefficient for models with the $N_6$ nose.

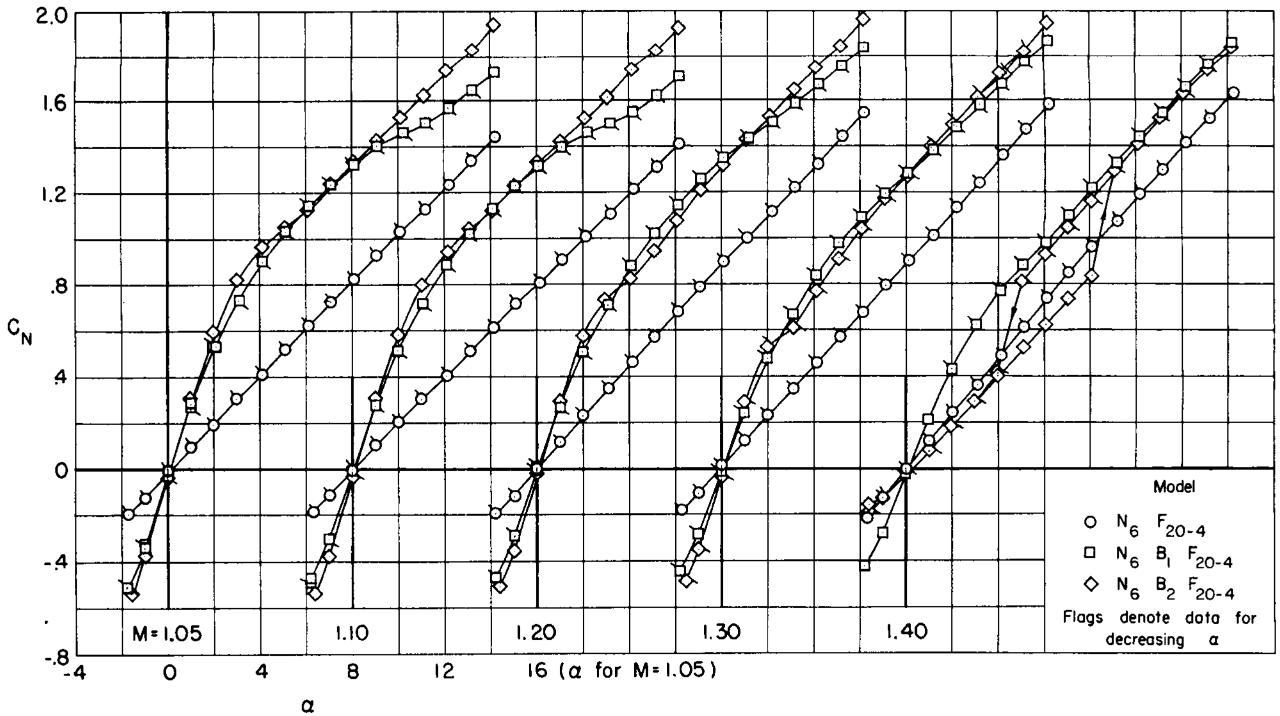


(b) Normal-force coefficient; M = 1.05 to 1.40.

Figure 5.- Continued.

A330

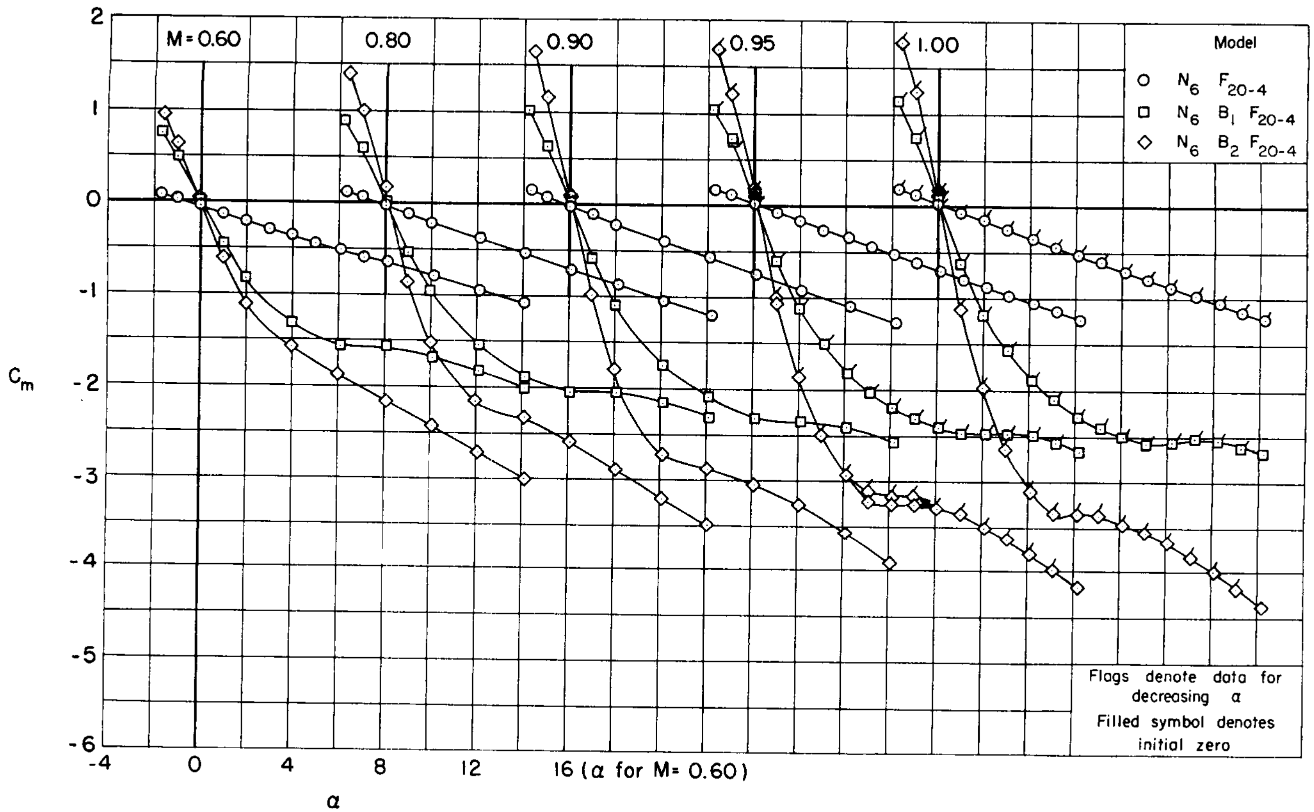


(c) Pitching-moment coefficient; M = 0.60 to 1.00.

Figure 5.- Continued.

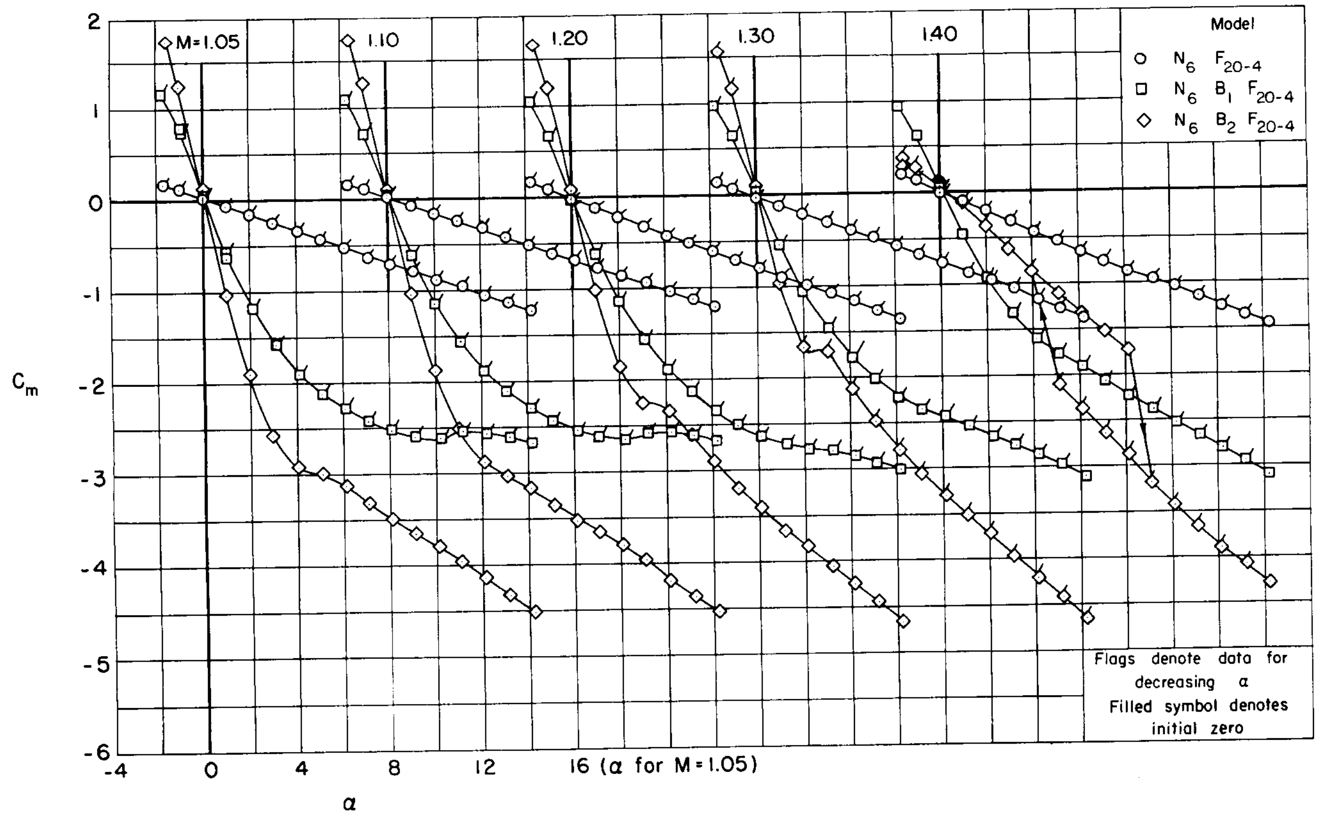


(d) Pitching-moment coefficient; M = 1.05 to 1.40.

Figure 5.- Continued.

[redacted]



A
3
3
0

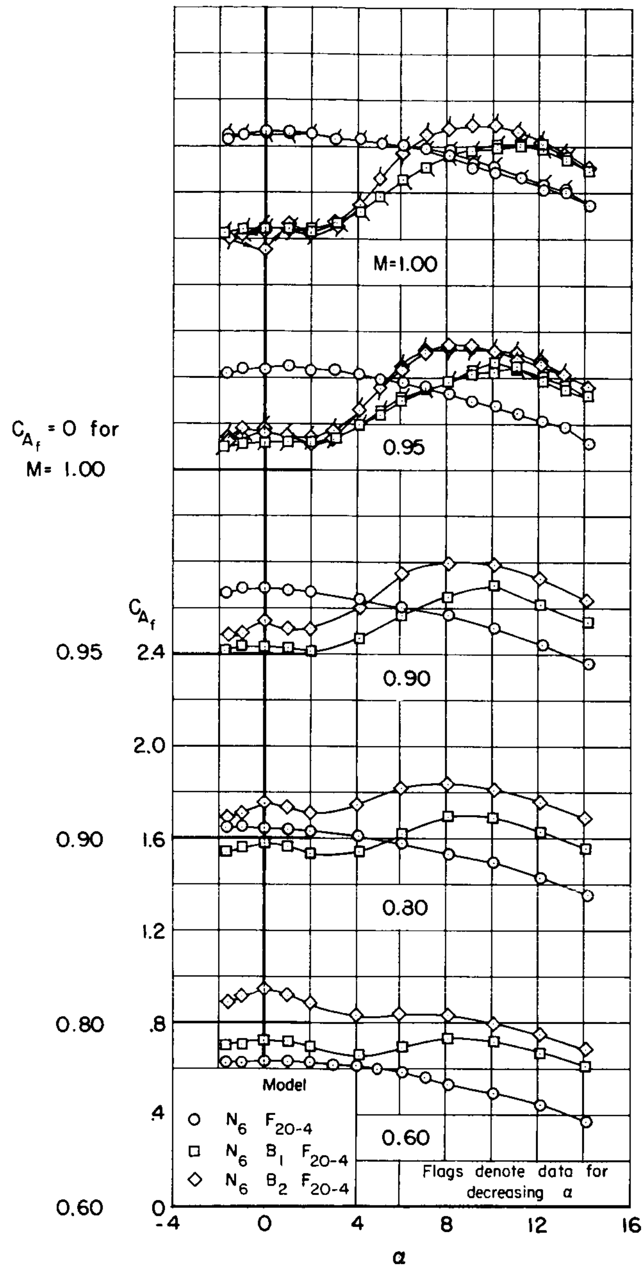


(e) Forebody axial-force coefficient; M = 0.60 to 1.00.

Figure 5.- Continued.

[redacted]

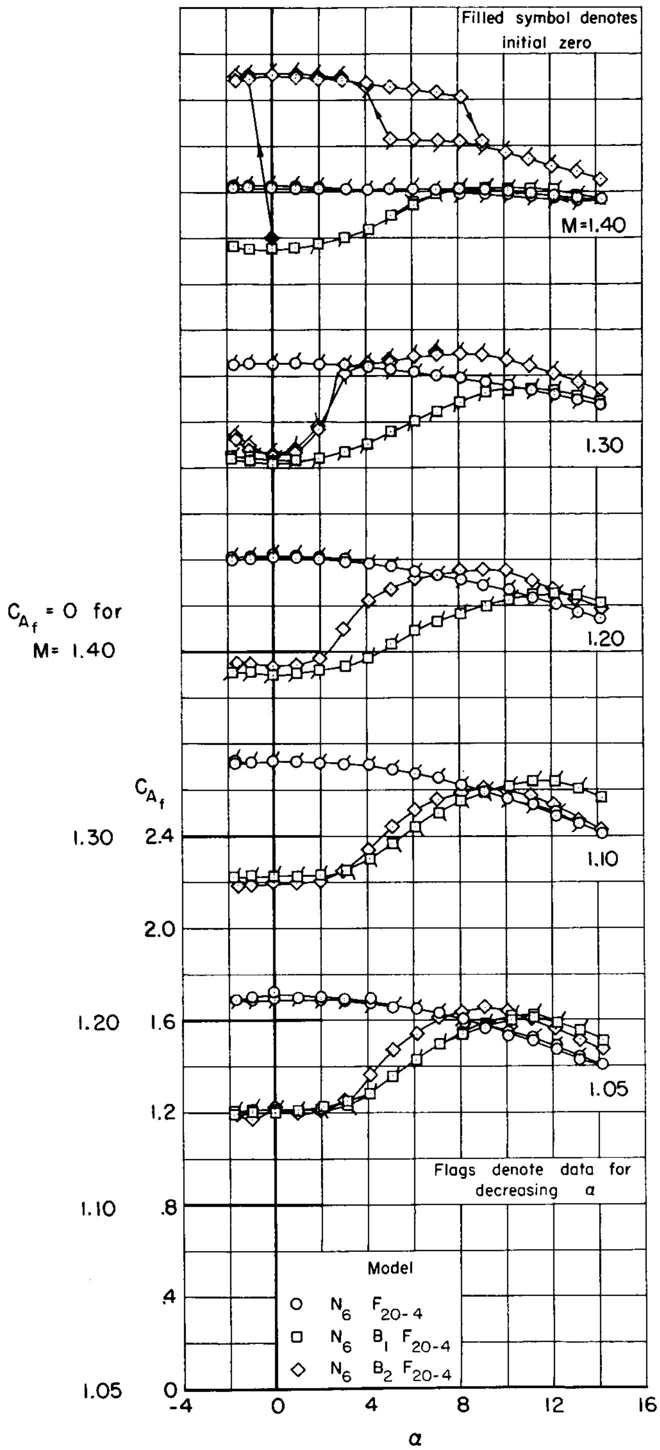


(f) Forebody axial-force coefficient; M = 1.05 to 1.40.

Figure 5.- Continued.

A
3
3
0

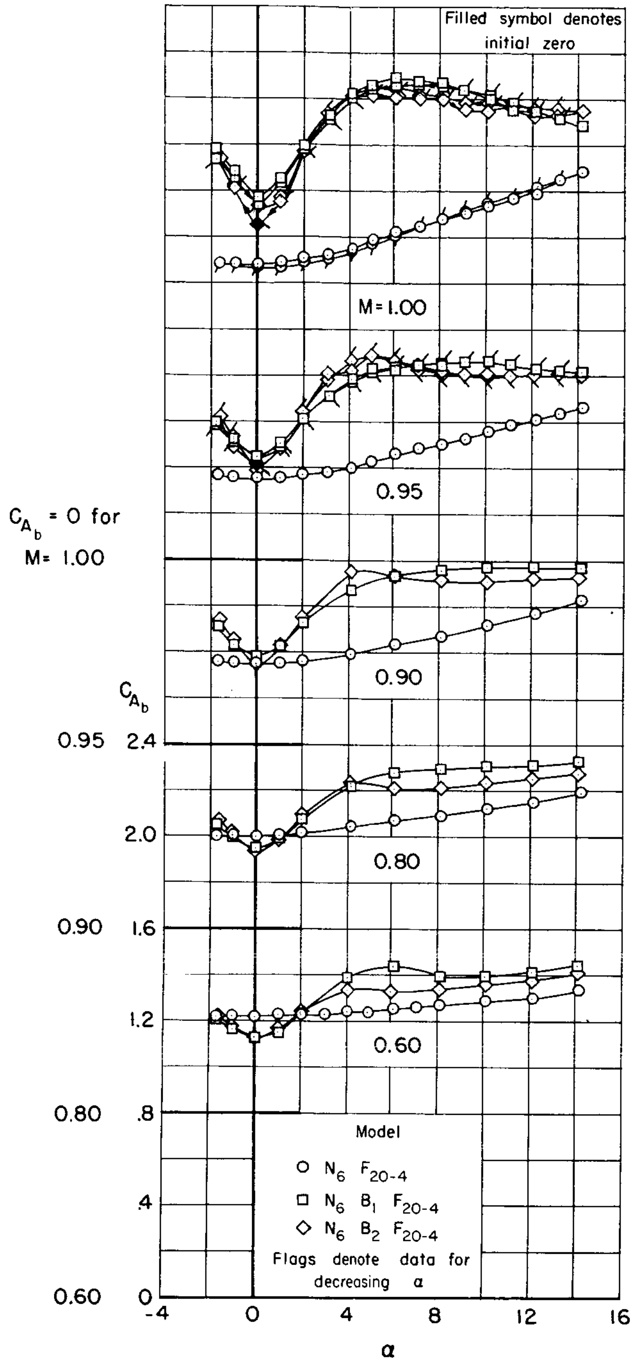


(g) Base axial-force coefficient; M = 0.60 to 1.00.

Figure 5.- Continued.

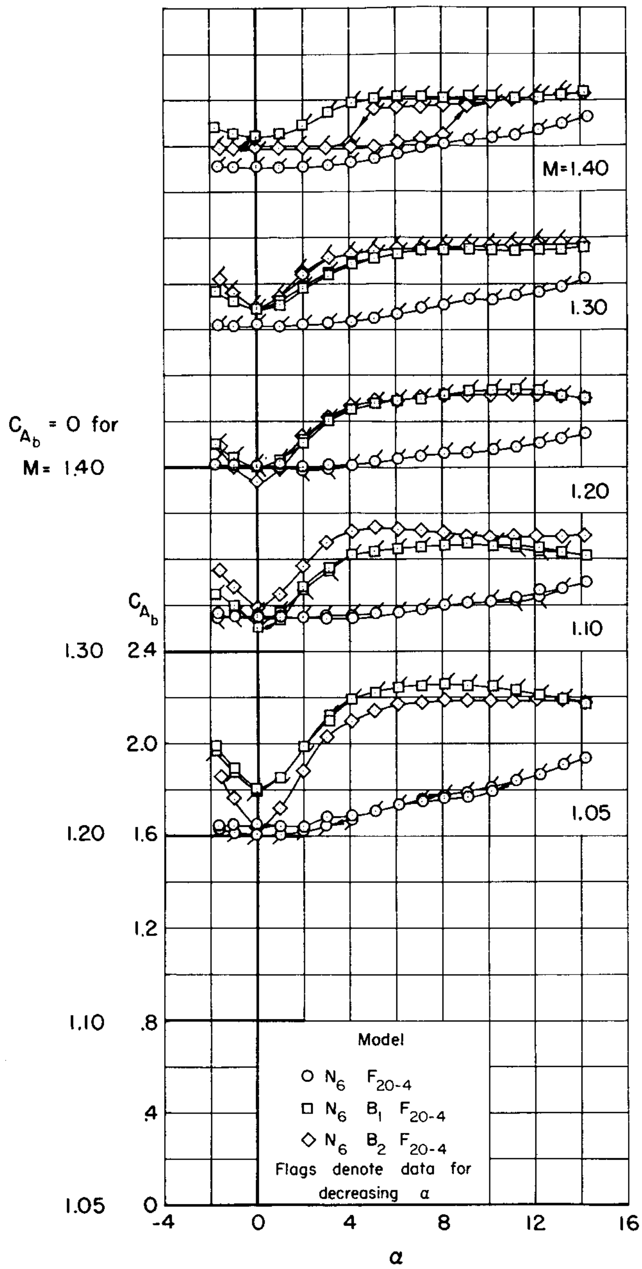


(h) Base axial-force coefficient, M = 1.05 to 1.40.

Figure 5.- Concluded.

A330

[redacted]

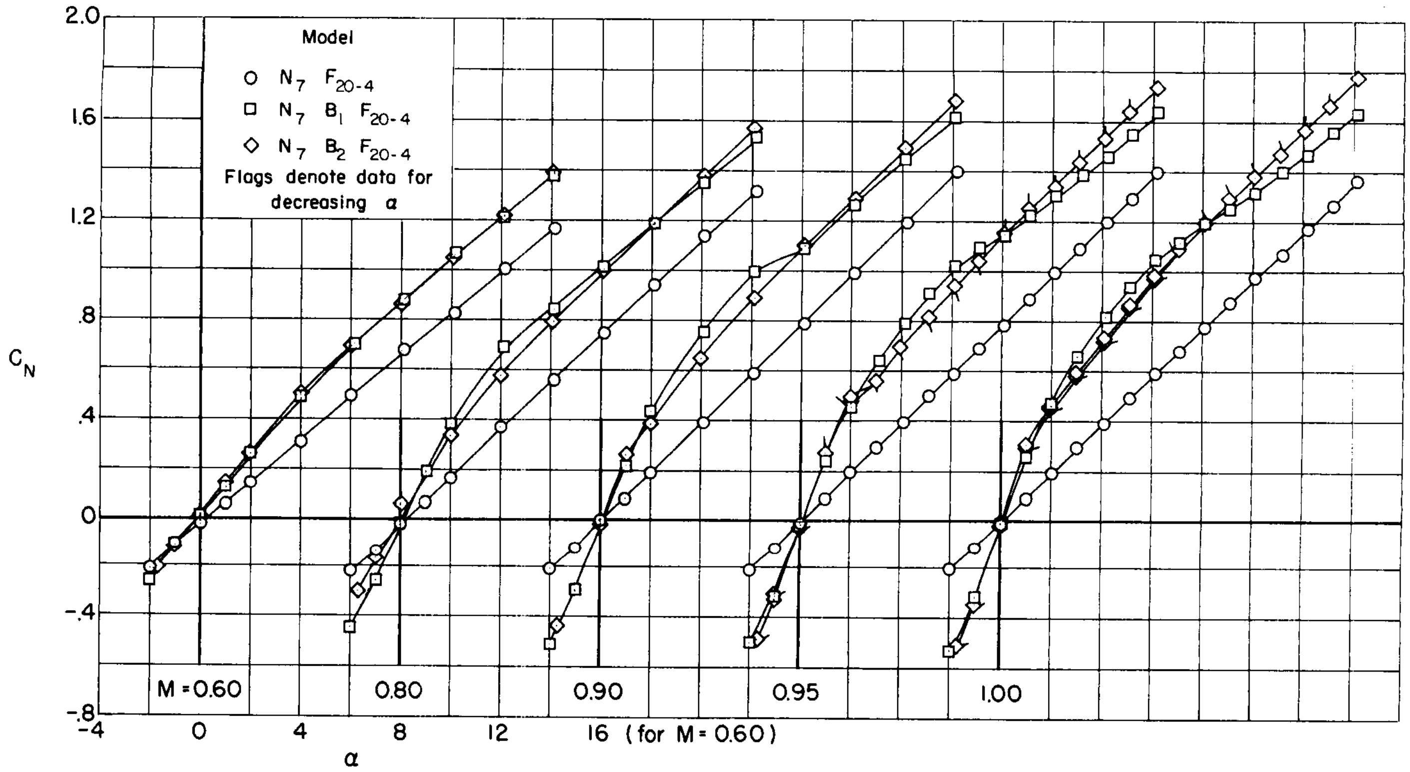


(a) Normal-force coefficient; M = 0.60 to 1.00.

Figure 6.- Static longitudinal aerodynamic coefficient for models with the $N_7$ nose.

[redacted]

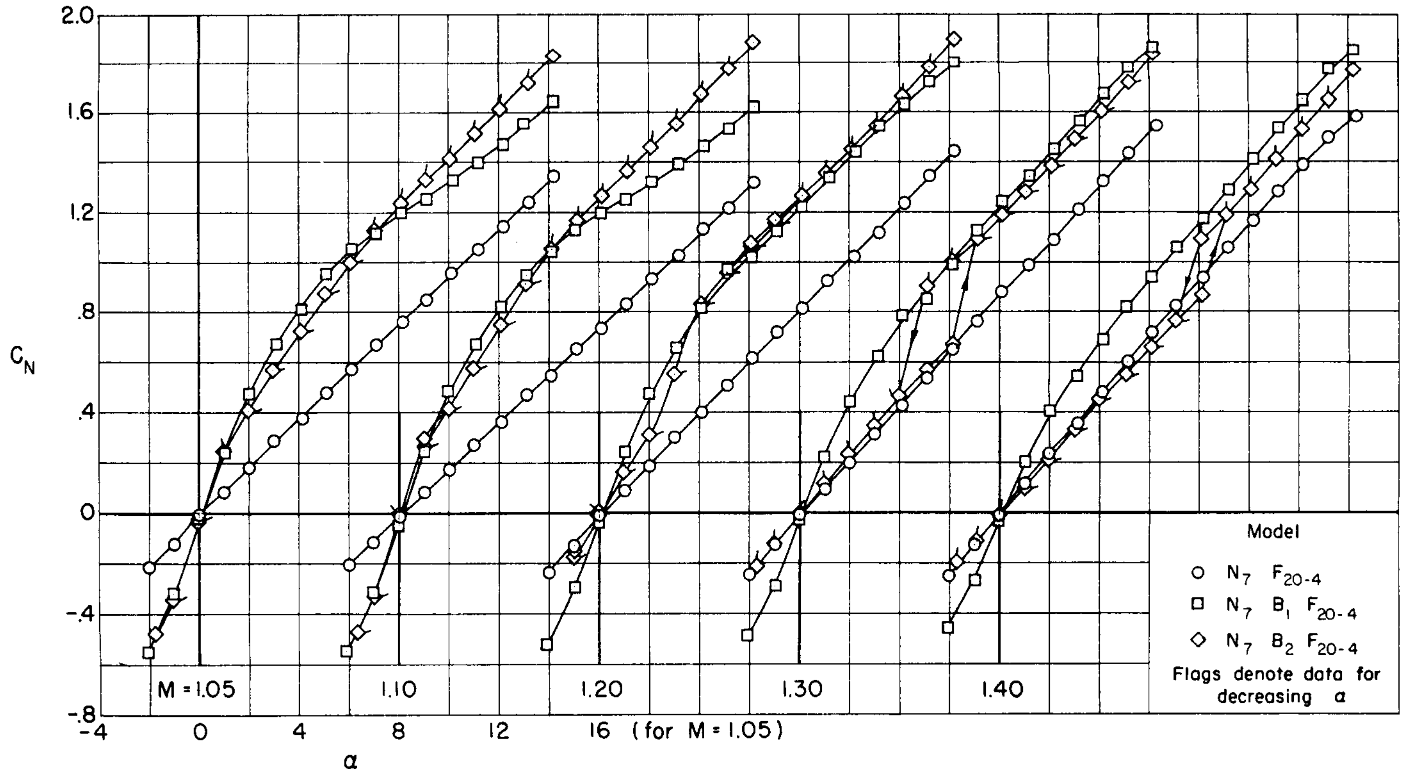


(b) Normal-force coefficient; M = 1.05 to 1.40.

Figure 6.- Continued.

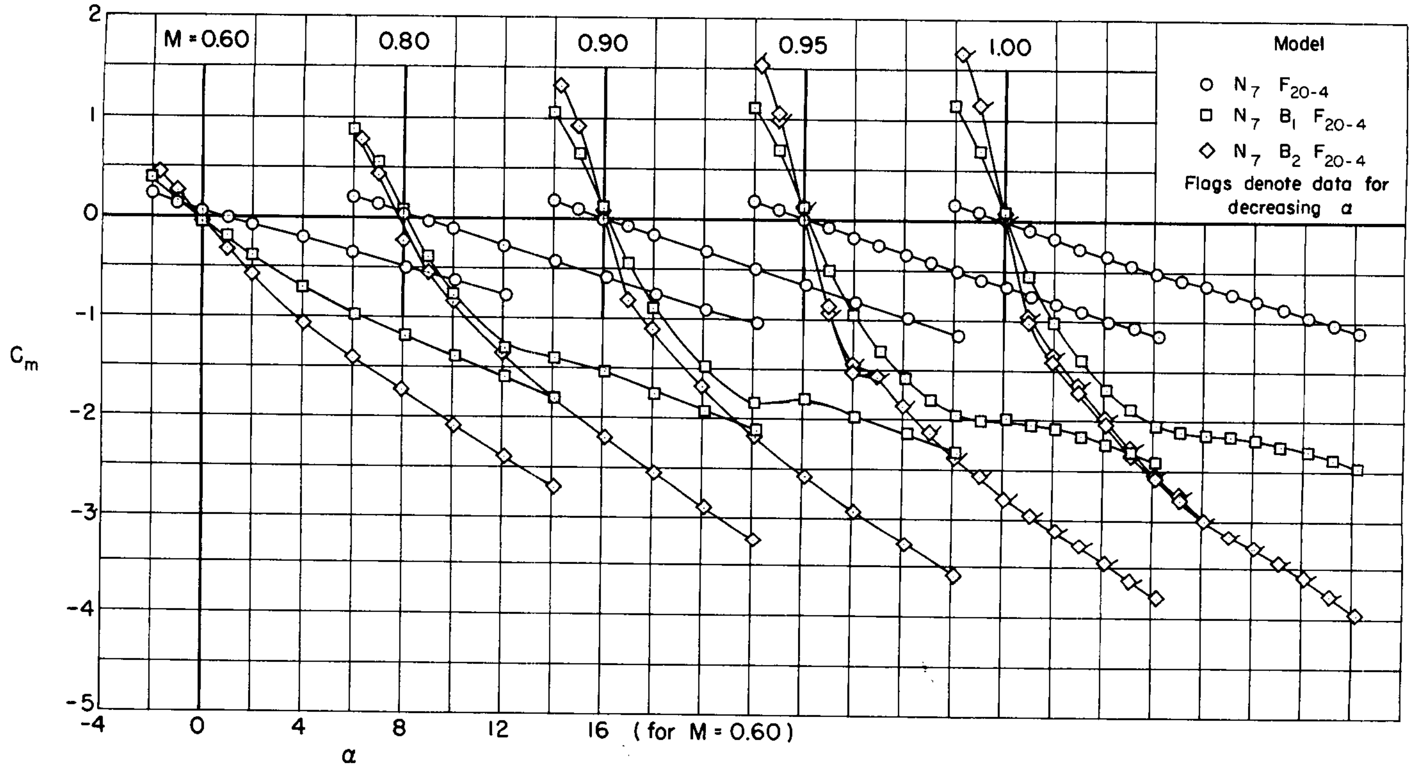


(c) Pitching-moment coefficient; M = 0.60 to 1.00.

Figure 6.- Continued.

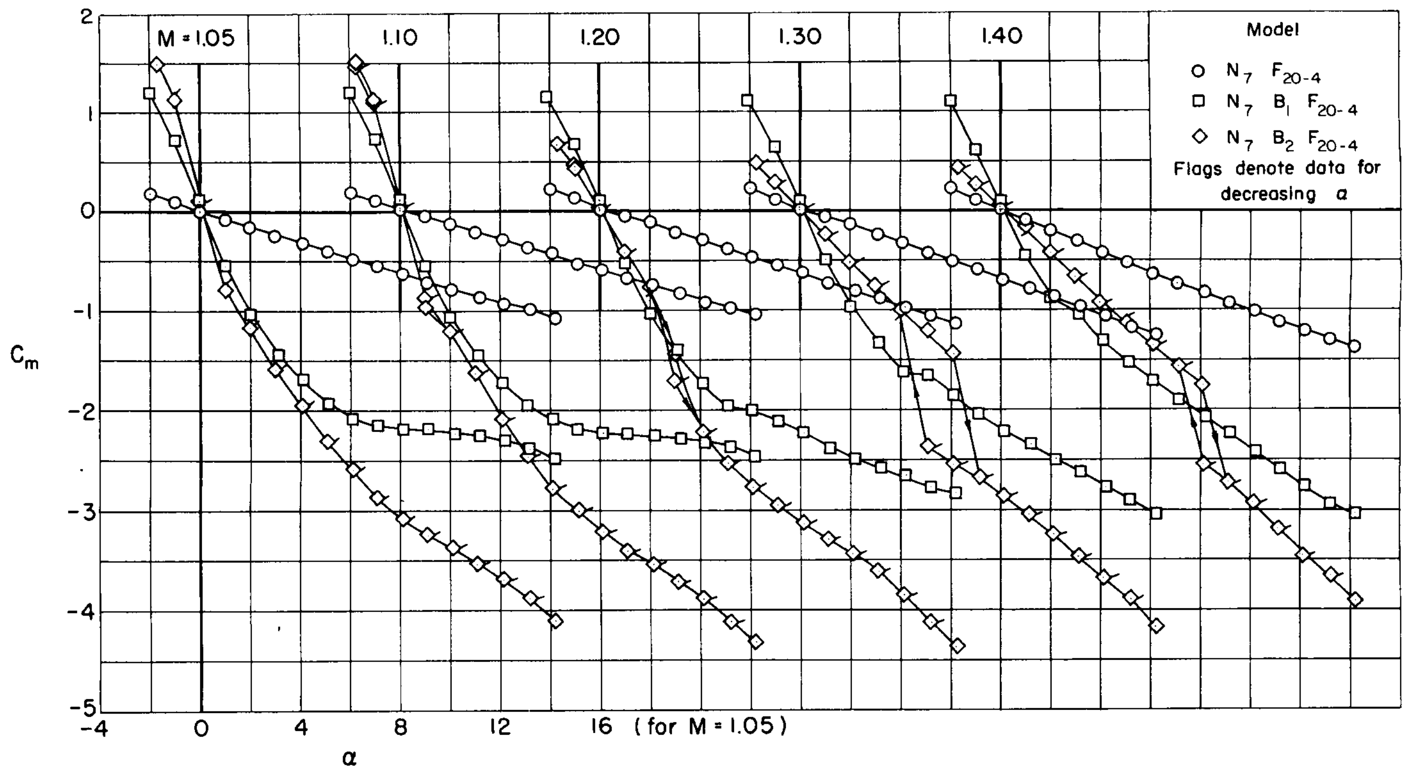


(d) Pitching-moment coefficient; M = 1.05 to 1.40.

Figure 6.- Continued.

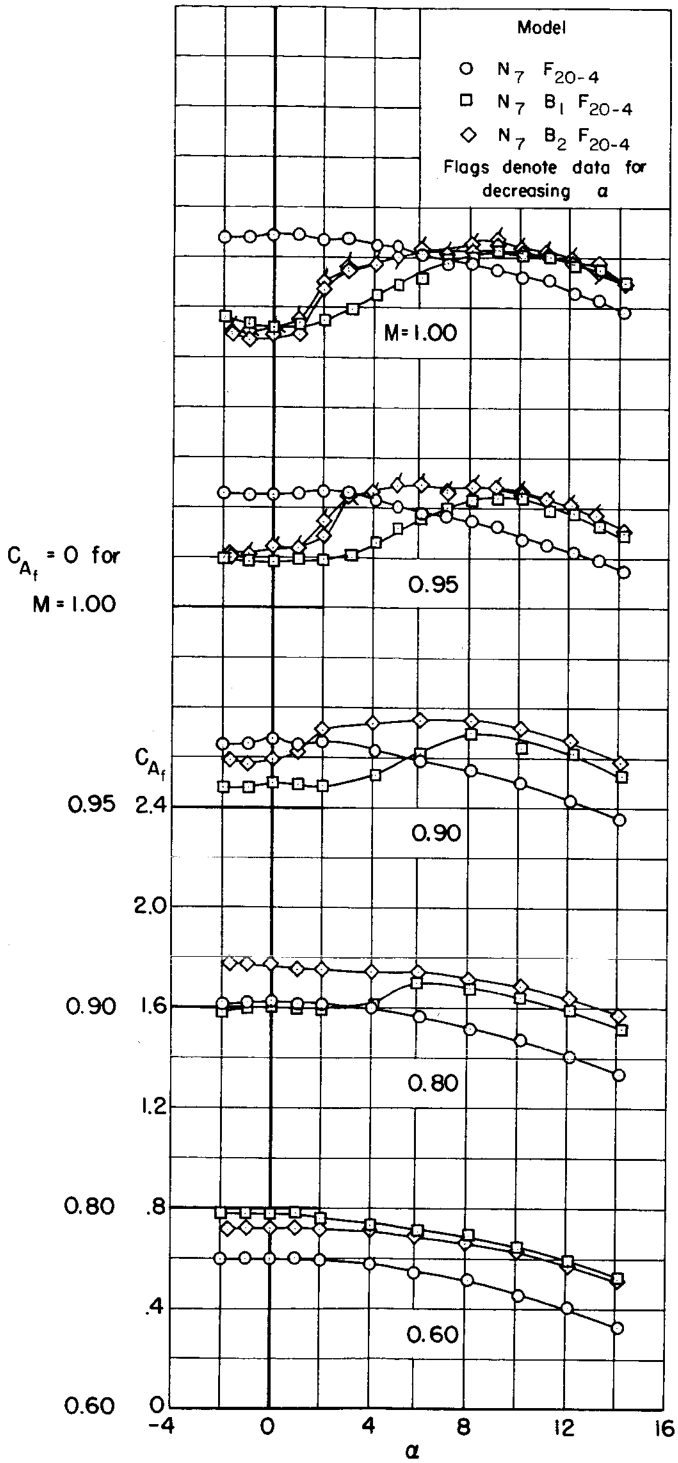


(e) Forebody axial-force coefficient; M = 0.60 to 1.00.

Figure 6.- Continued.

[redacted]

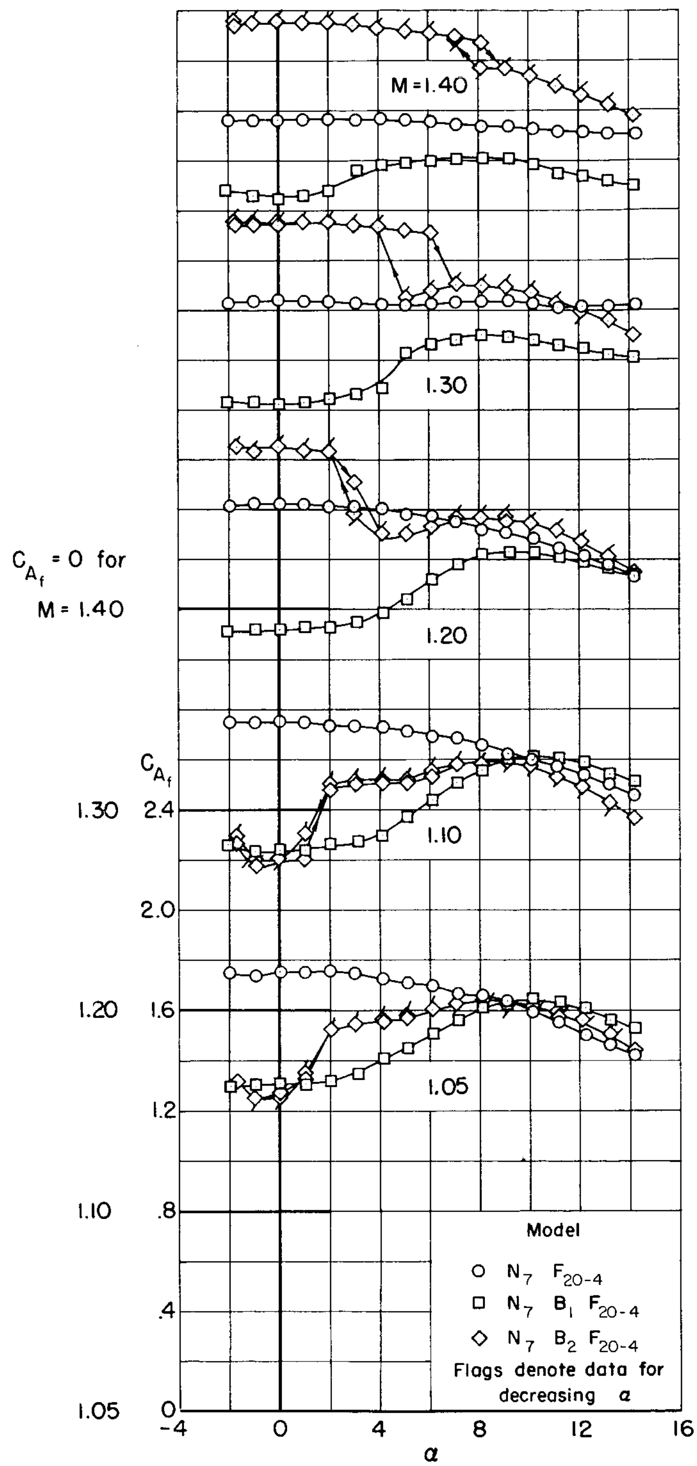


(f) Forebody axial-force coefficient; M = 1.05 to 1.40.

Figure 6.- Continued.

[redacted]

A
3
3
0

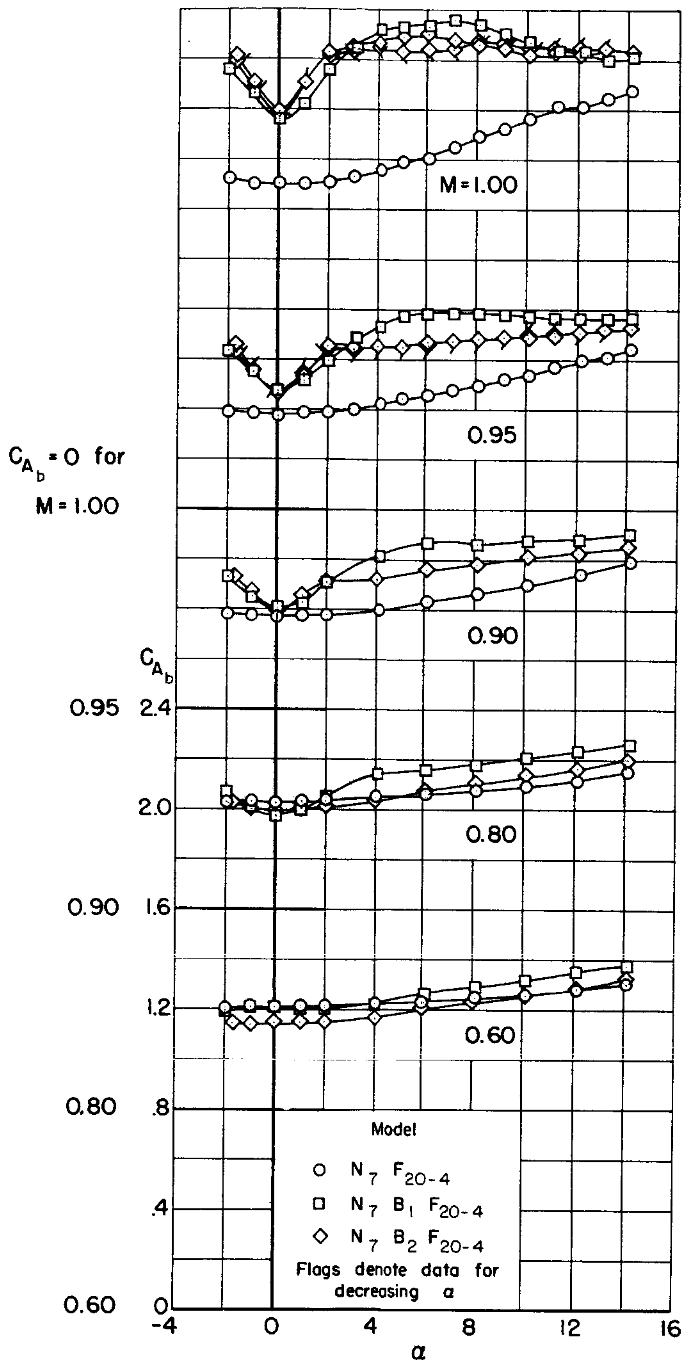


(g) Base axial-force coefficient; M = 0.60 to 1.00.

Figure 6.- Continued.

[redacted]

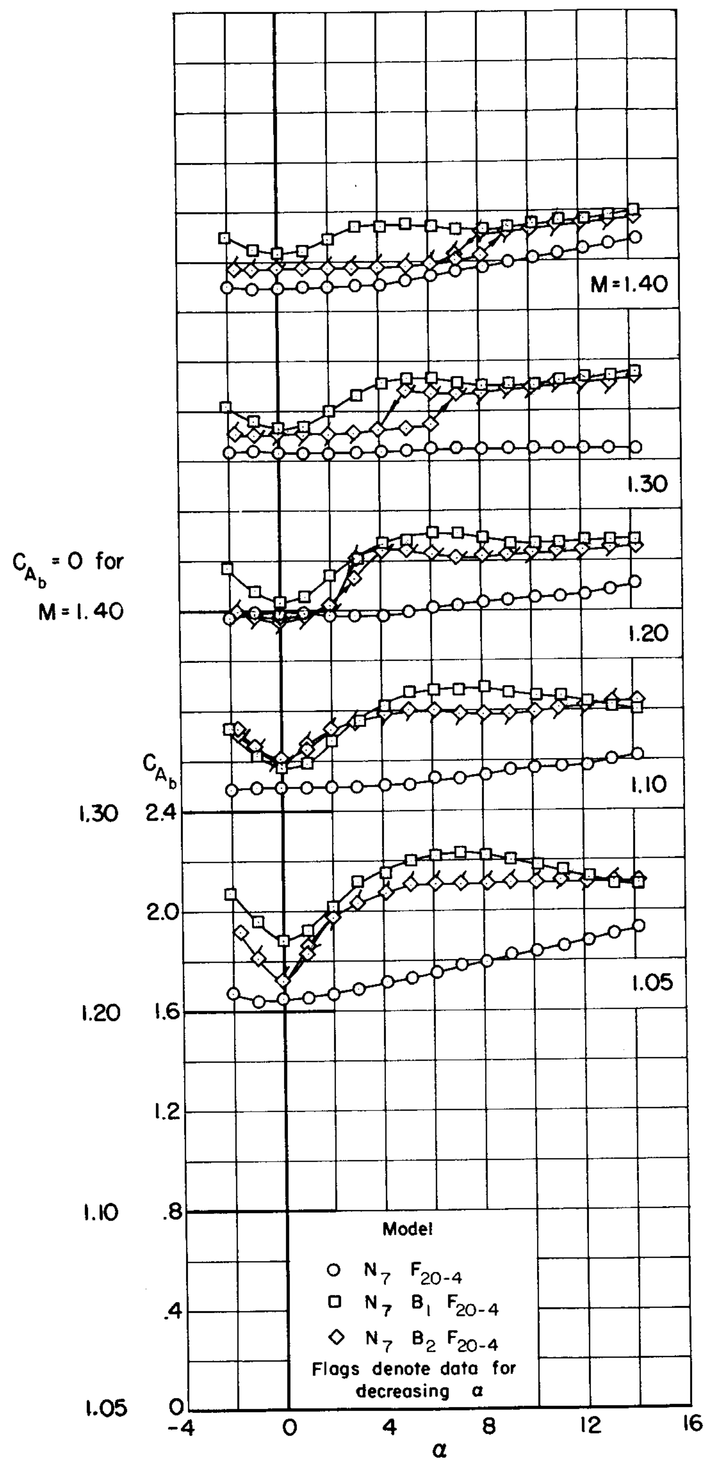


(h) Base axial-force coefficient; M = 1.05 to 1.40.

Figure 6.- Concluded.

[redacted]

A
3
3
0

[redacted]

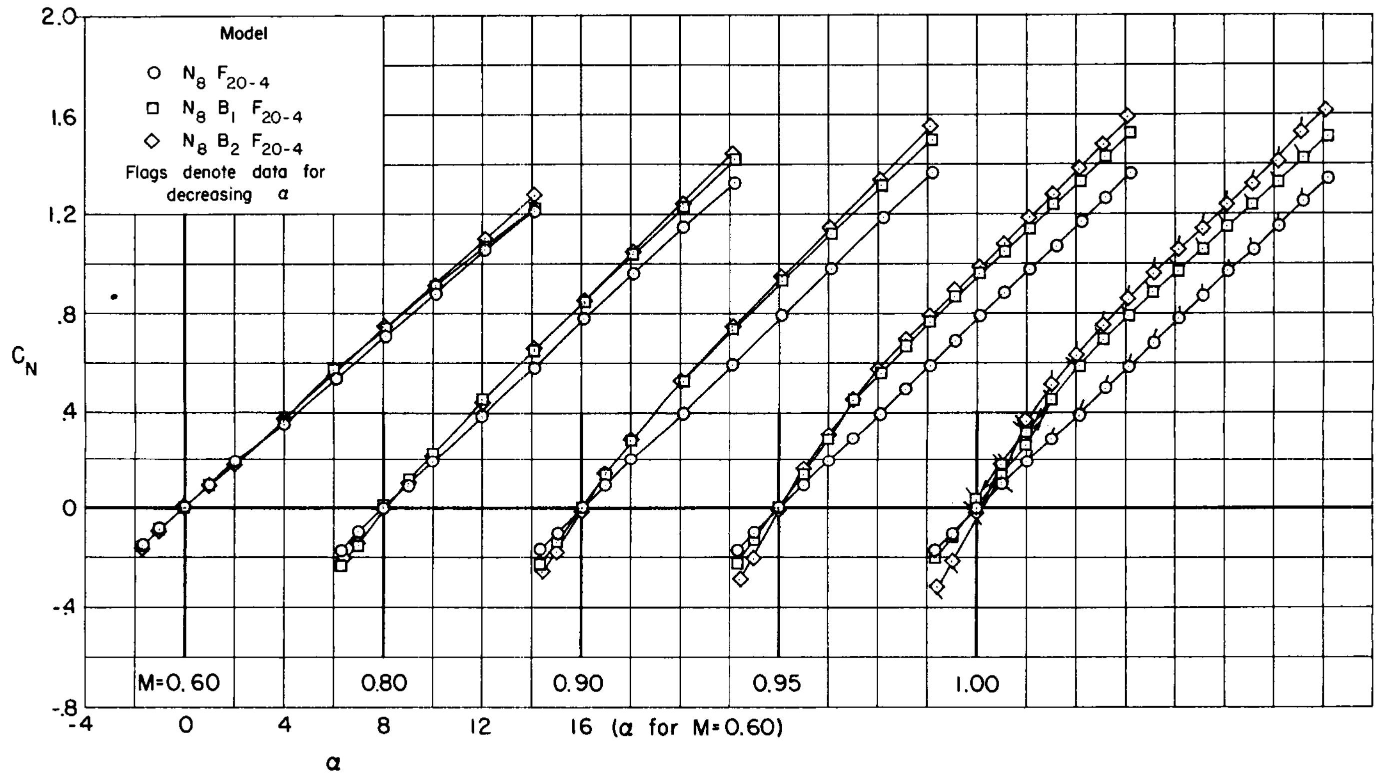


(a) Normal-force coefficient; M = 0.60 to 1.00.

Figure 7.- Static longitudinal aerodynamic coefficient for models with the $N_8$ nose.

[redacted]

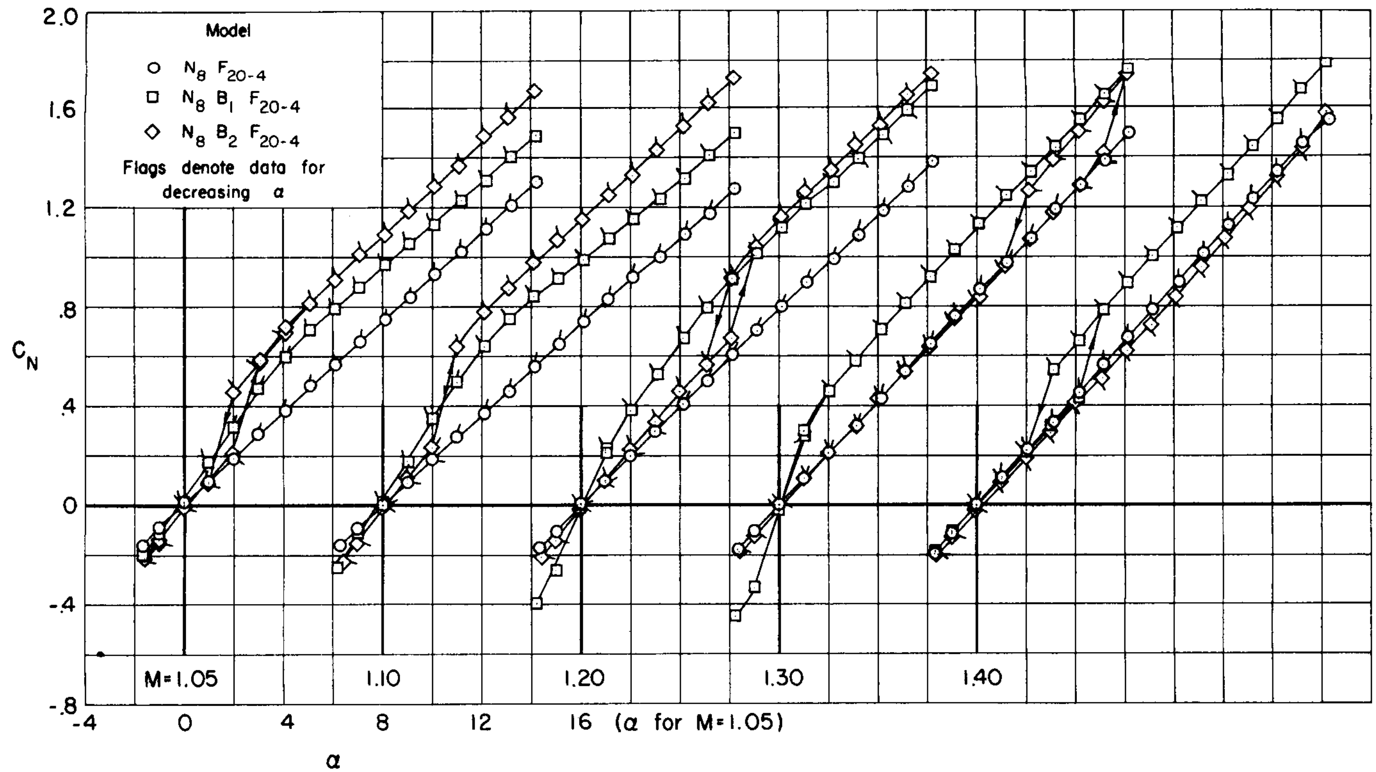


(b) Normal-force coefficient; M = 1.05 to 1.40.

Figure 7.- Continued.

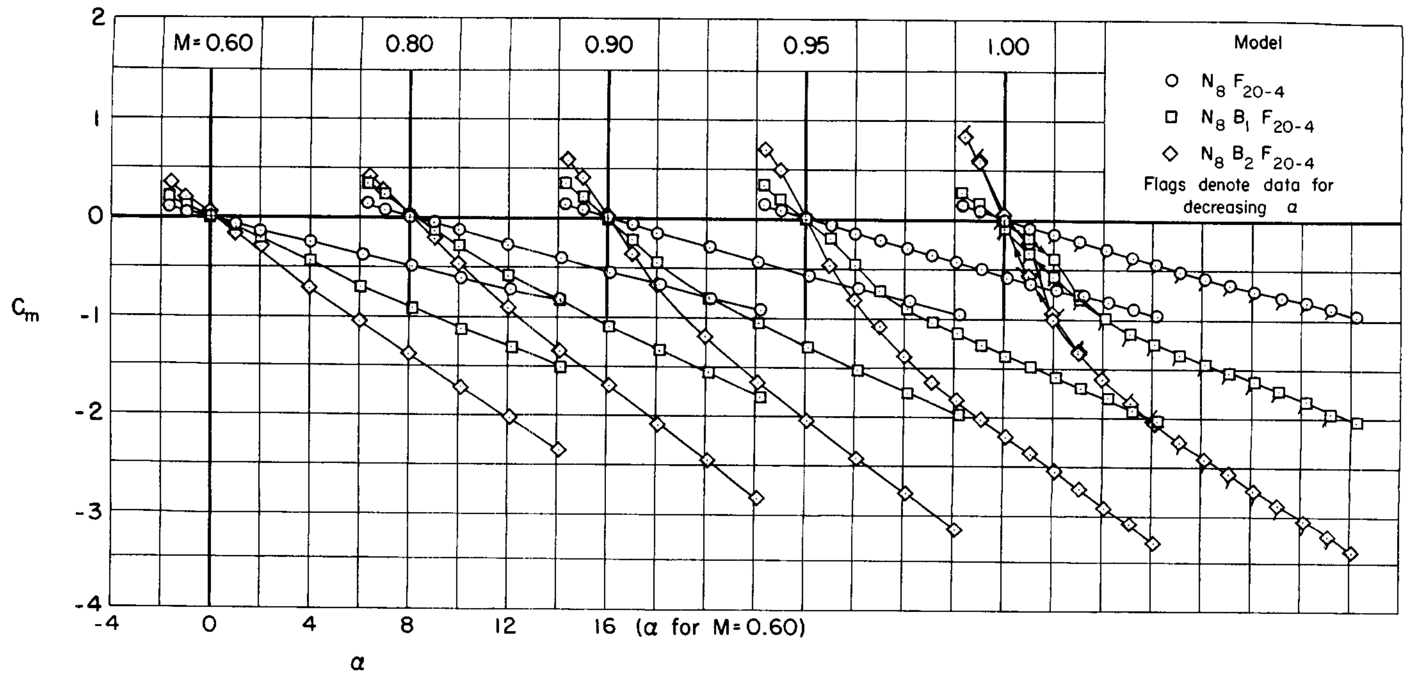


(c) Pitching-moment coefficient; M = 0.60 to 1.00.

Figure 7.- Continued.

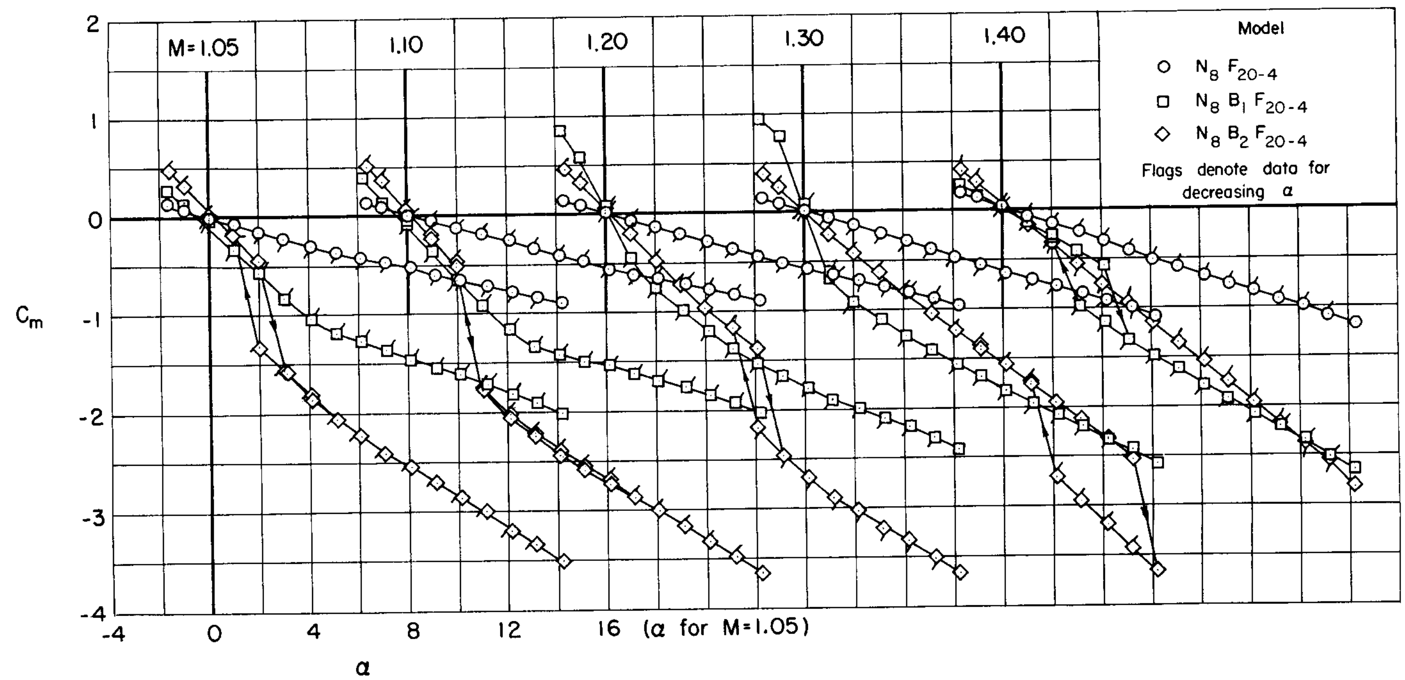


(d) Pitching-moment coefficient; M = 1.05 to 1.40.

Figure 7.- Continued.

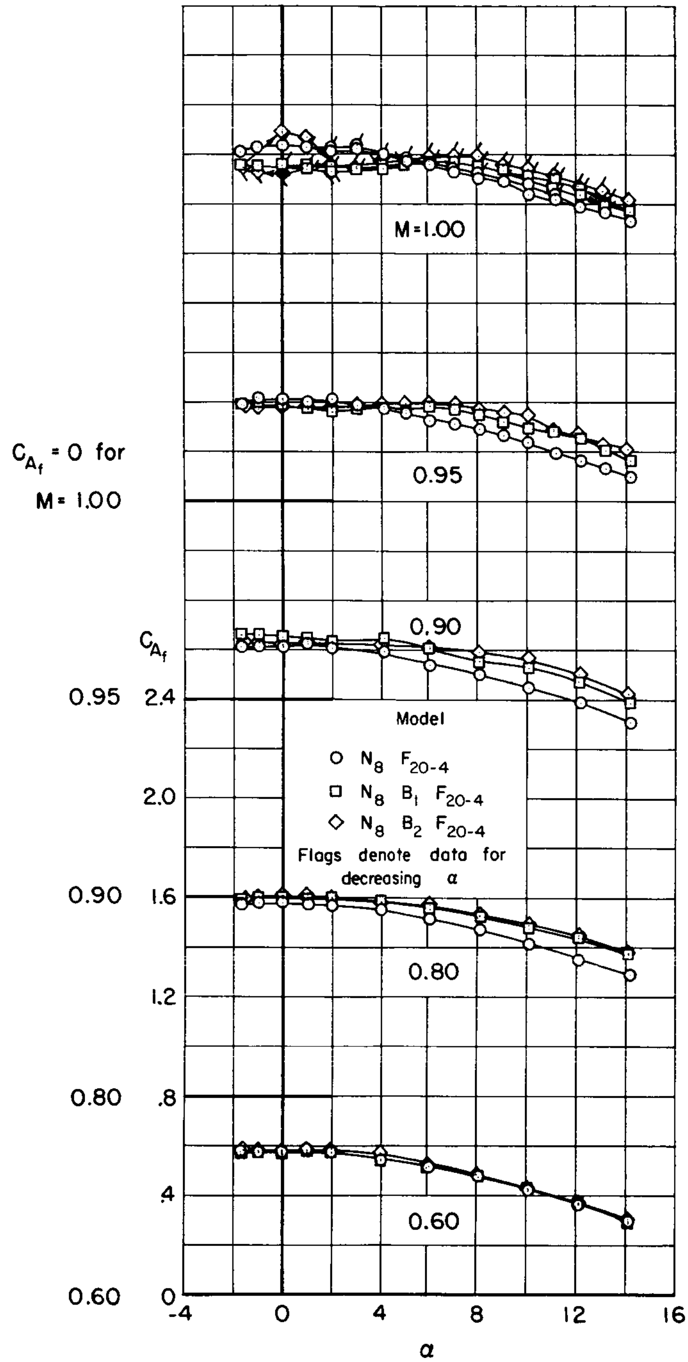


(e) Forebody axial-force coefficient; M = 0.60 to 1.00.

Figure 7.- Continued.

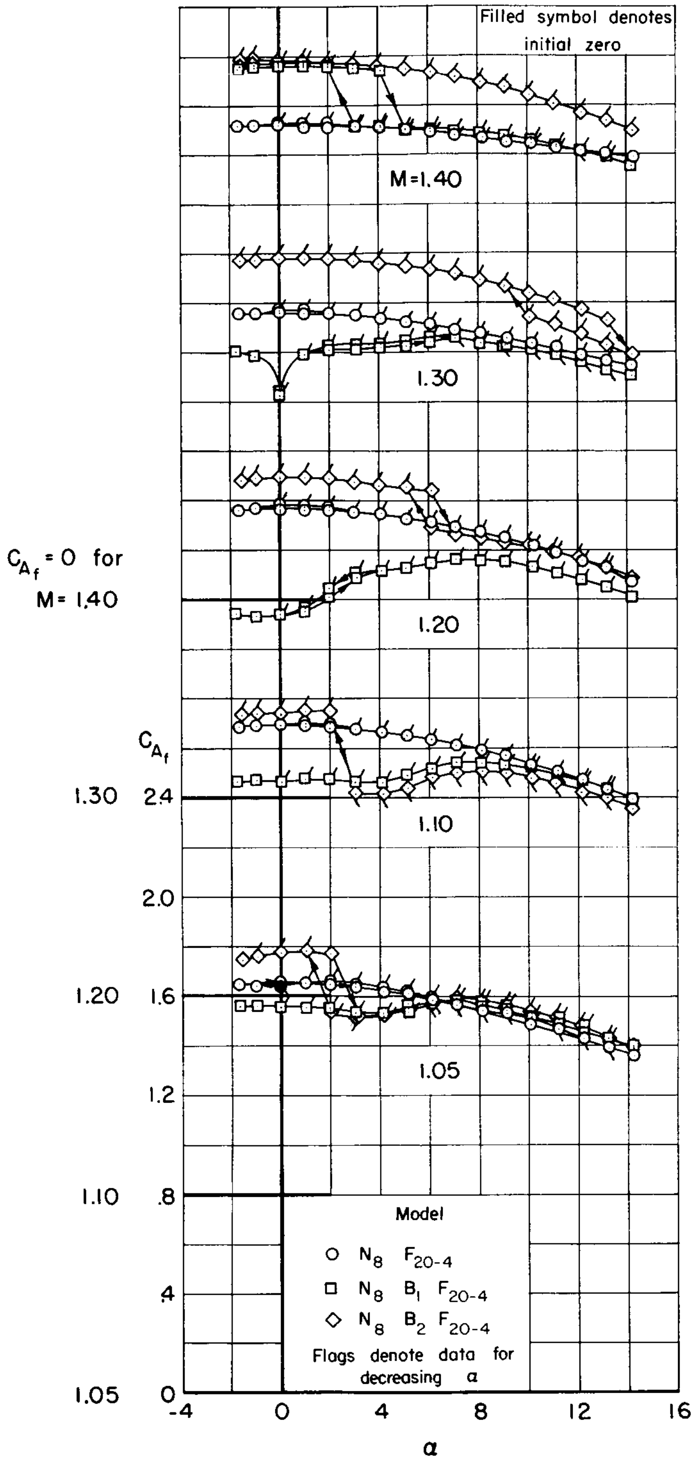


(f) Forebody axial-force coefficient; M = 1.05 to 1.40.

Figure 7.- Continued.

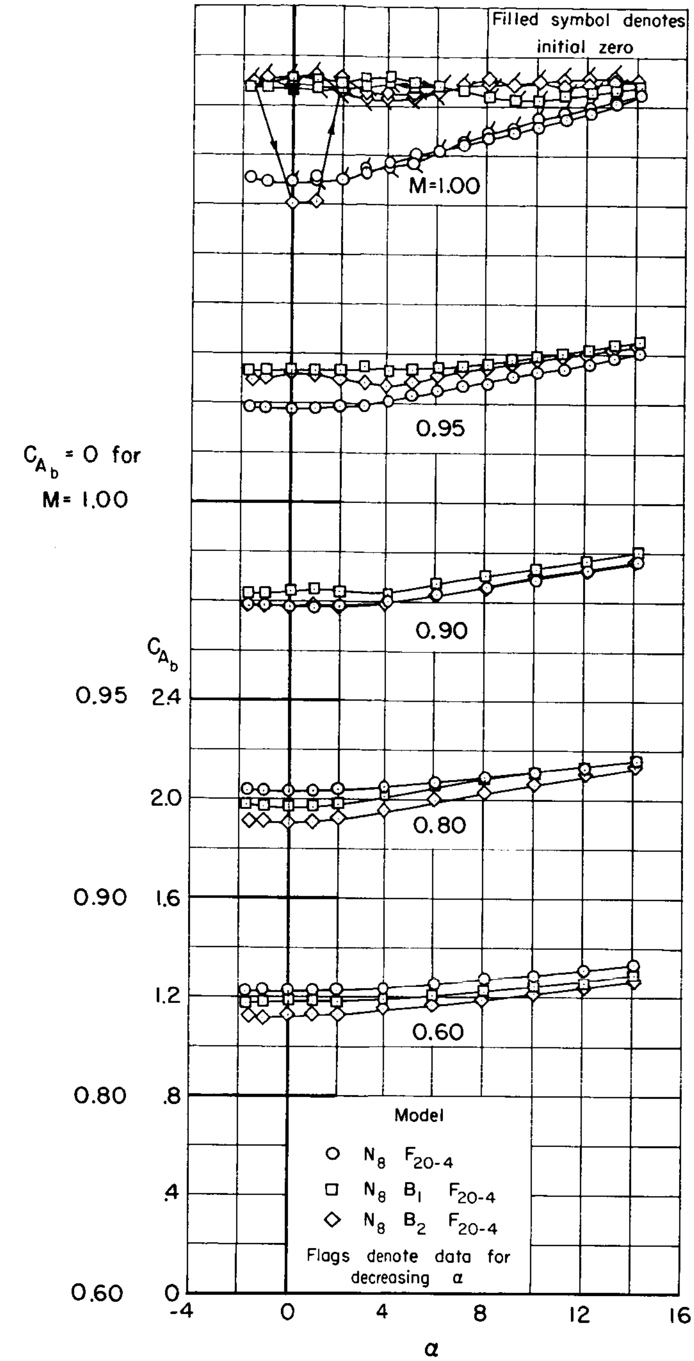


(g) Base axial-force coefficient; M = 0.60 to 1.00.

Figure 7.- Continued.

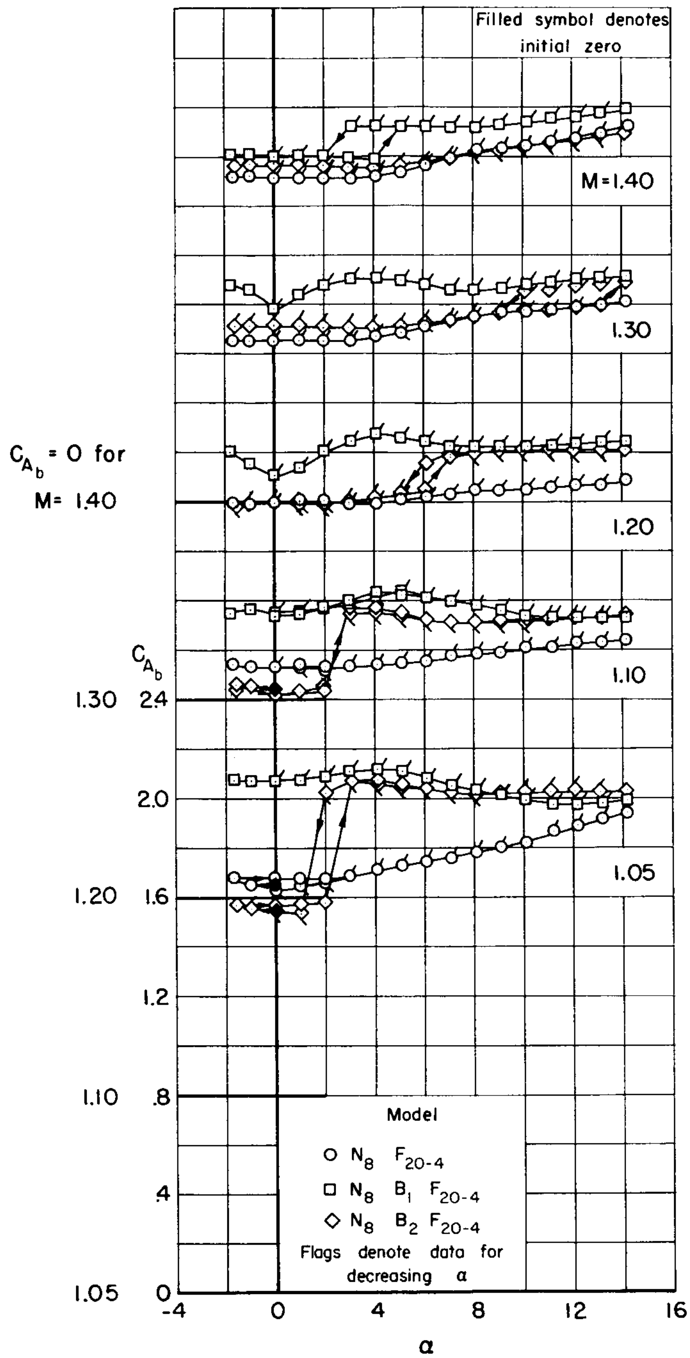


(h) Base axial-force coefficient; M = 1.05 to 1.40.

Figure 7.- Concluded.

A
3
3
0

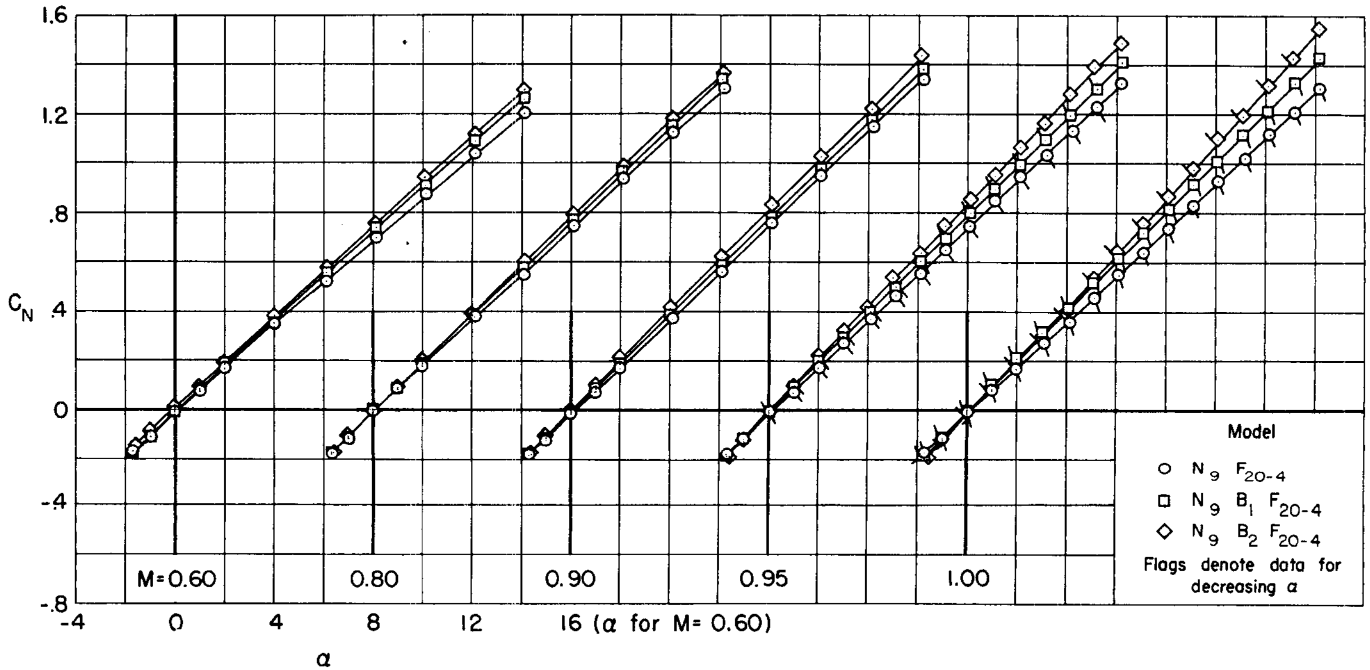


(a) Normal-force coefficient; M = 0.60 to 1.00.

Figure 8.- Static longitudinal aerodynamic coefficient for models with the $N_9$ nose.

A 3 3 0

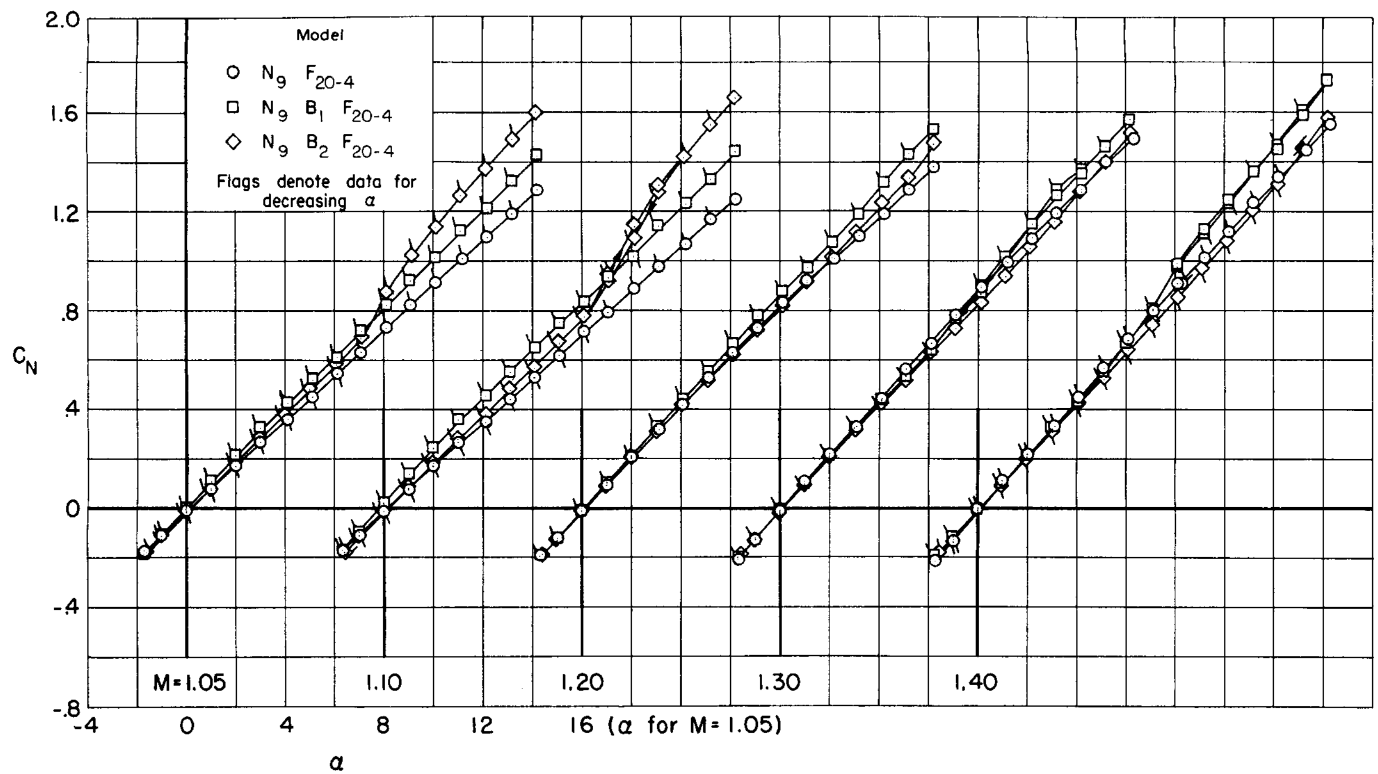


(b) Normal-force coefficient; M = 1.05 to 1.40.

Figure 8.- Continued.

[redacted]



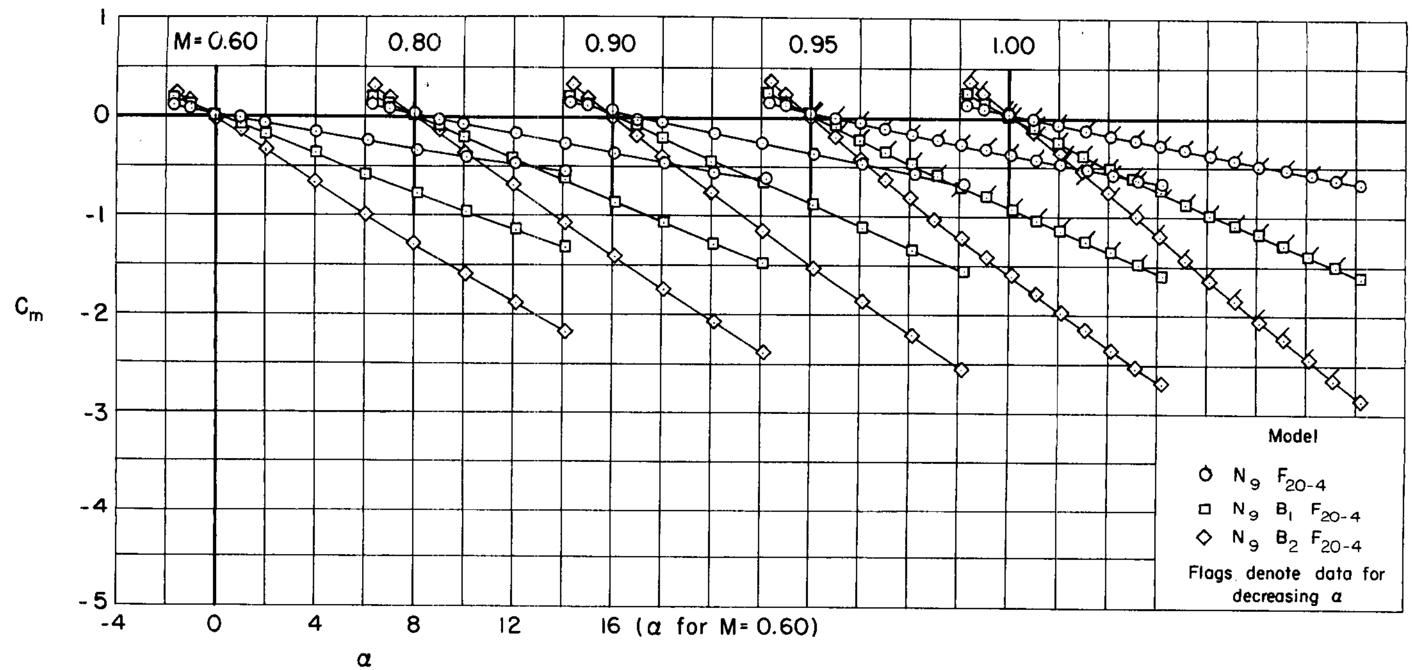


(c) Pitching-moment coefficient; M = 0.60 to 1.00.

Figure 8.- Continued.

[redacted]

[redacted]

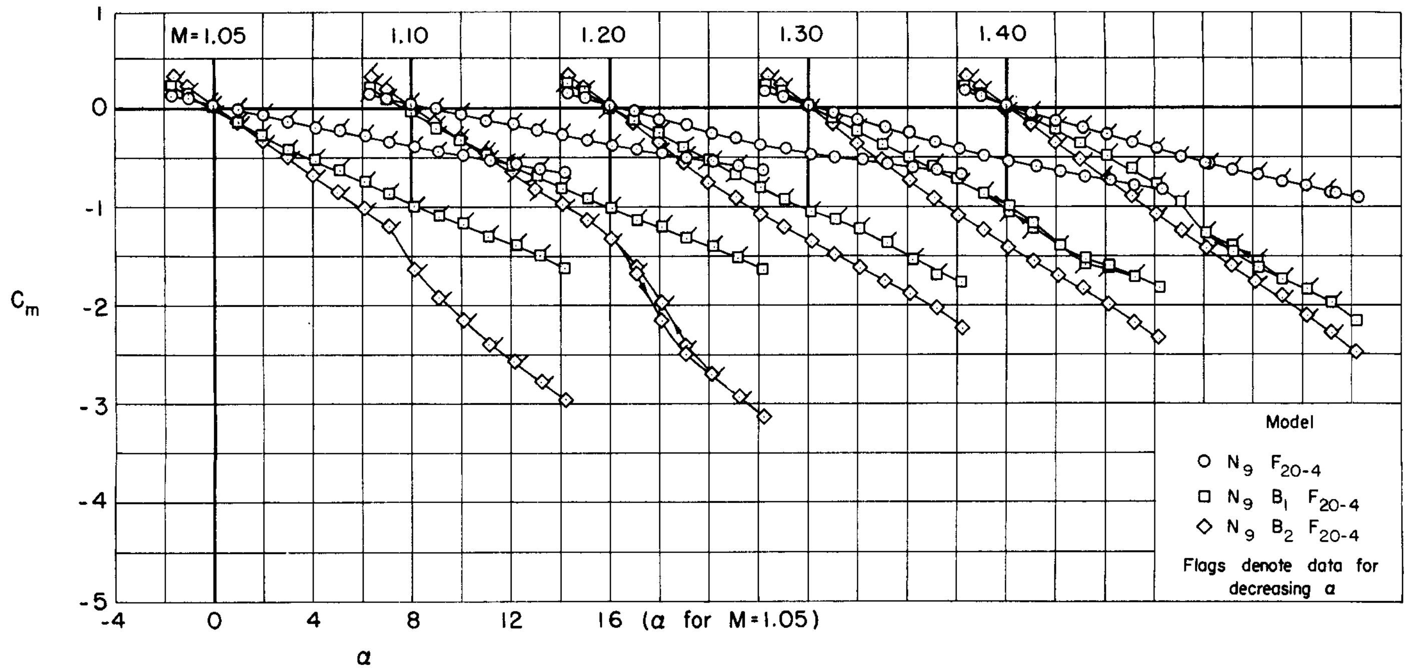


(d) Pitching-moment coefficient; M = 1.05 to 1.40.

Figure 8.- Continued.

[redacted]

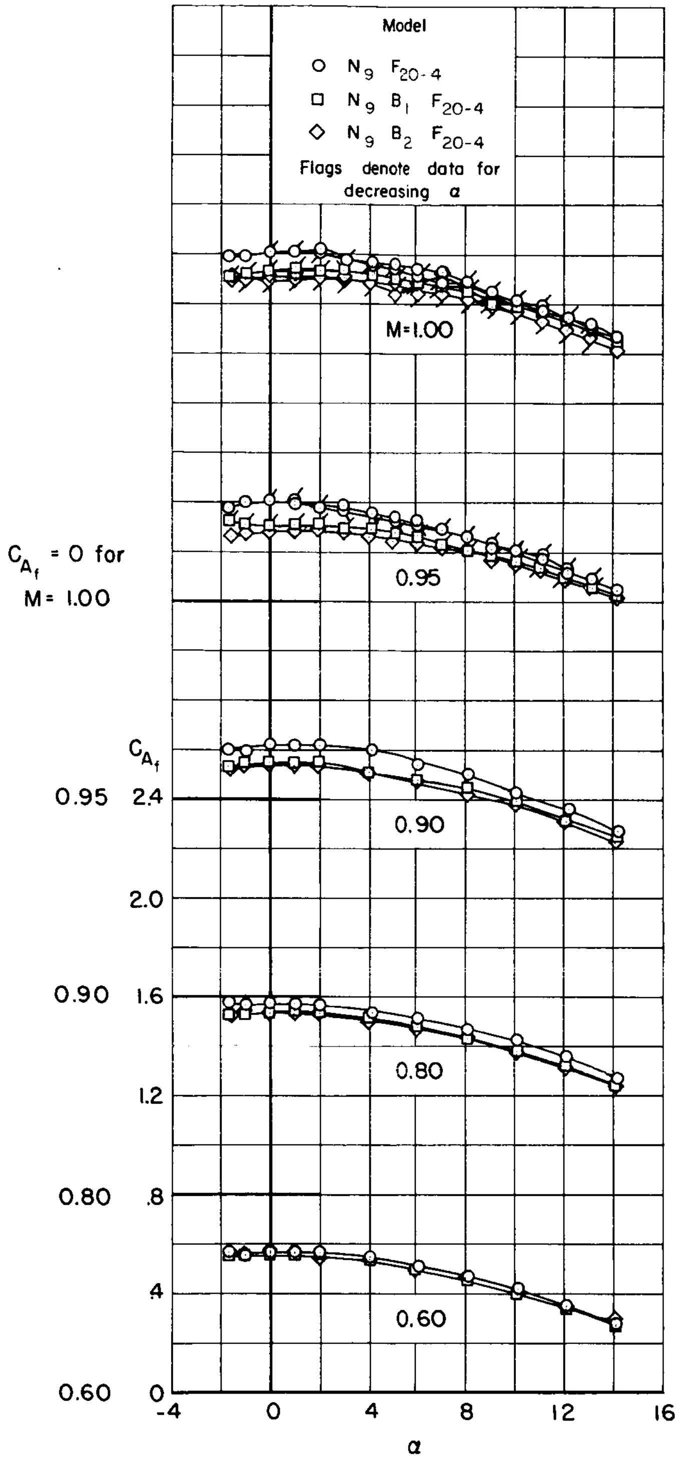


(e) Forebody axial-force coefficient; M = 0.60 to 1.00.

Figure 8.- Continued.

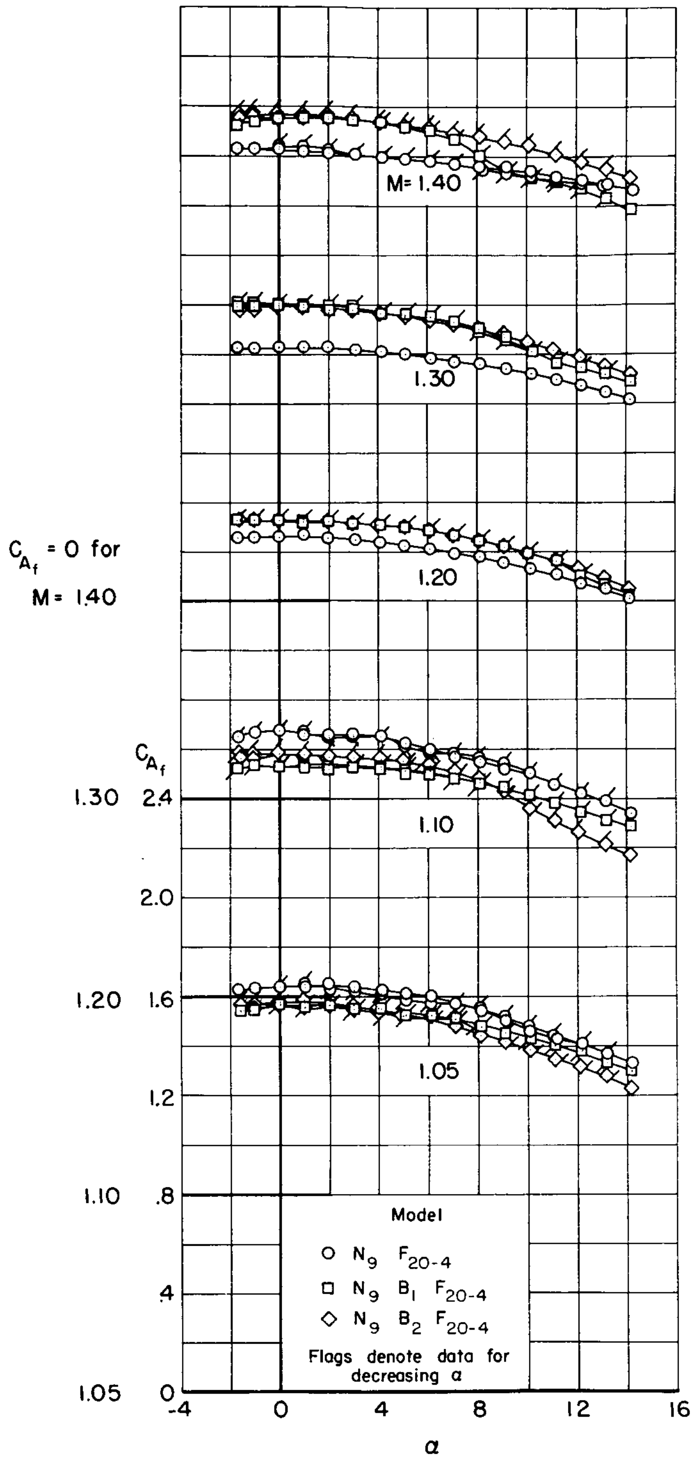


(f) Forebody axial-force coefficient; M = 1.05 to 1.40.

Figure 8.- Continued.

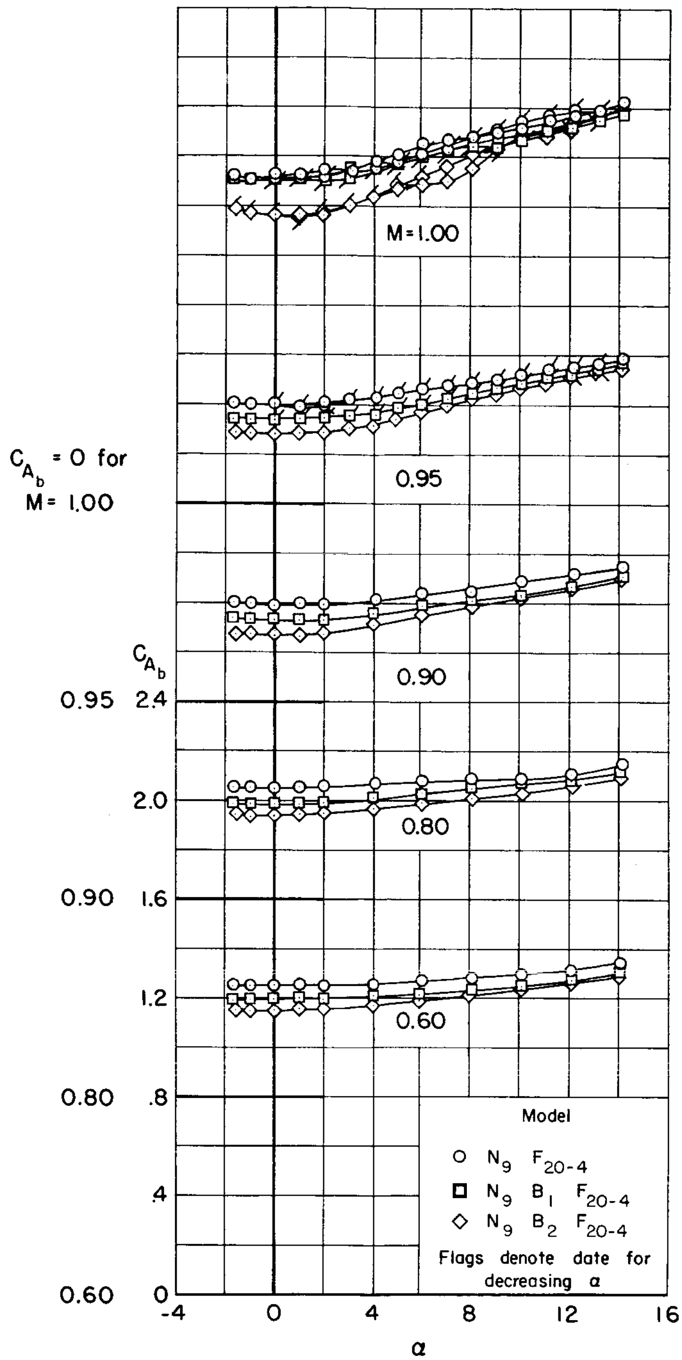


(g) Base axial-force coefficient; M = 0.60 to 1.00.

Figure 8.- Continued.

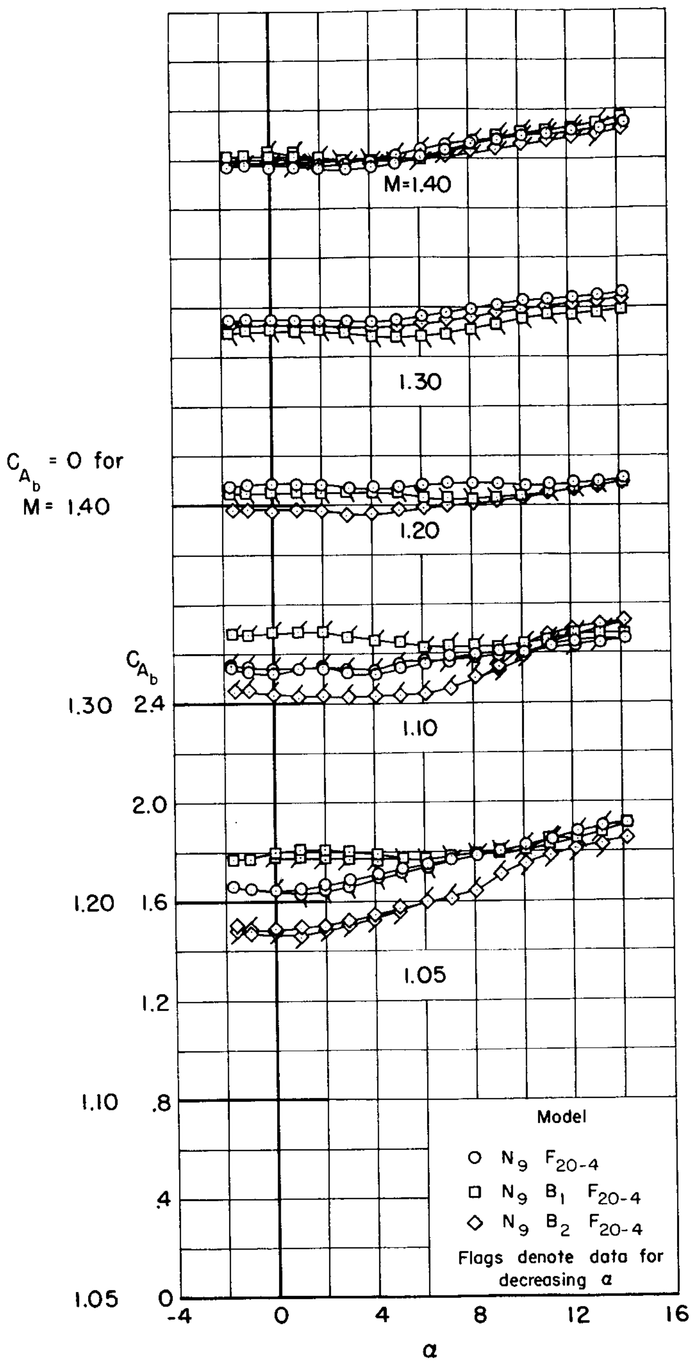


(h) Base axial-force coefficient; M = 1.05 to 1.40.

Figure 8.- Concluded.

[redacted]

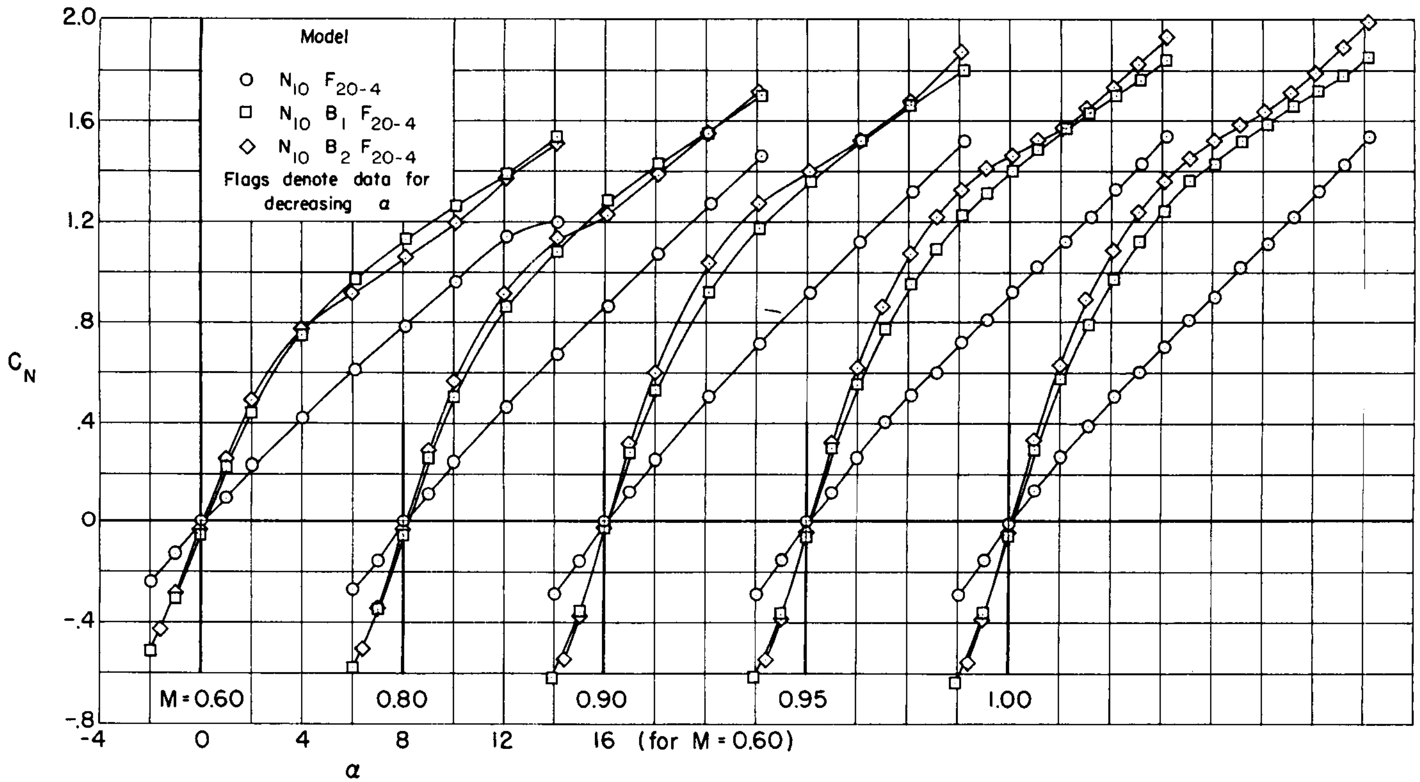


(a) Normal-force coefficient; M = 0.60 to 1.00.

Figure 9.- Static longitudinal aerodynamic coefficient for models with the $N_{10}$ nose.

[redacted]

A330

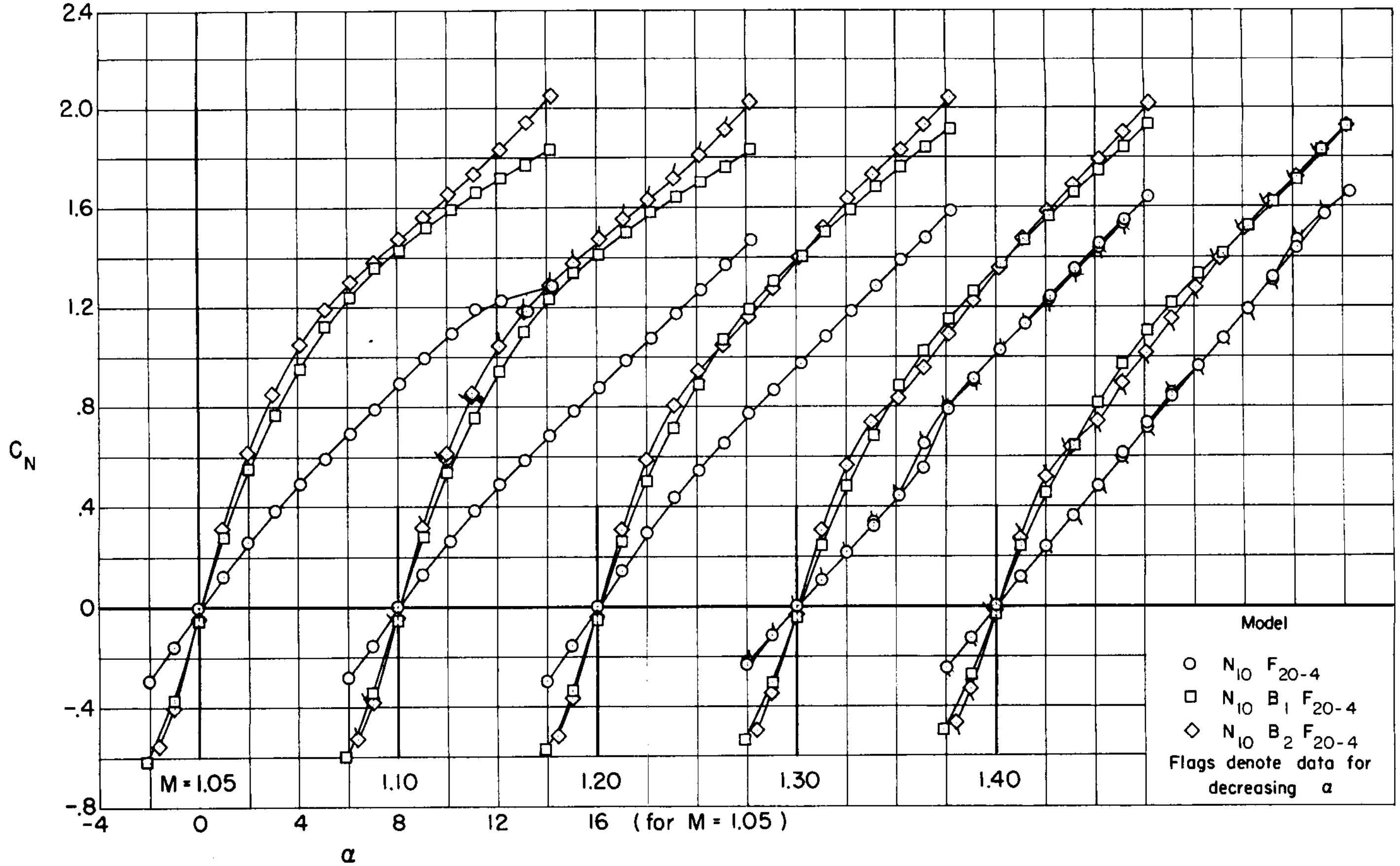


(b) Normal-force coefficient; M = 1.05 to 1.40.

Figure 9.- Continued.

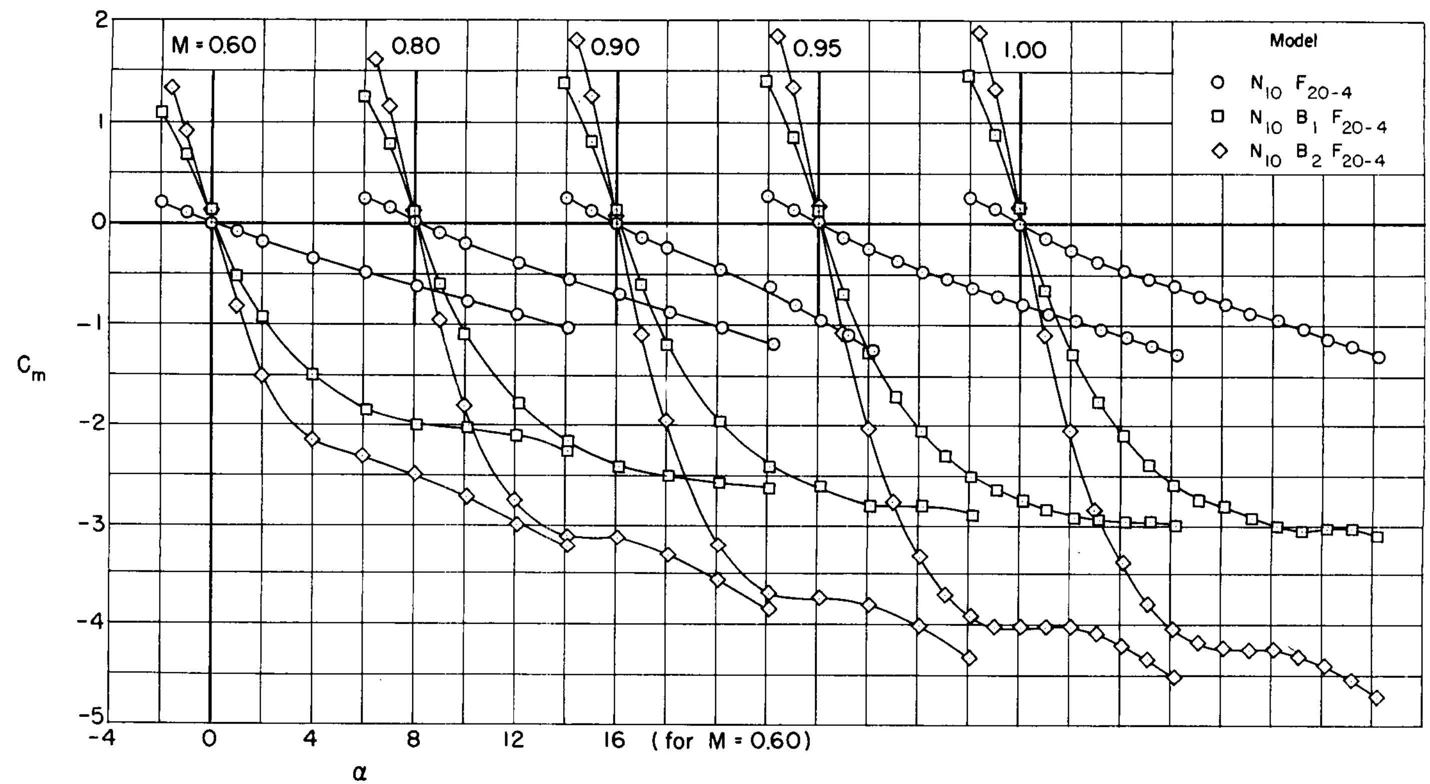


(c) Pitching-moment coefficient; M = 0.60 to 1.00.

Figure 9.- Continued.

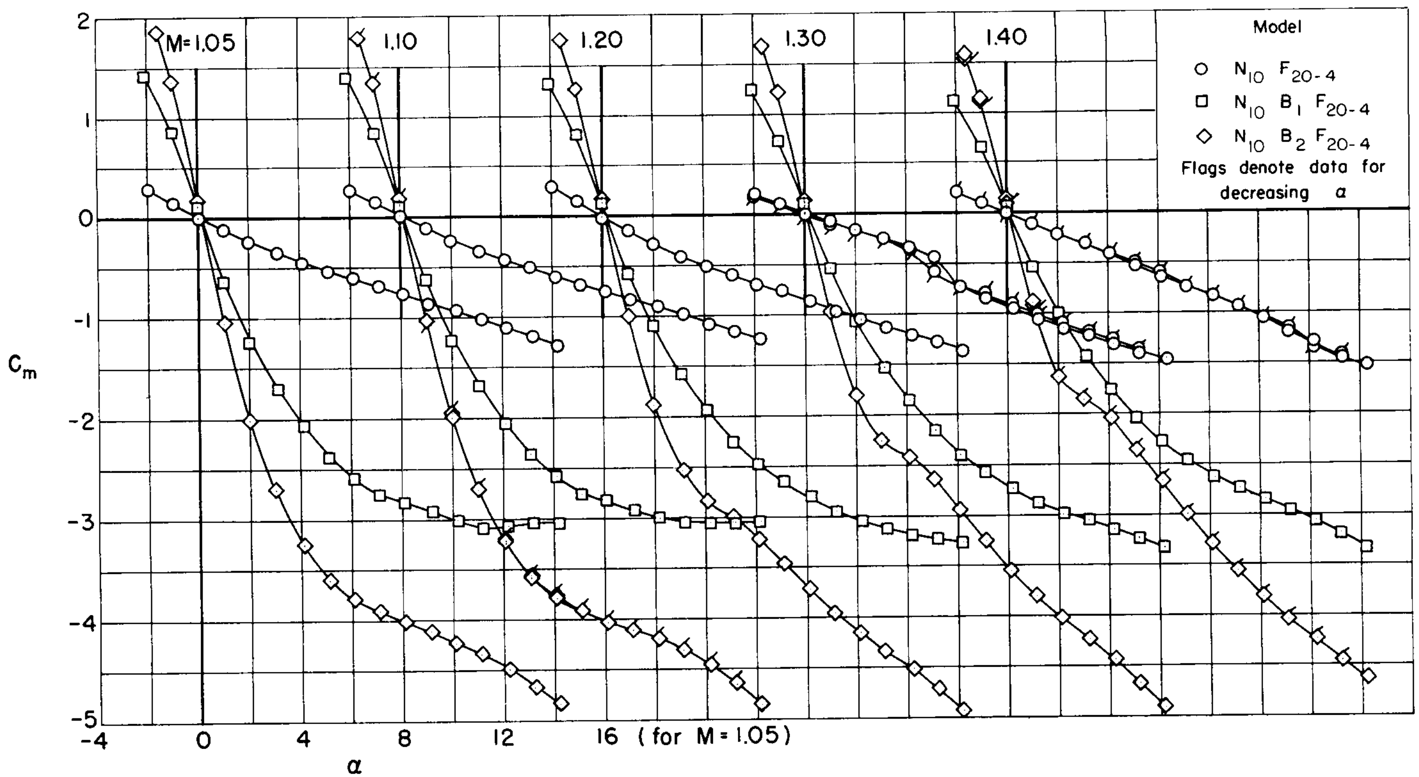


(d) Pitching-moment coefficient; M = 1.05 to 1.40.

Figure 9.- Continued.

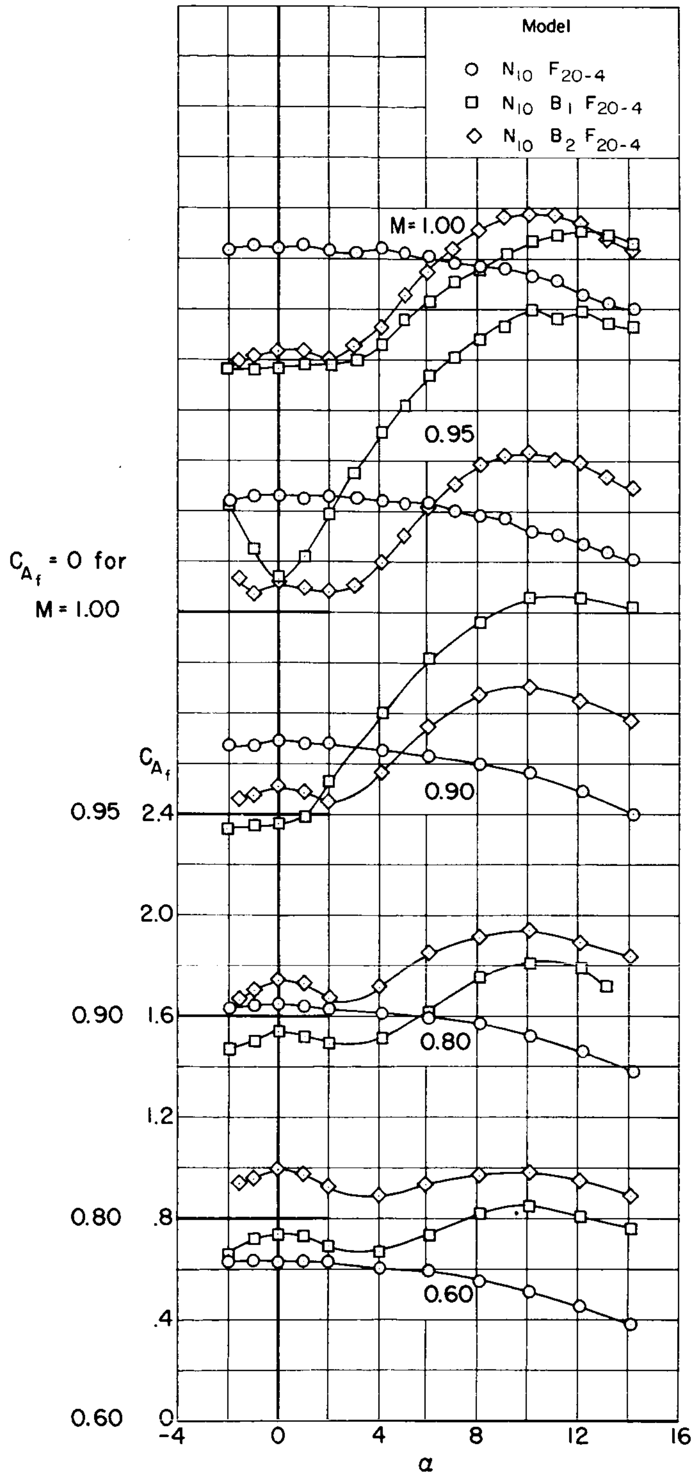


(e) Forebody axial-force coefficient; M = 0.60 to 1.00.

Figure 9.- Continued.

[redacted]

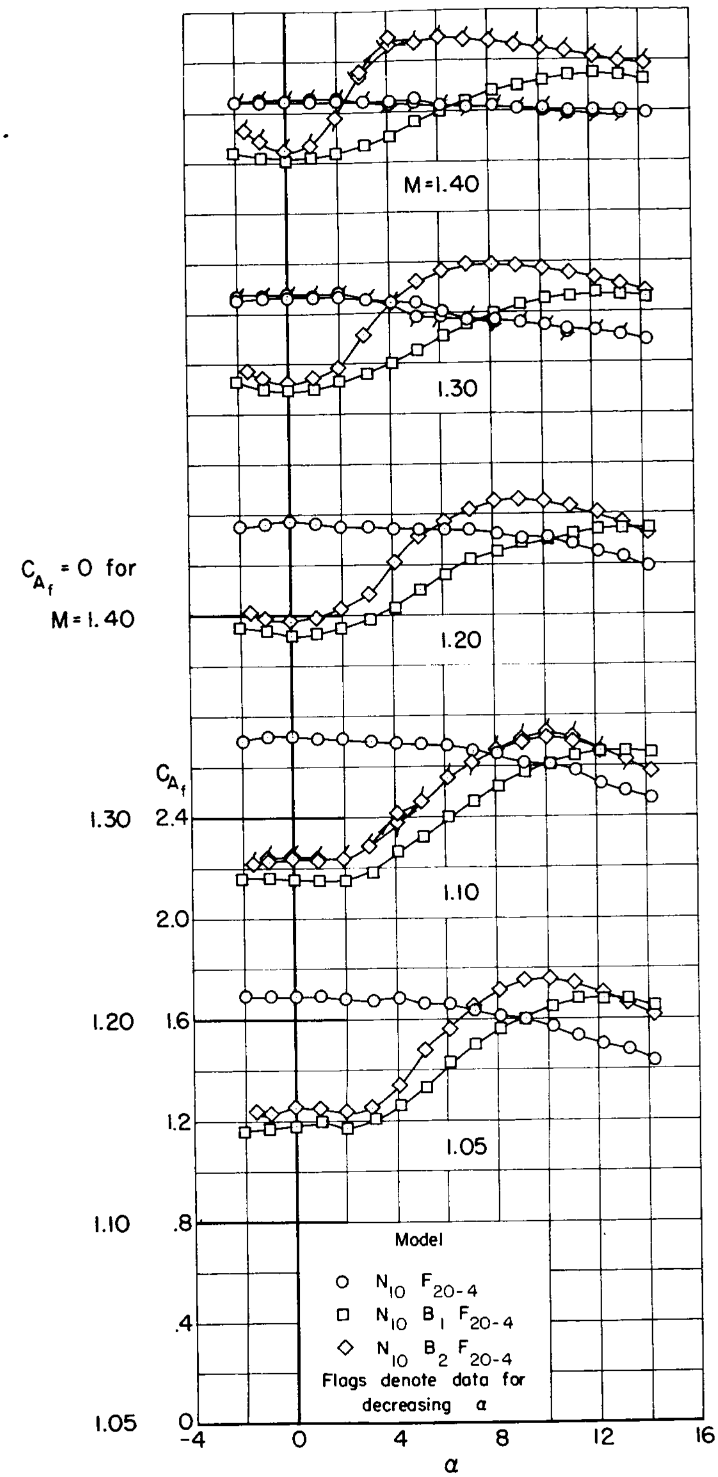


(f) Forebody axial-force coefficient; M = 1.05 to 1.40.

Figure 9.- Continued.

[redacted]

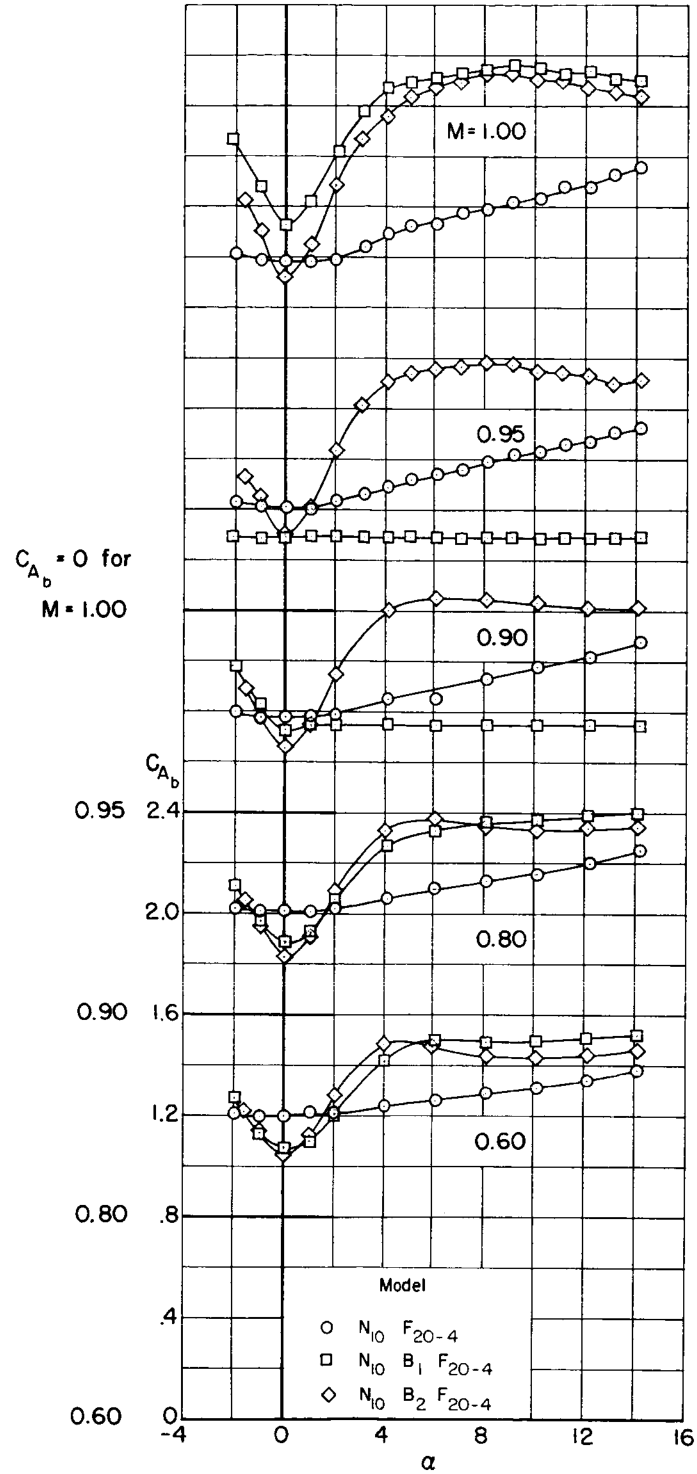


(g) Base axial-force coefficient; M = 0.60 to 1.00.

Figure 9.- Continued.

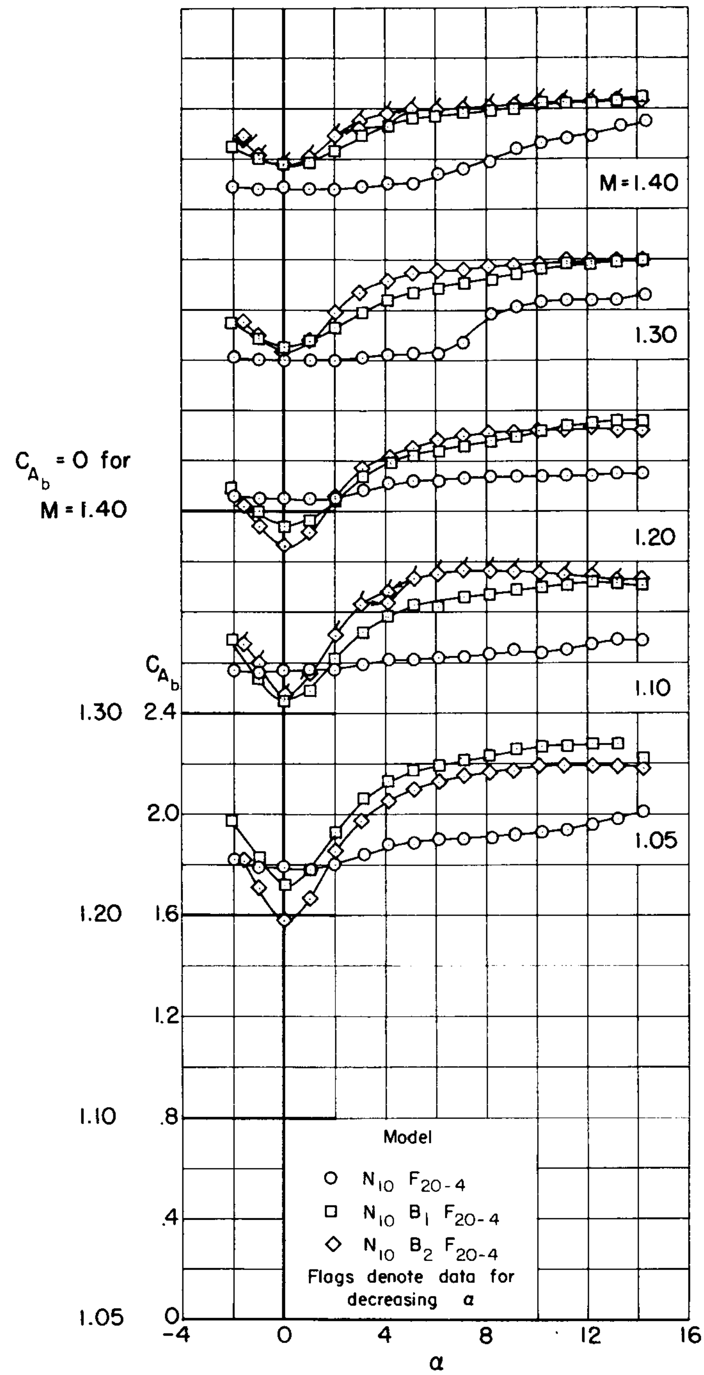


(h) Base axial-force coefficient; M = 1.05 to 1.40.

Figure 9.- Concluded.

A
3
3
0

A
3
3
0

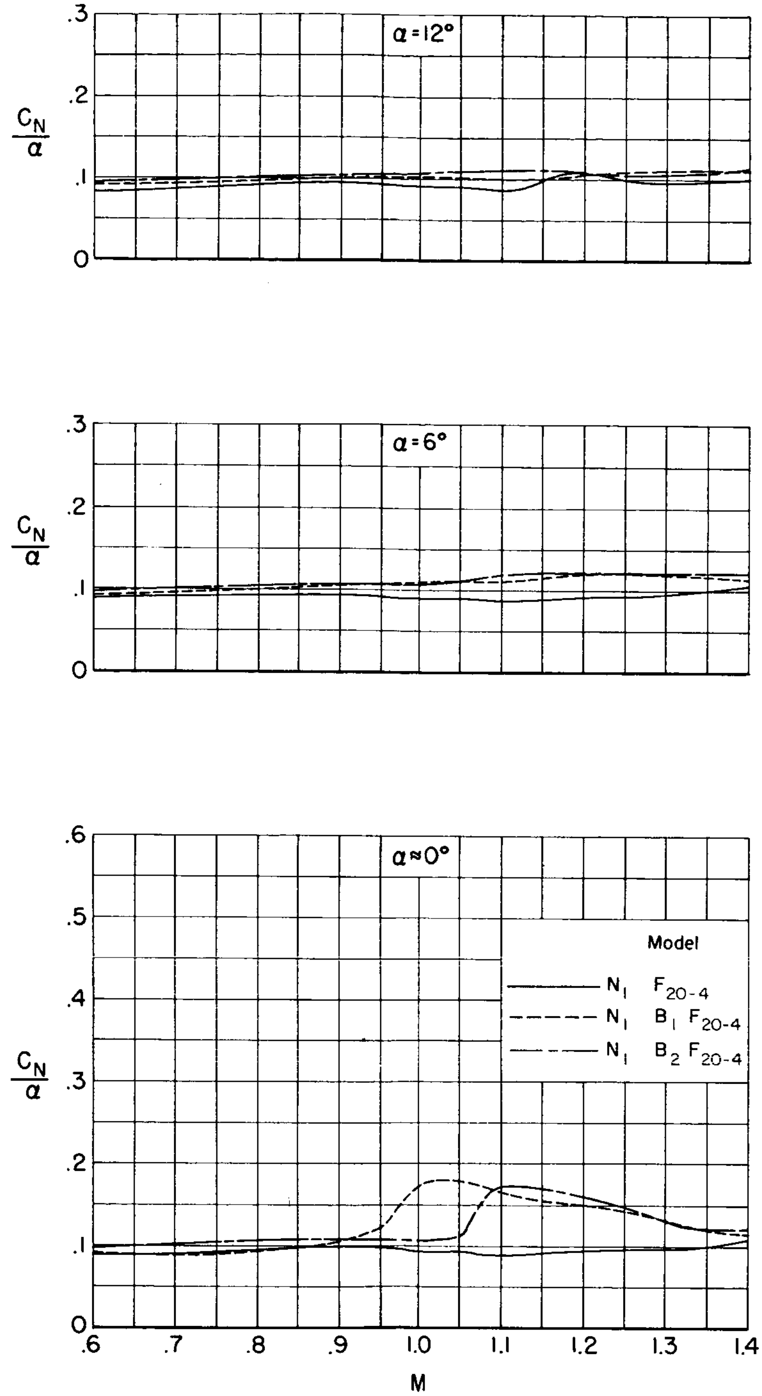


(a) Models with the $N_1$ nose.

Figure 10.- Effects of centerbody length on the normal-force parameter for models with the same nose shape.

C[redacted]

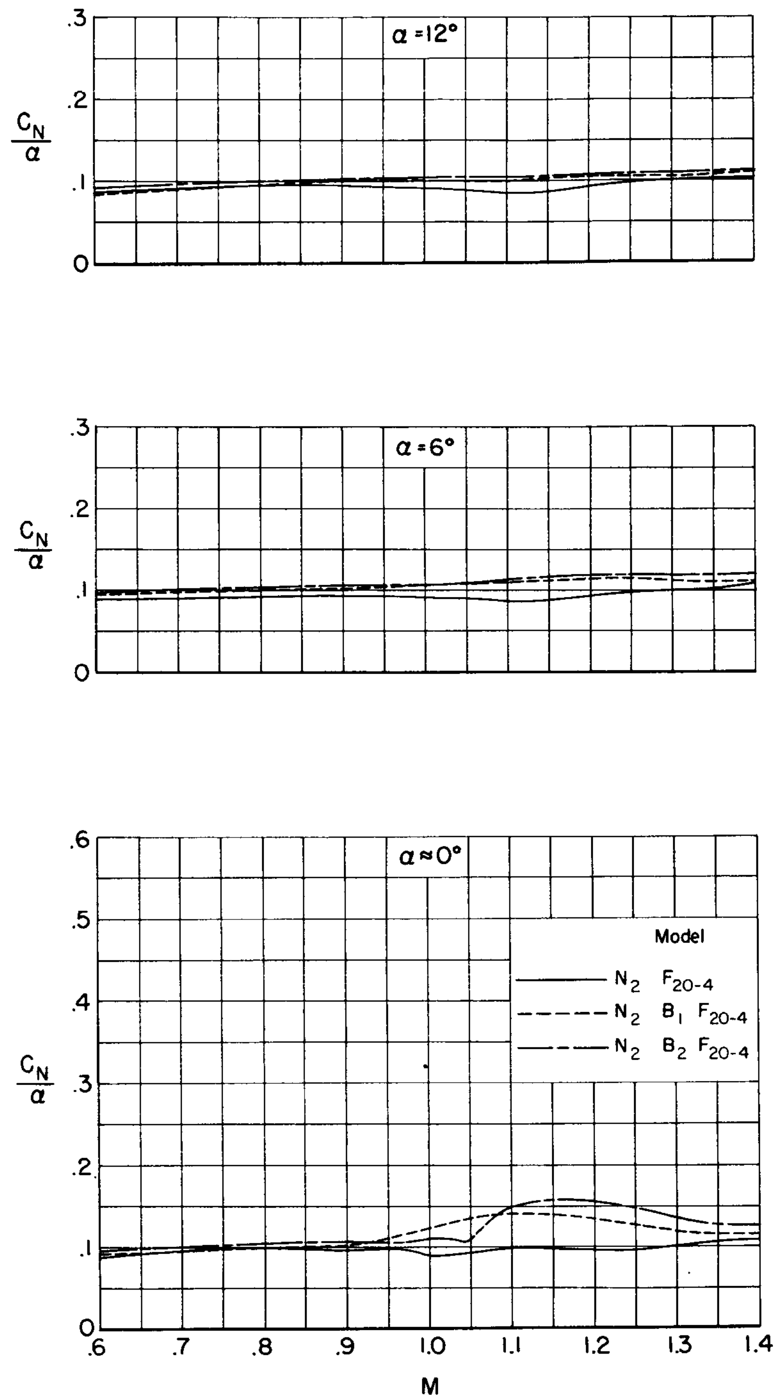


(b) Models with the $N_2$ nose.

Figure 10.- Continued.

[redacted]AL

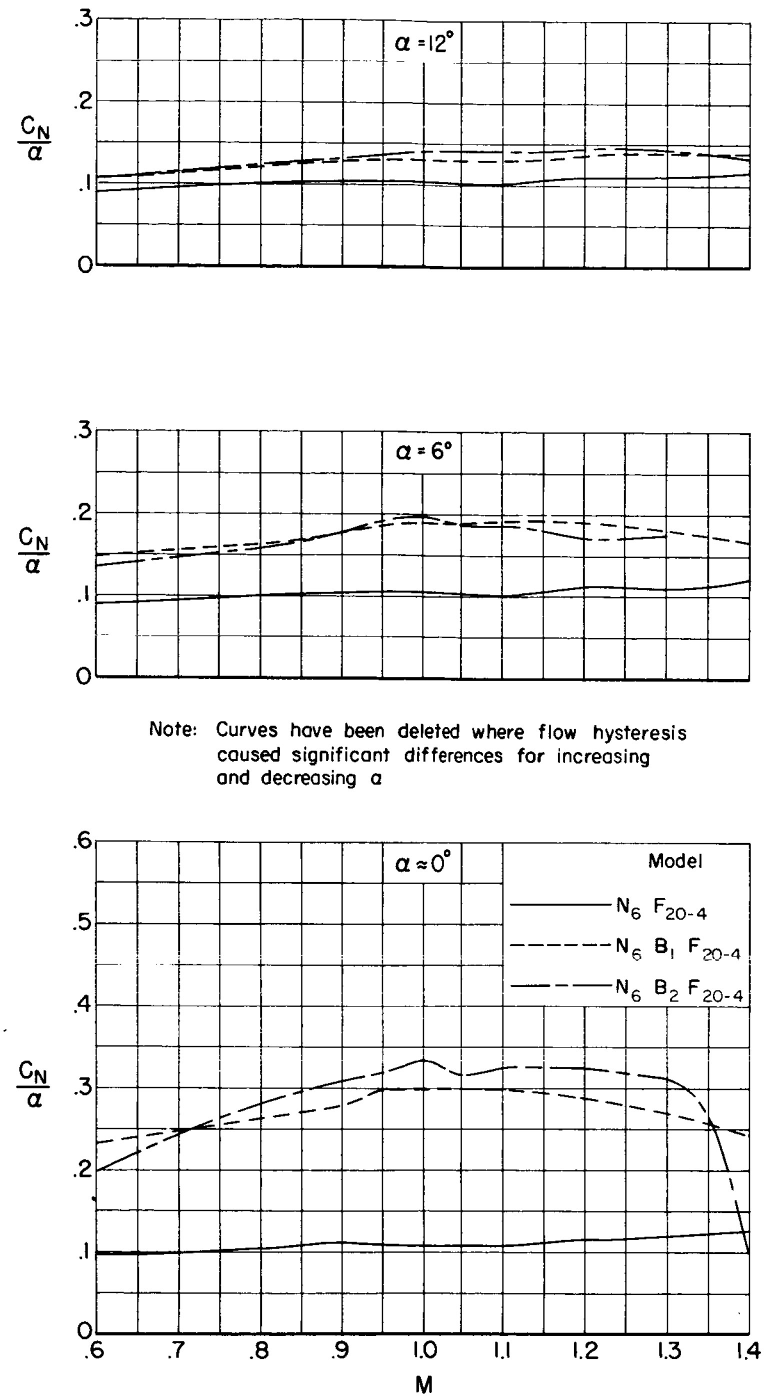


(c) Models with the $N_6$ nose.

Figure 10.- Continued.

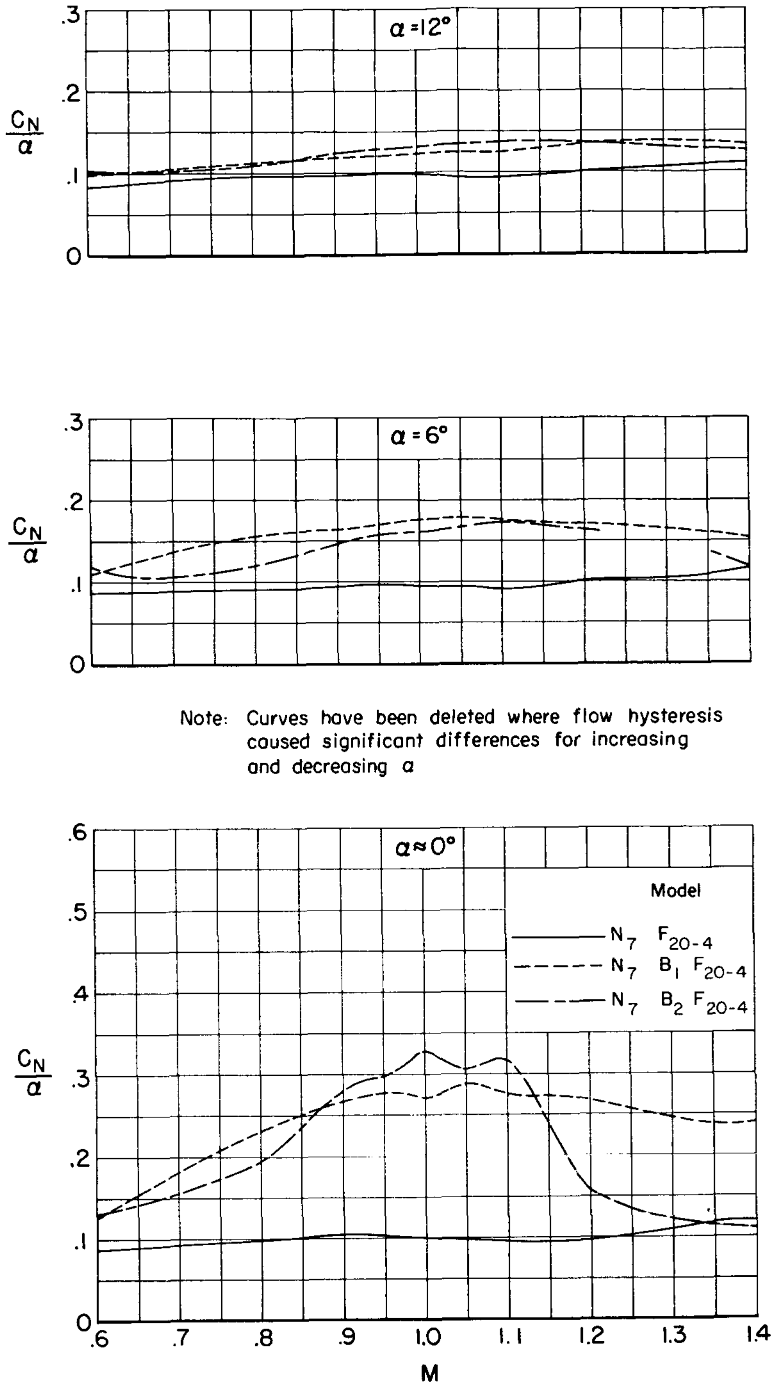


(d) Models with the $N_7$ nose.

Figure 10.- Continued.

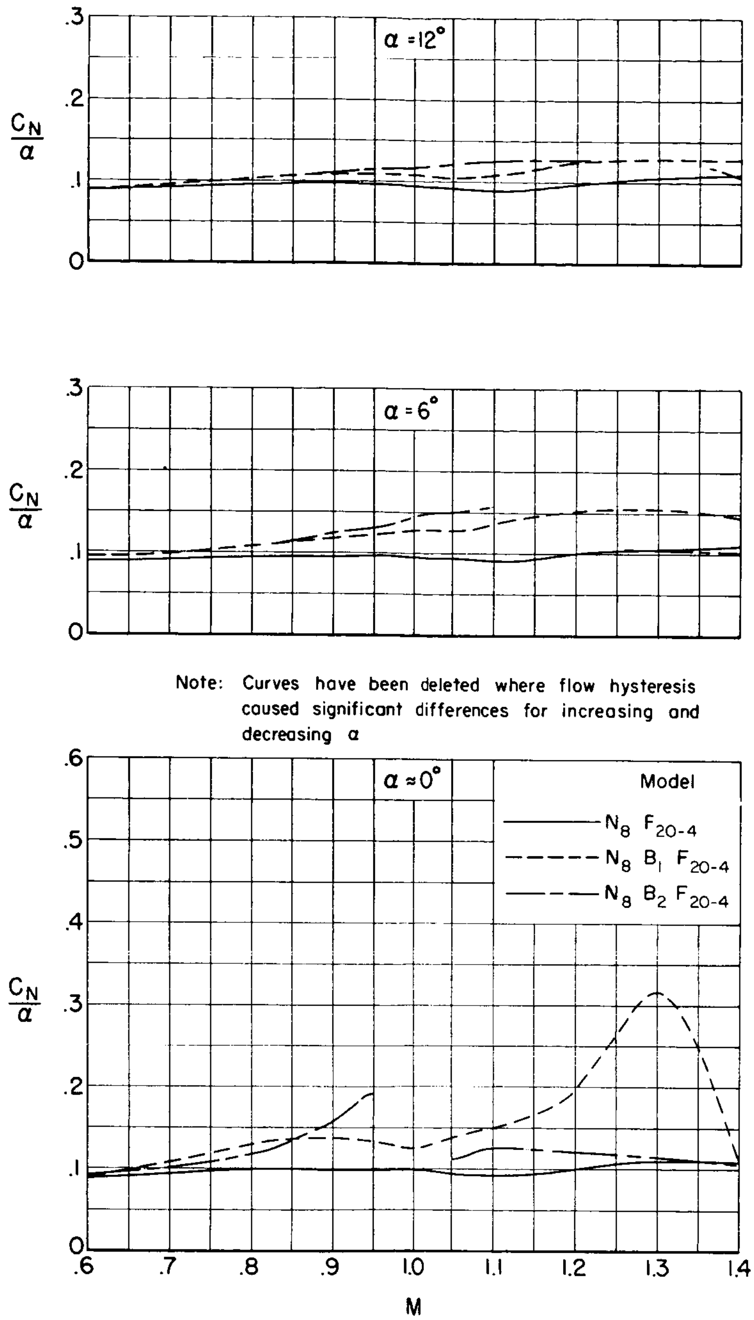


(e) Models with the $N_8$ nose.

Figure 10.- Continued.

[redacted]

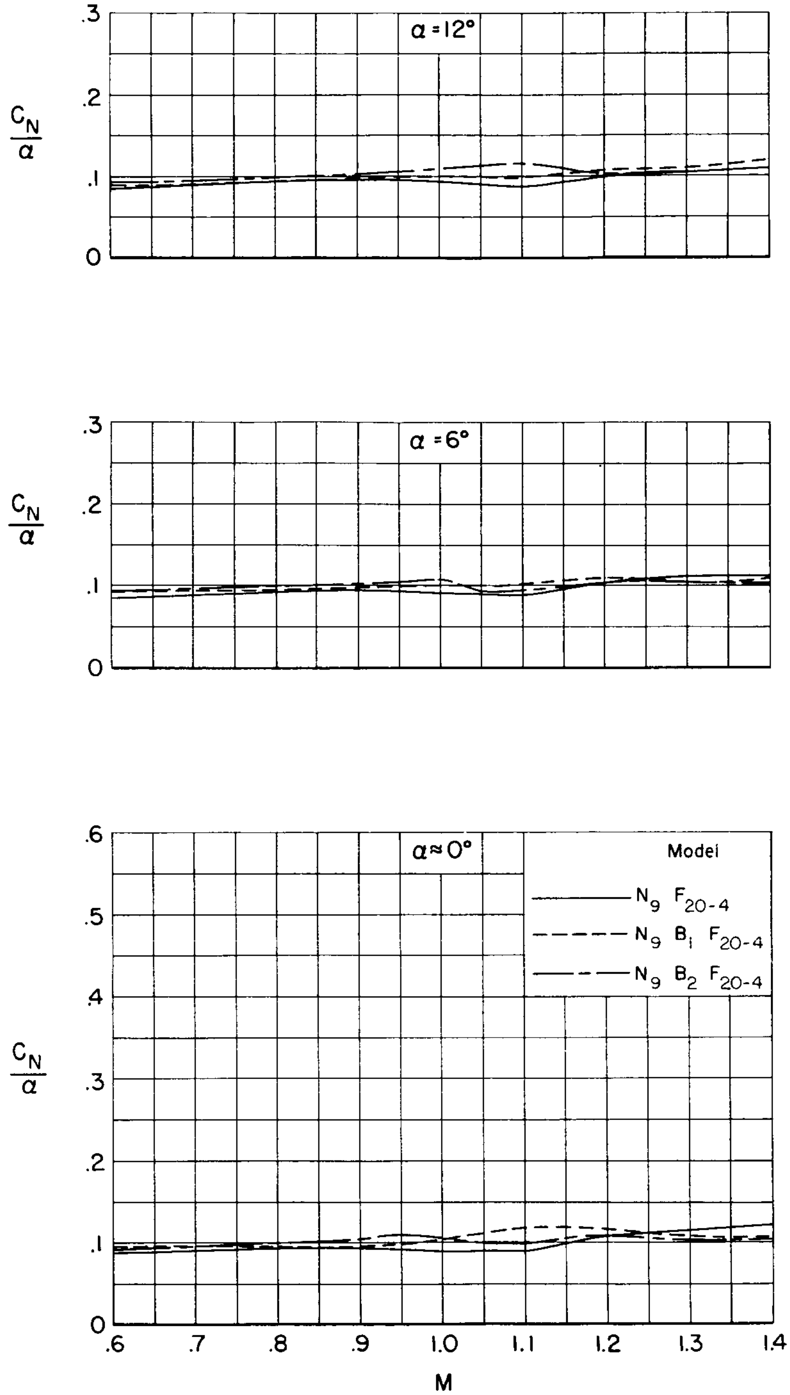


(f) Models with the $N_9$ nose.

Figure 10.- Continued.

[redacted]

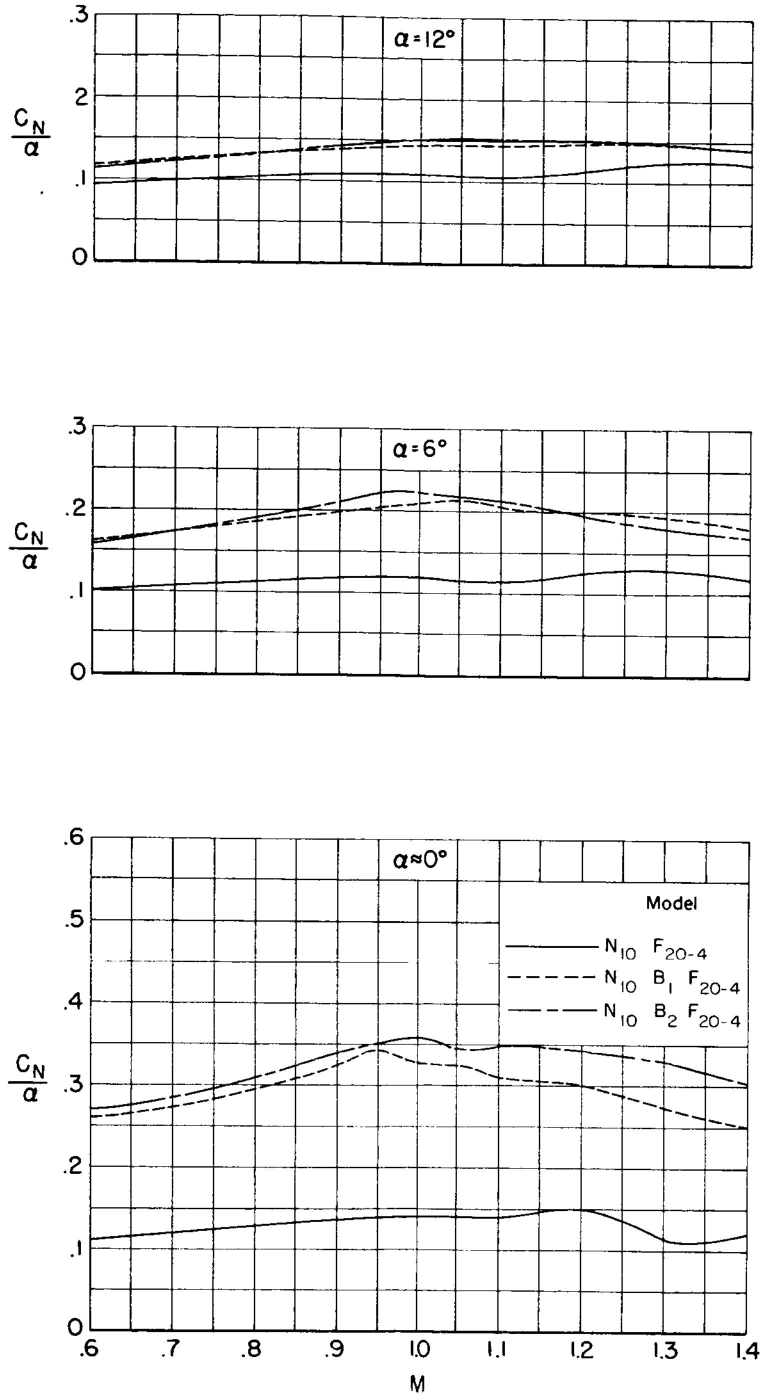


(g) Models with the $N_{10}$ nose.

Figure 10.- Concluded.

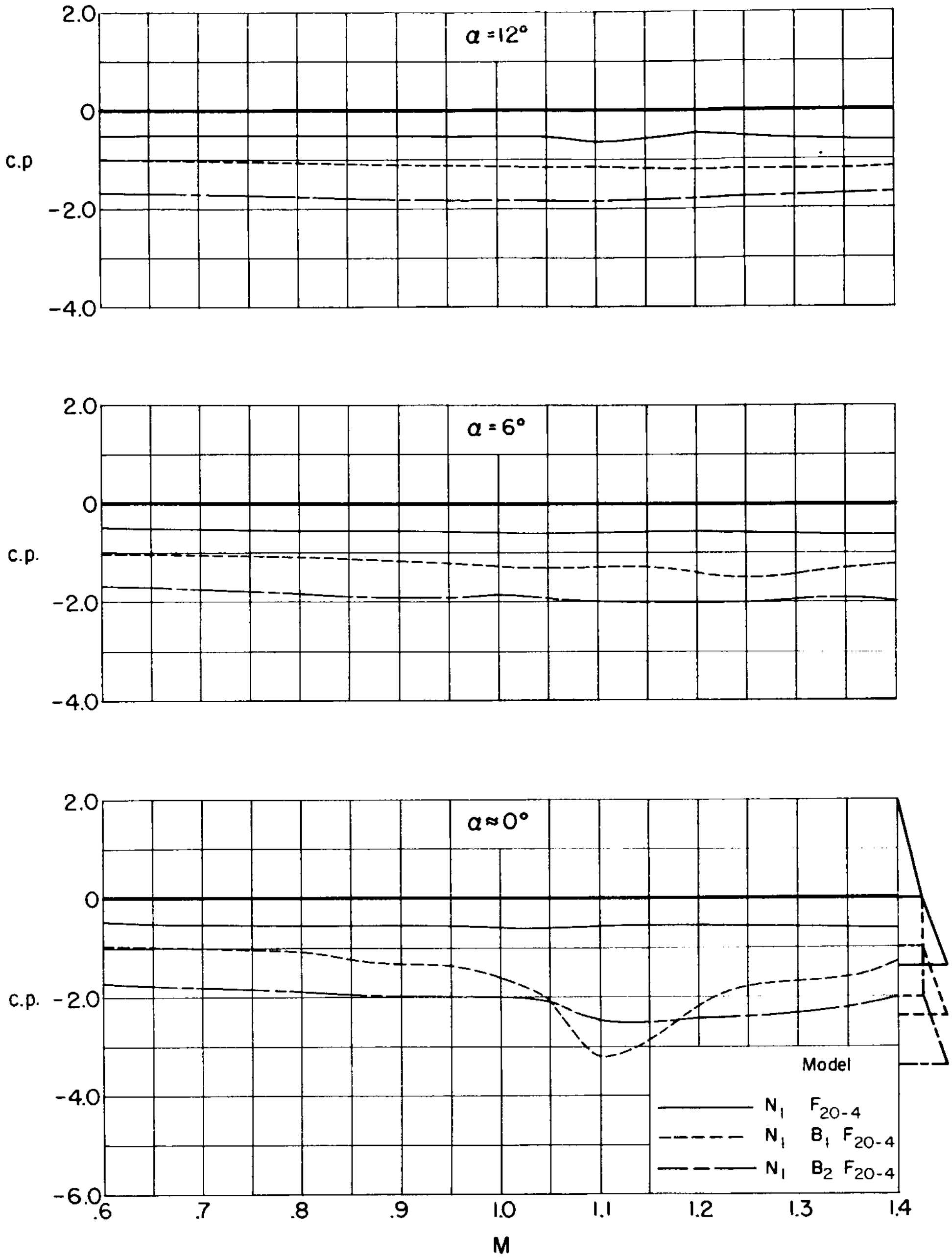


(a) Models with the $N_1$ nose.

Figure 11.- Effects of centerbody length on the center of pressure for models with the same nose shape.

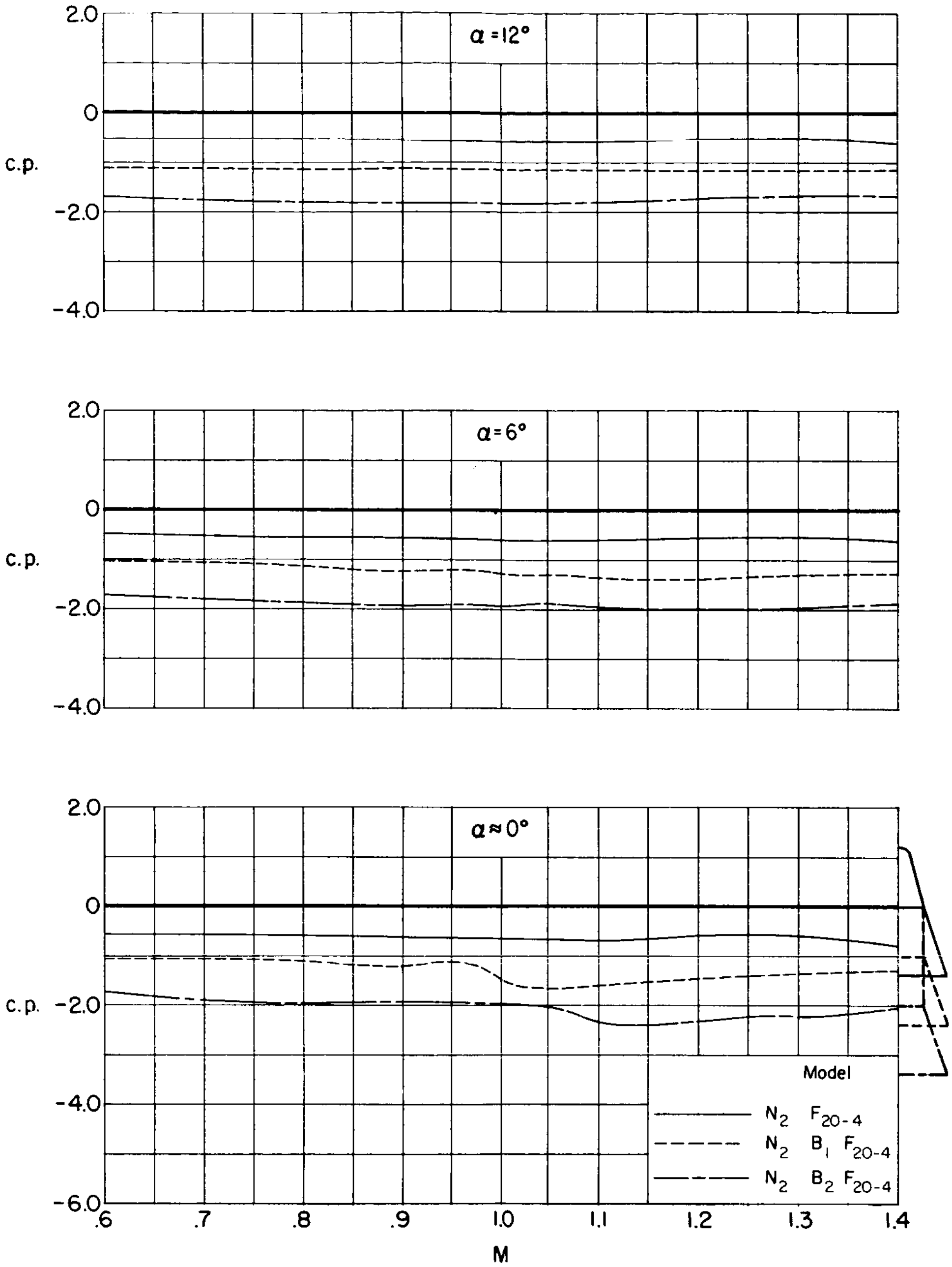


(b) Models with the $N_2$ nose.

Figure 11.- Continued.

[redacted]

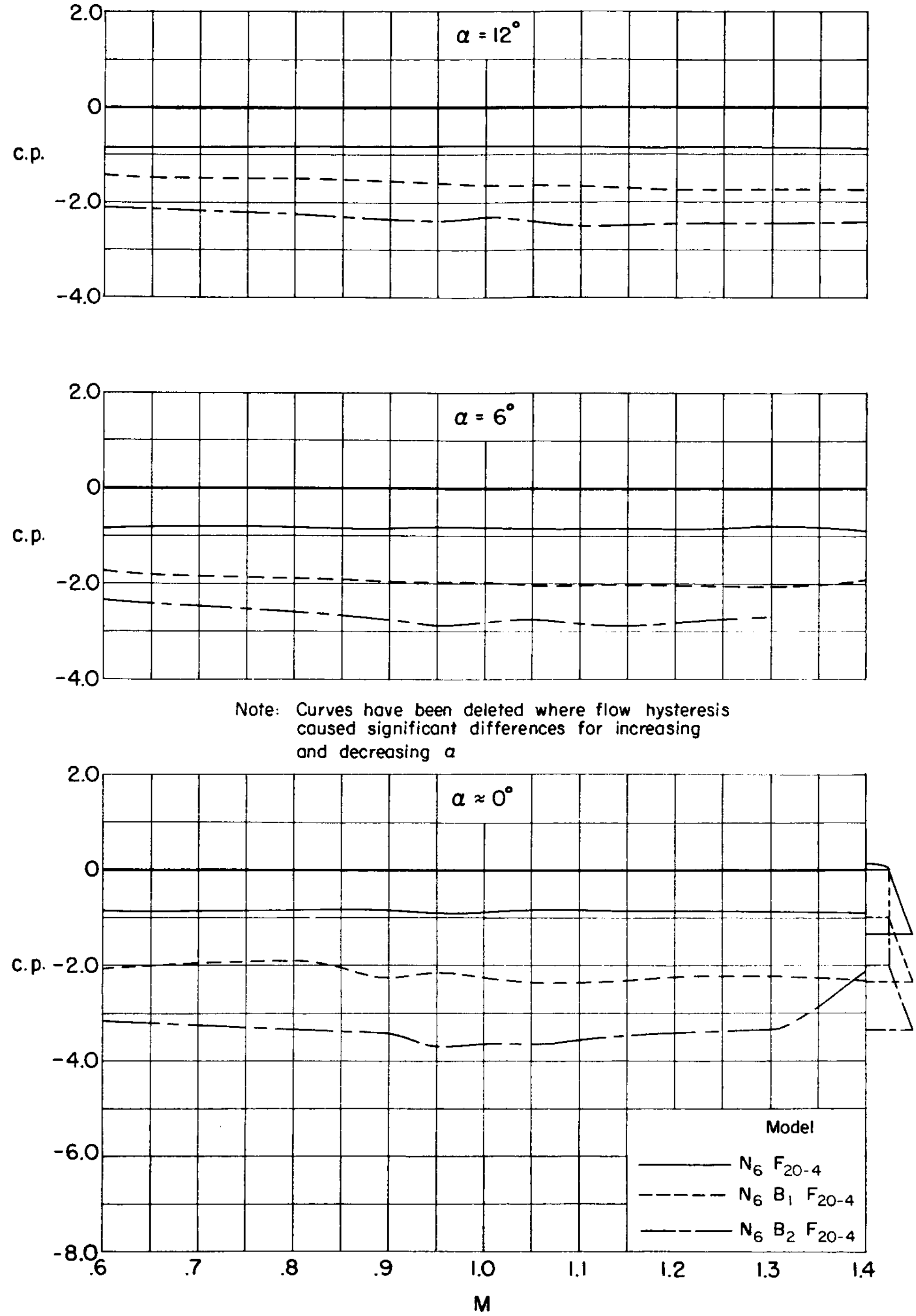


(c) Models with the $N_6$ nose.

Figure 11.- Continued.

A
3
3
0

[redacted]

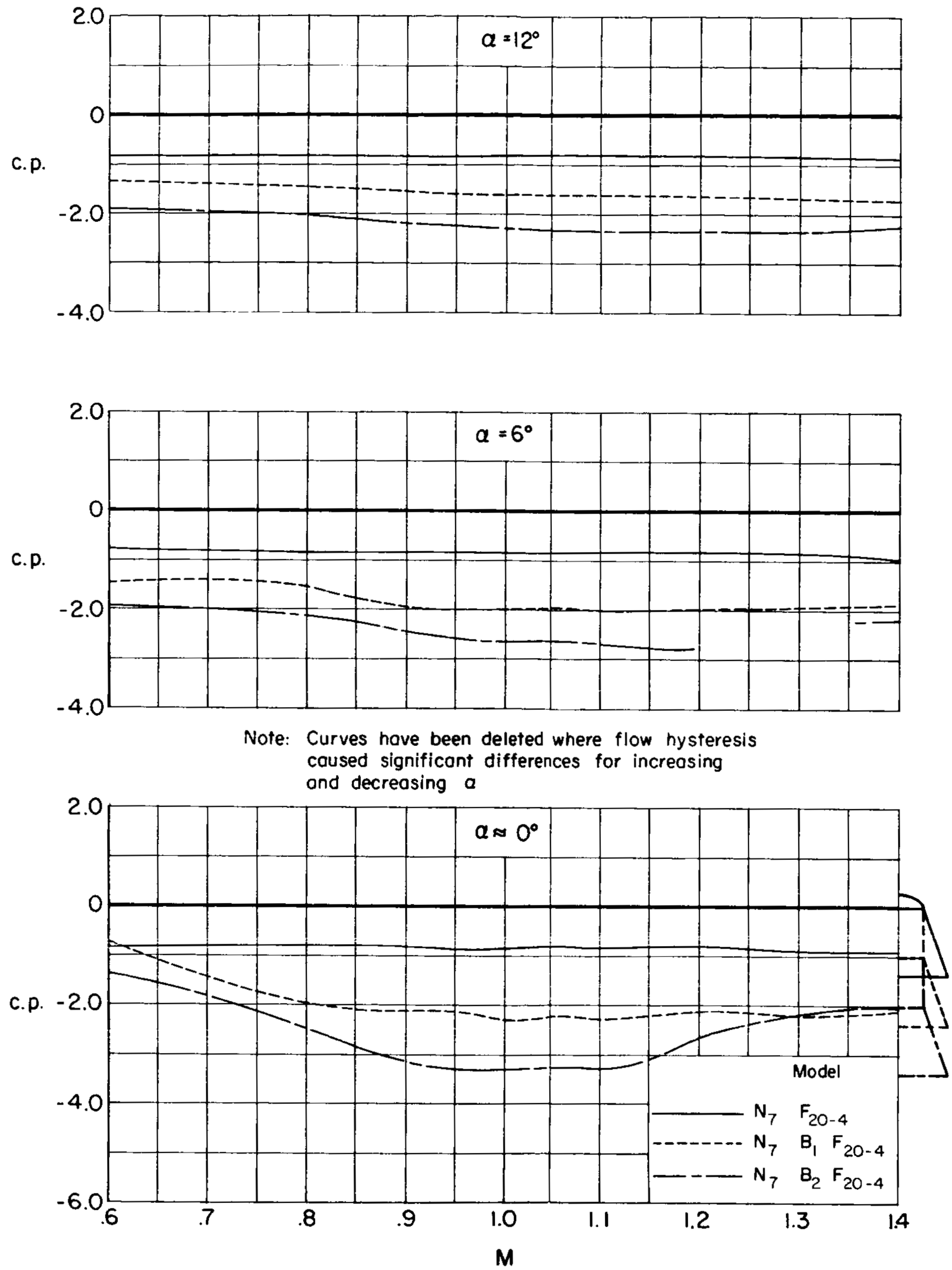


(d) Models with the $N_7$ nose.

Figure 11.- Continued.

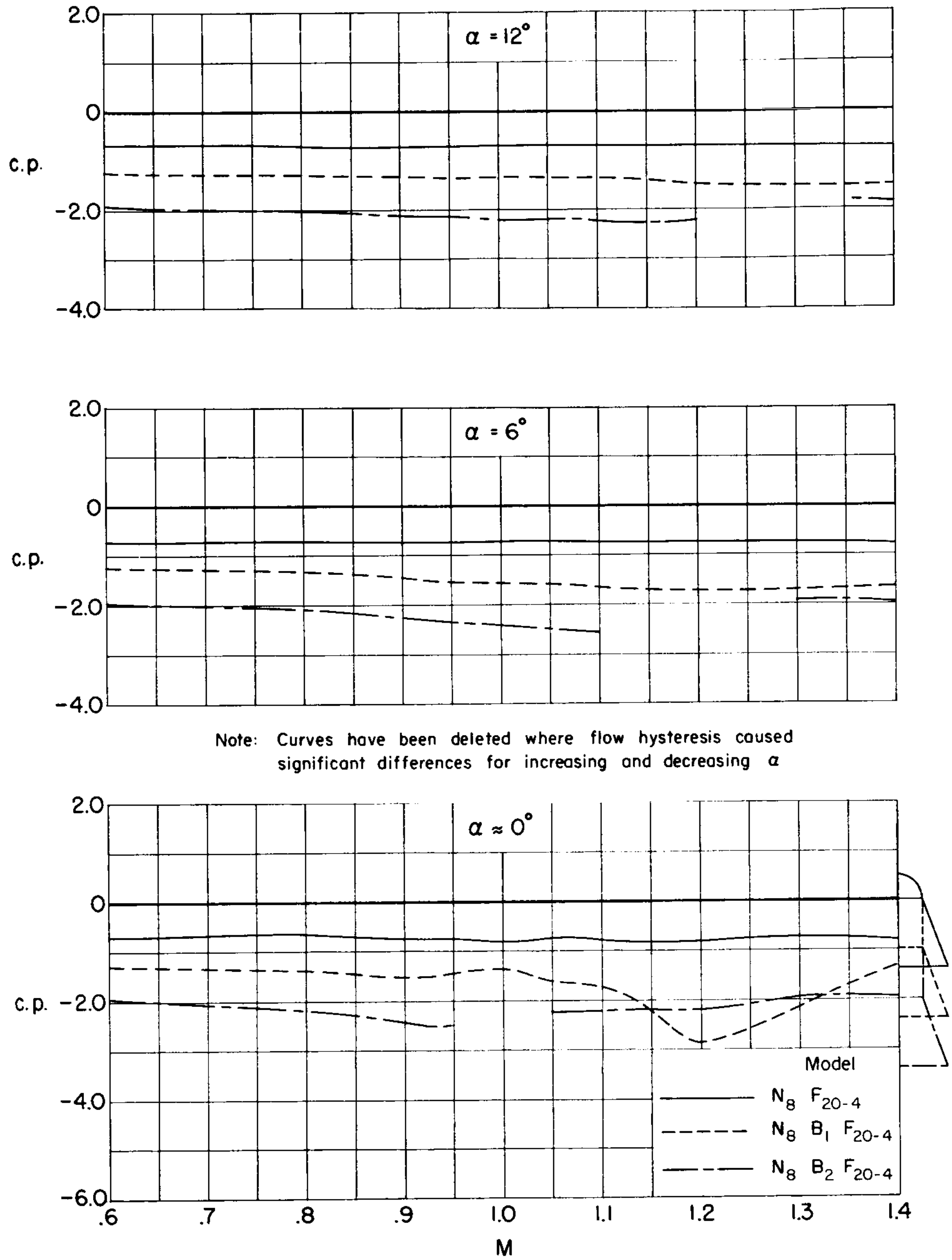


(e) Models with the $N_8$ nose.

Figure 11.- Continued.

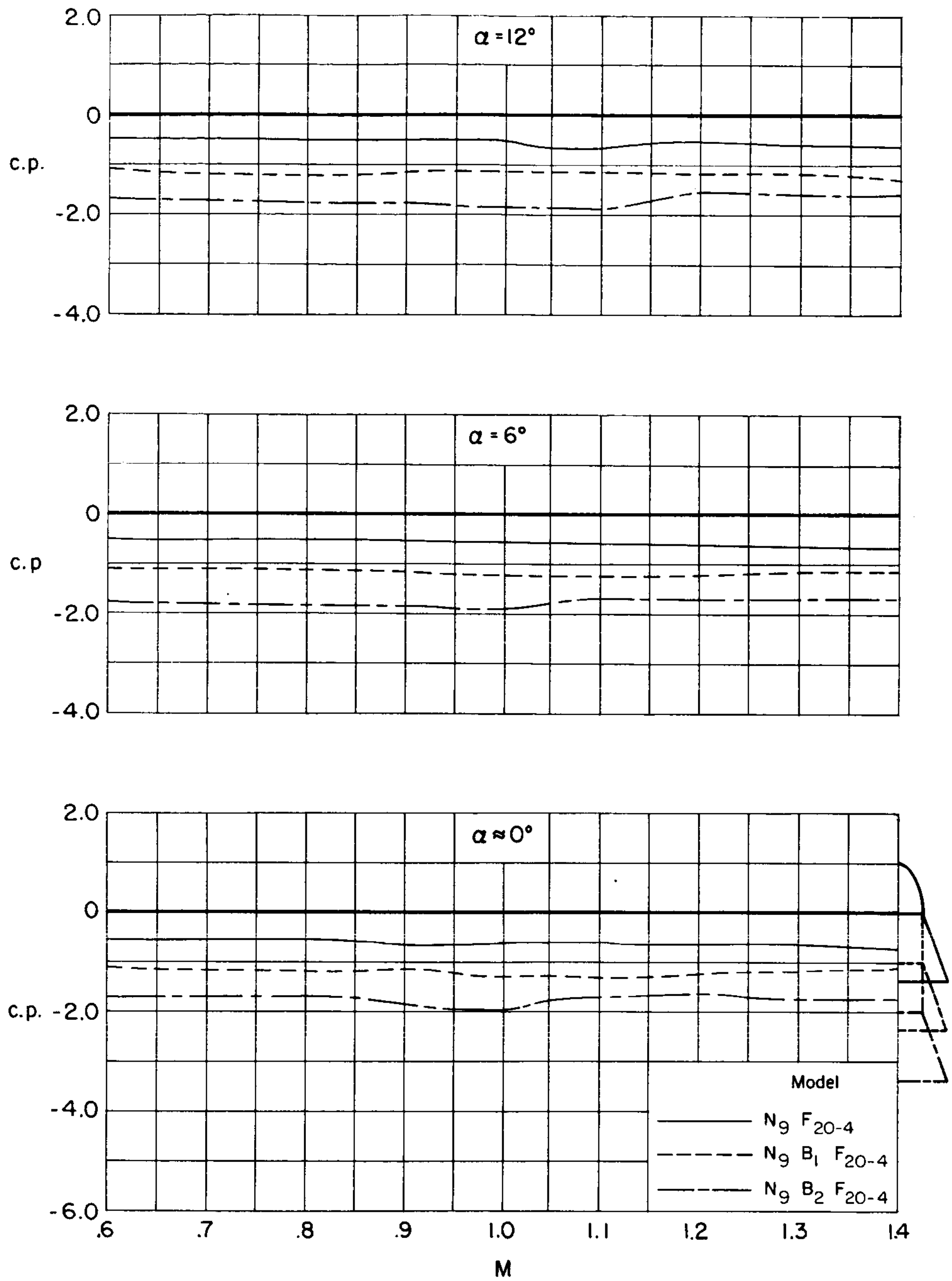


(f) Models with the $N_9$ nose.

Figure 11.- Continued.

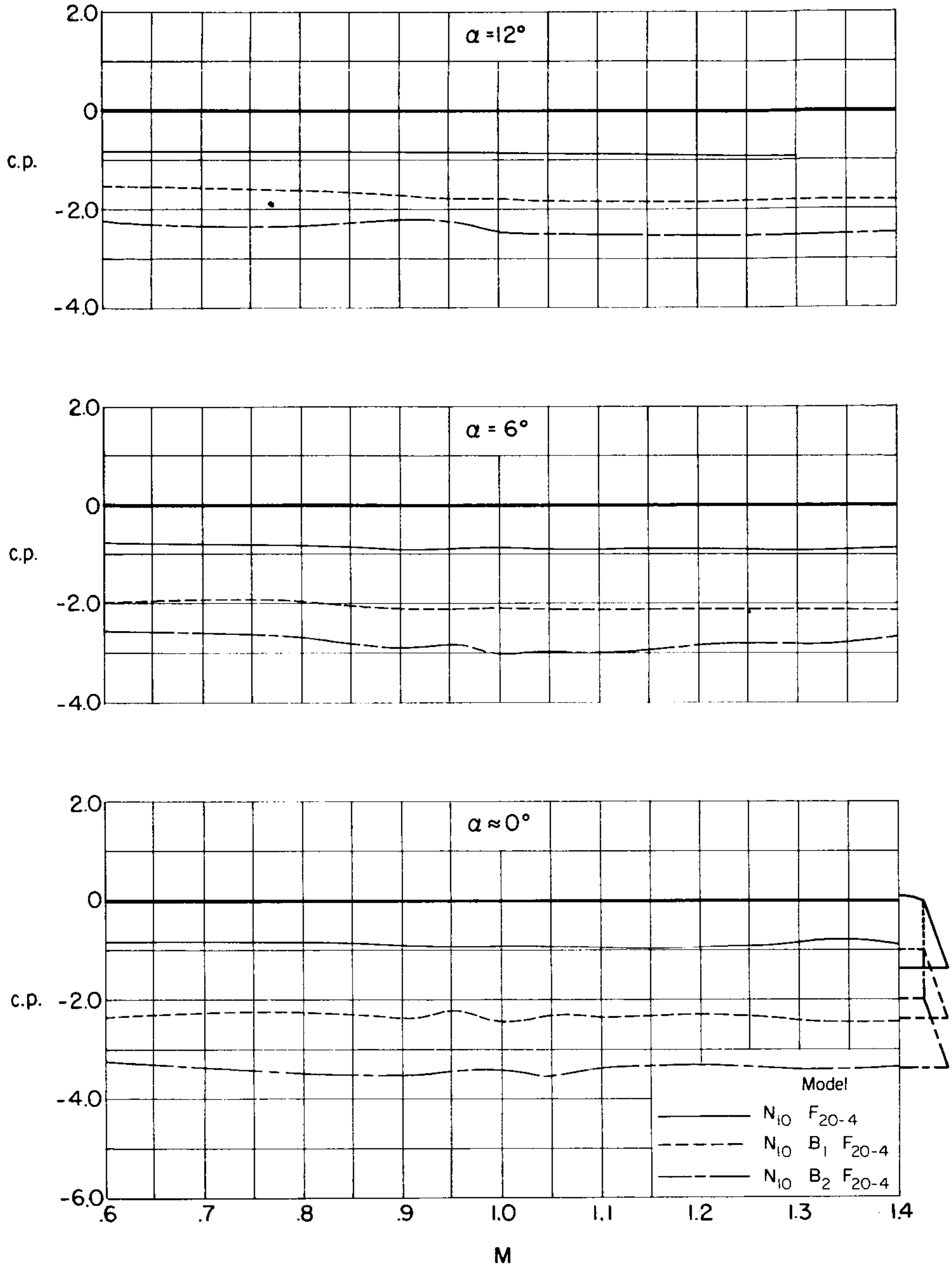


(g) Models with the $N_{10}$ nose.

Figure 11.- Concluded.

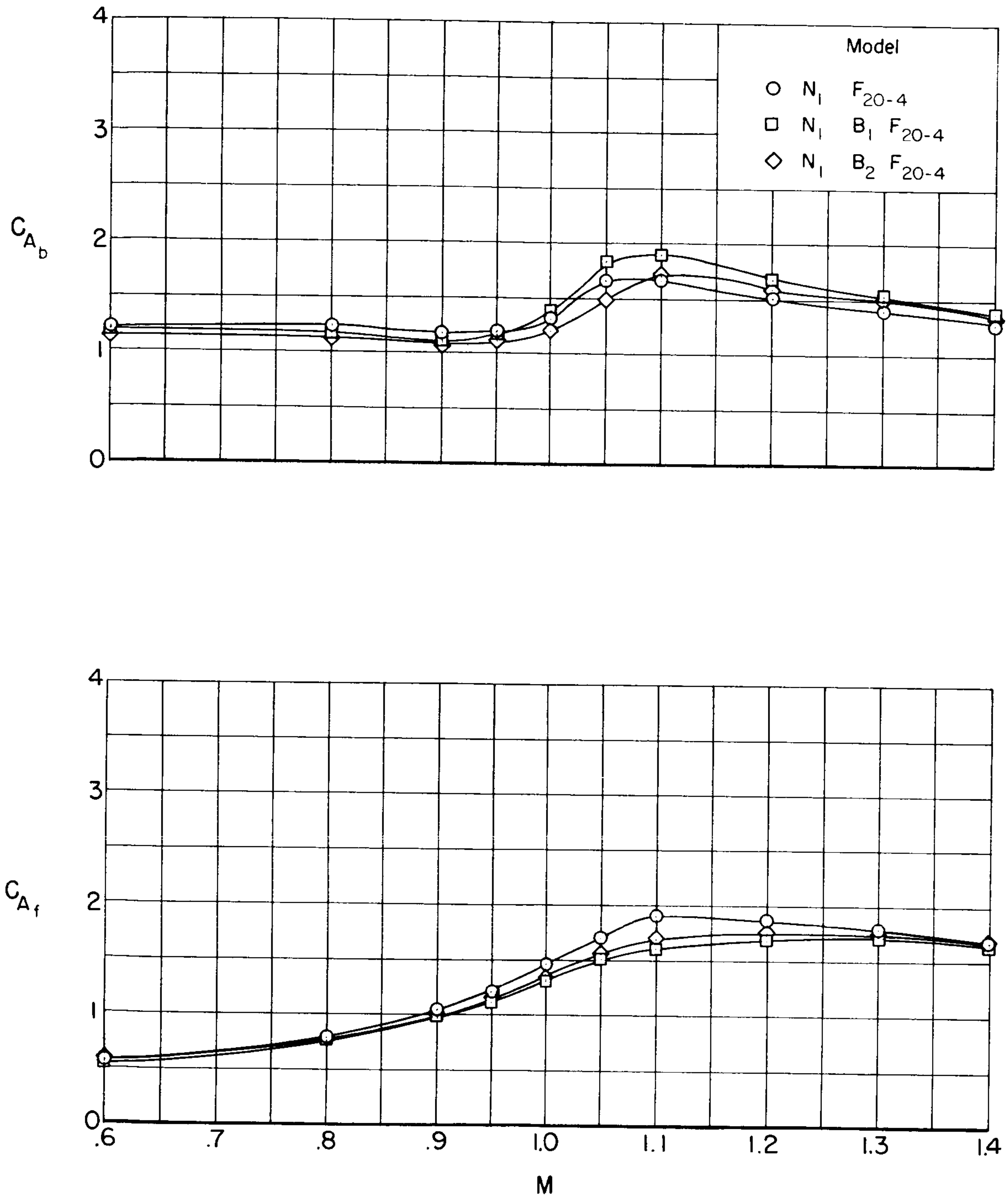


(a) Models with the $N_1$ nose.

Figure 12.- Effects of centerbody length on the forebody axial force and base axial force at $\alpha = 0^{\circ}$ for models with the same nose shape.

[redacted]

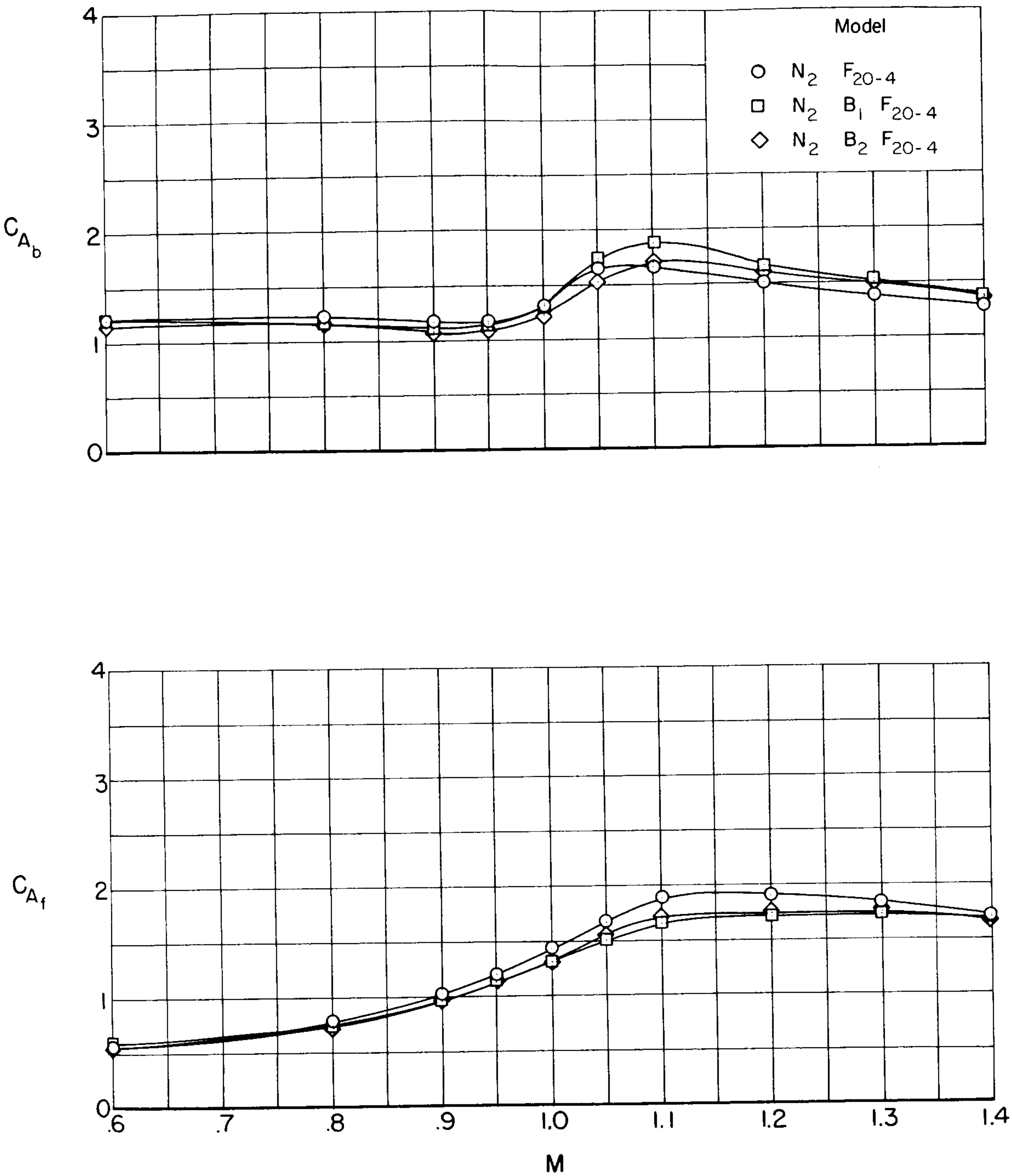


(b) Models with the $N_2$ nose.

Figure 12.- Continued.

A
3
3
0

[redacted]

A330

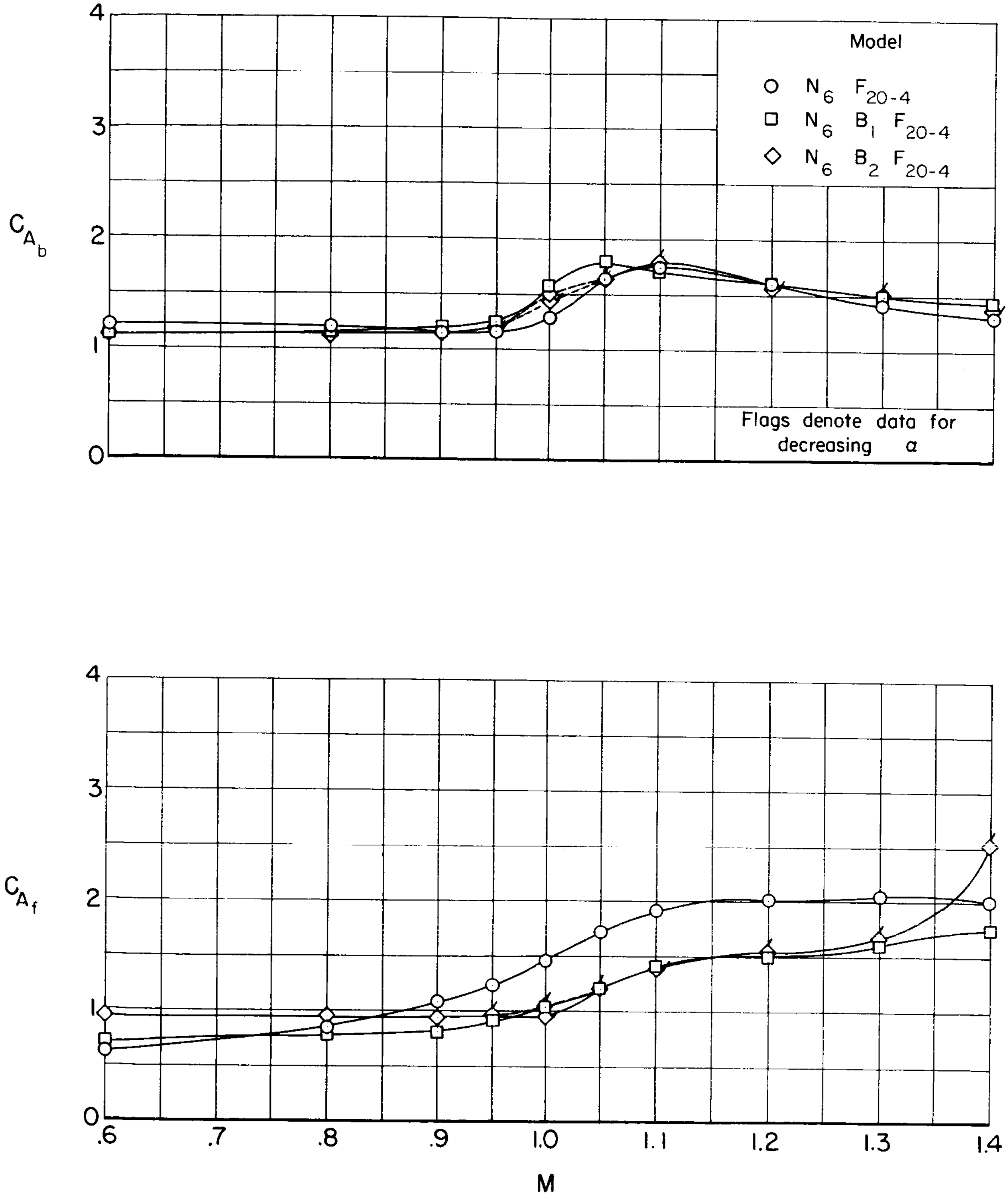


(c) Models with the $N_6$ nose.

Figure 12.- Continued.

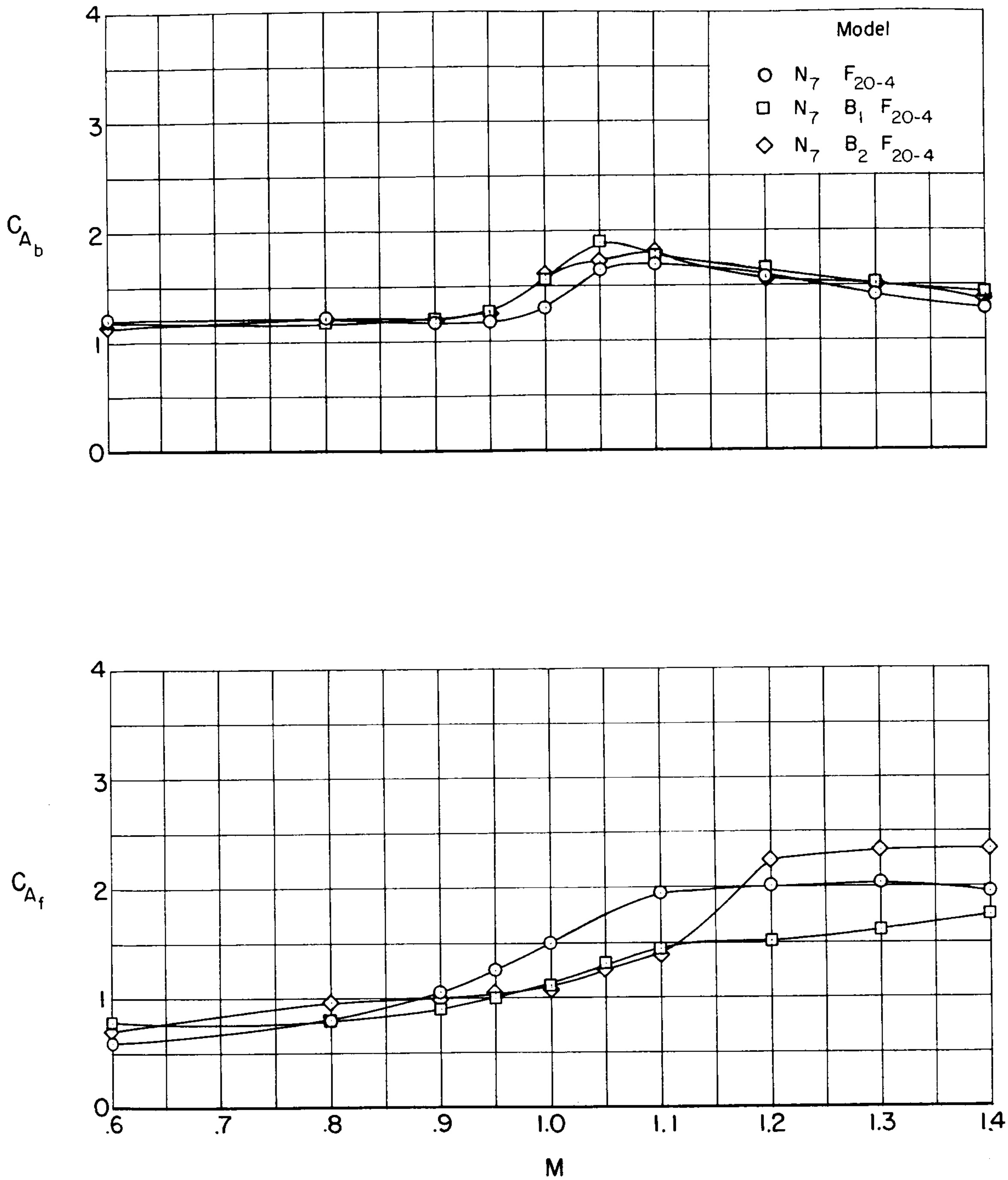


(d) Models with the $N_7$ nose.

Figure 12.- Continued.

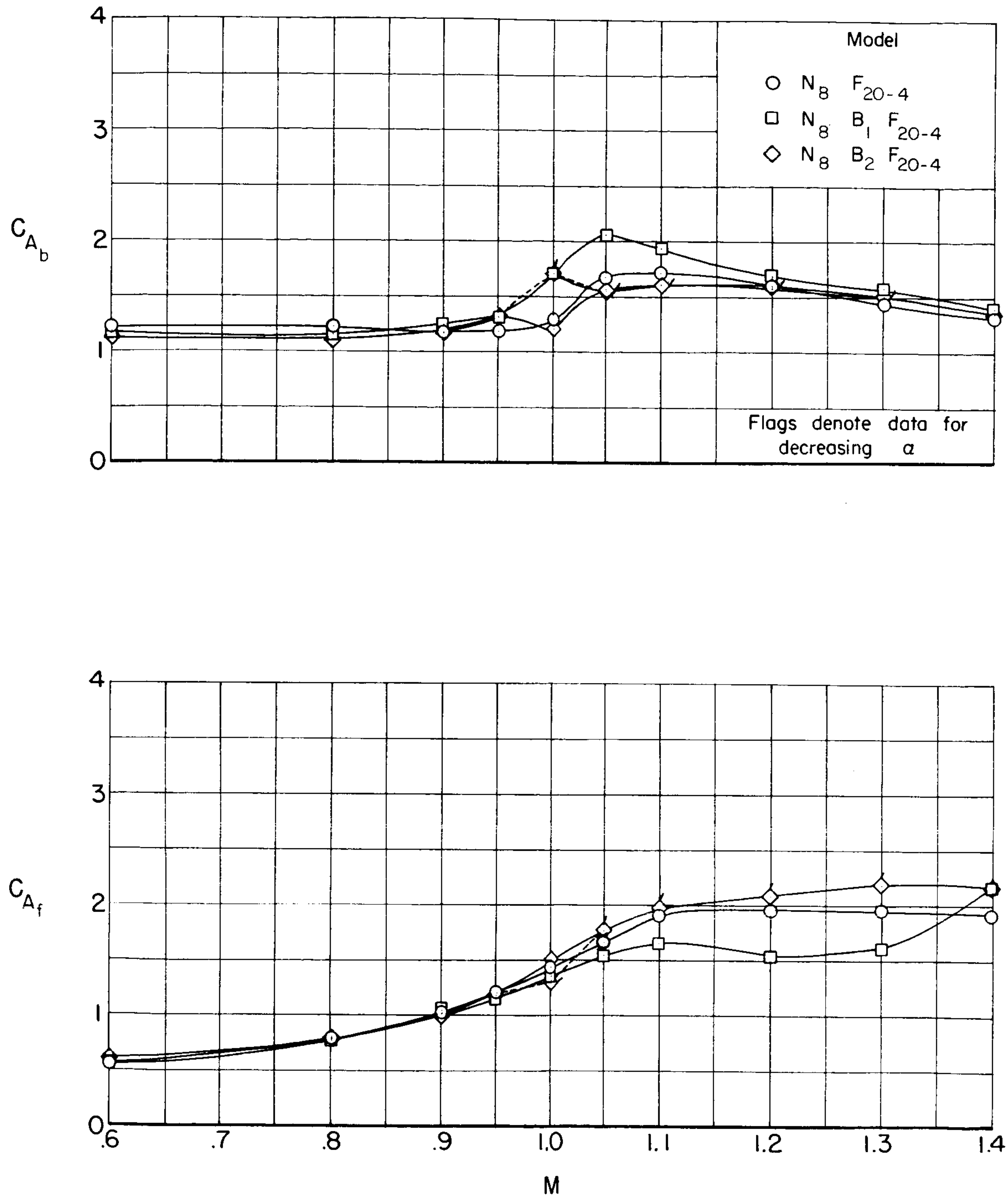


(e) Models with the N8 nose.

Figure 12.- Continued.

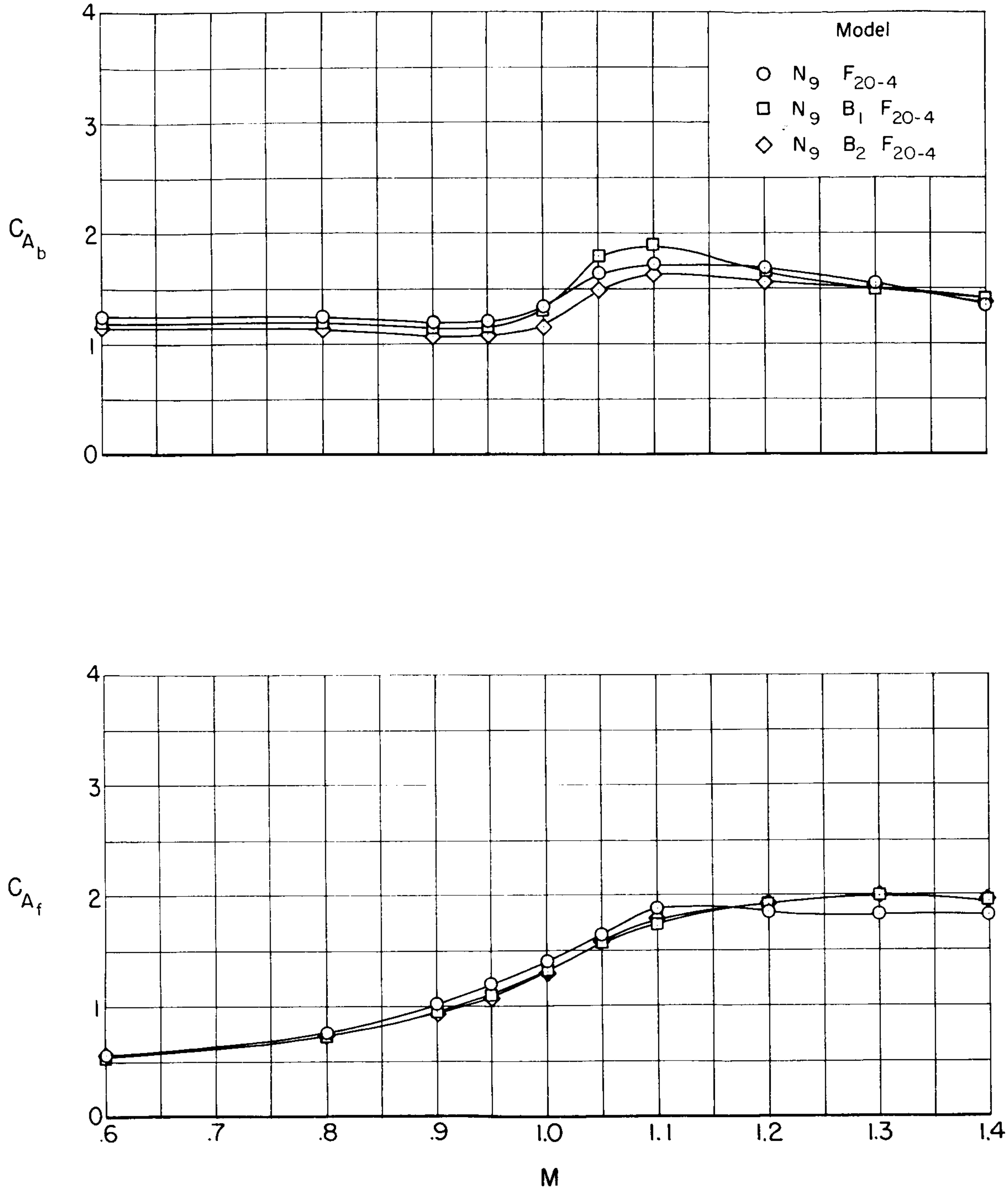


(f) Models with the $N_9$ nose.

Figure 12.- Continued.

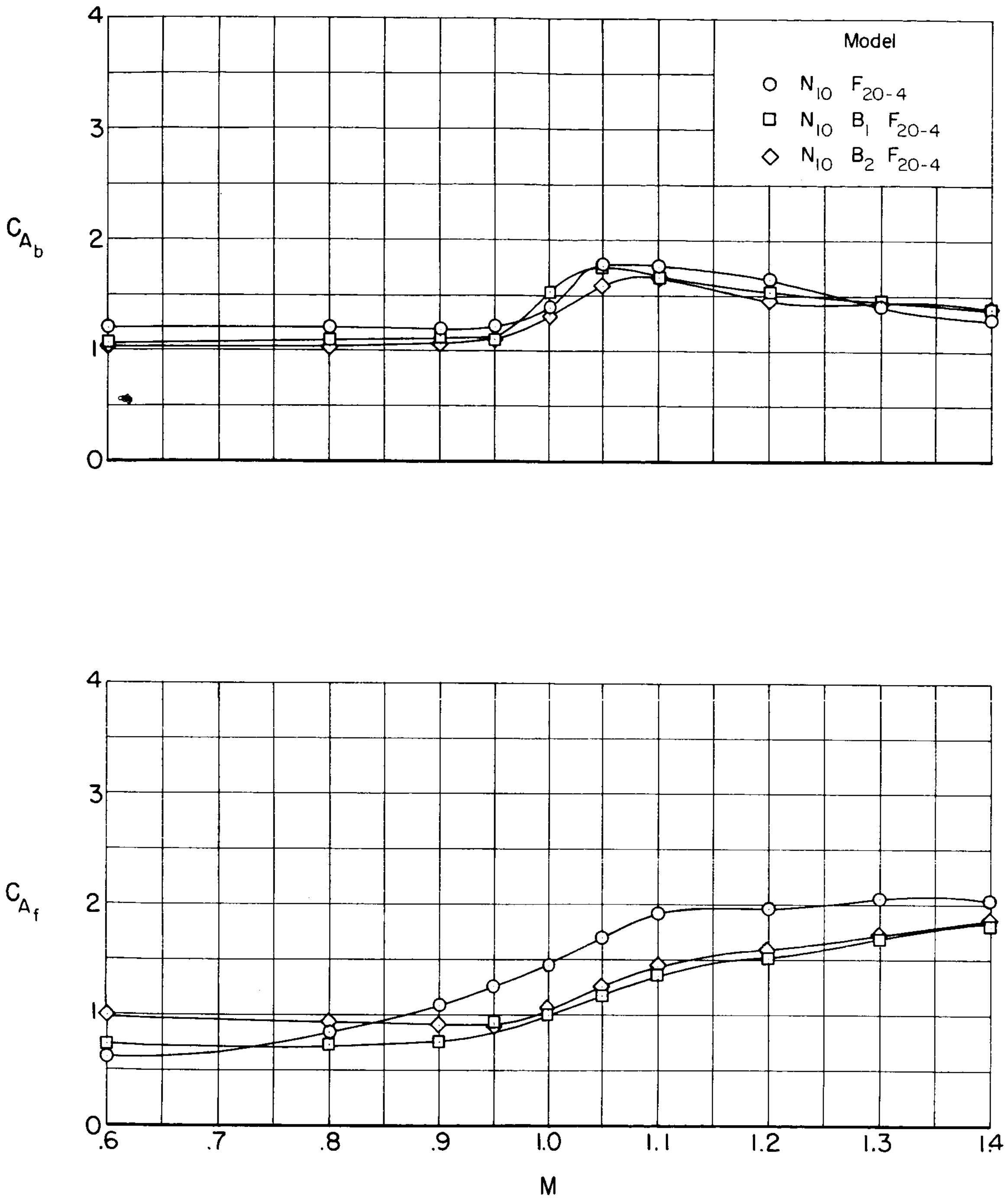


(g) Models with the $N_{10}$ nose.

Figure 12.- Concluded.

[redacted]

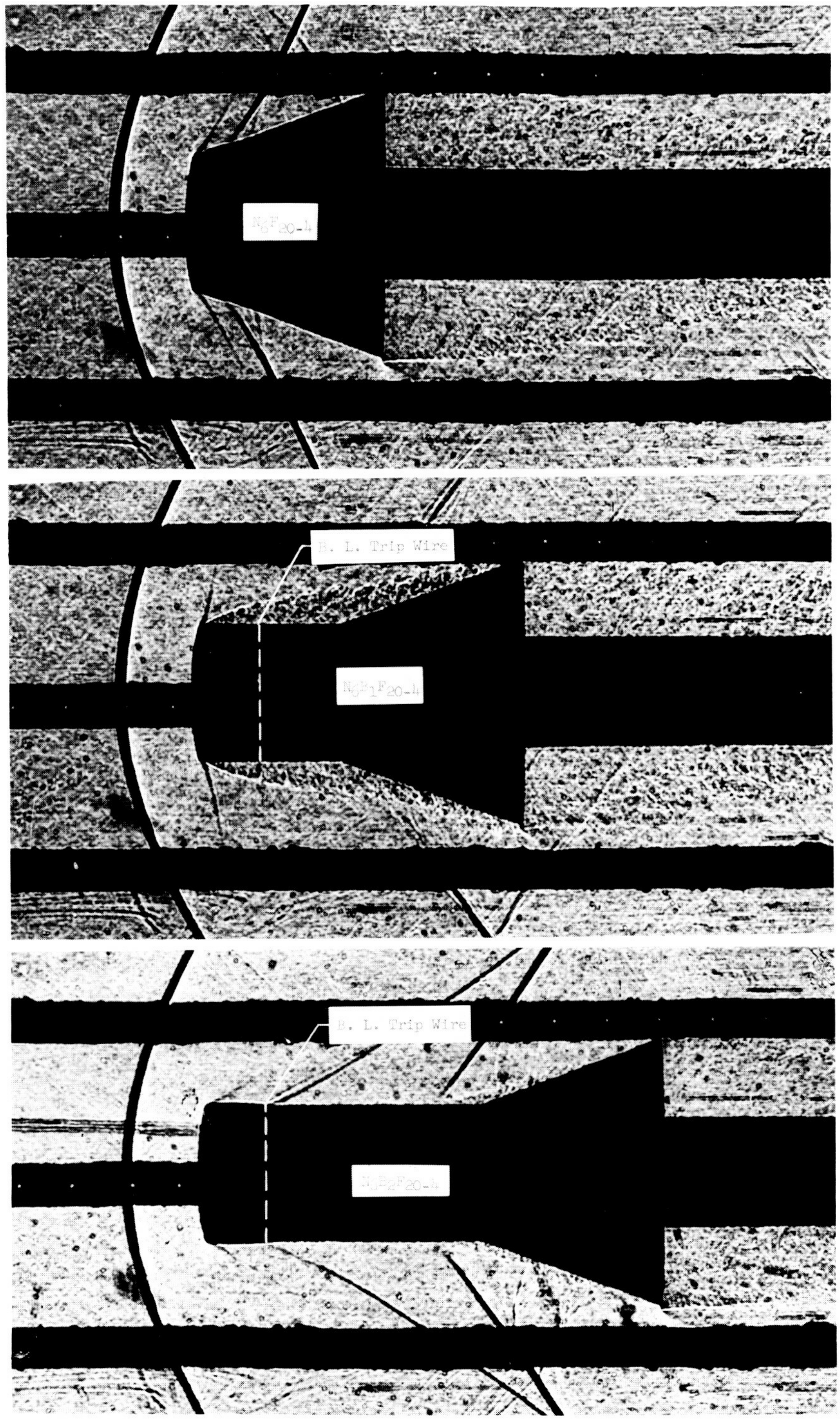


(a) Models with the $N_6$ nose.

Figure 13.- The effect of centerbody length on flow patterns at $M = 1.4$ and $\alpha = 0^{\circ}$.

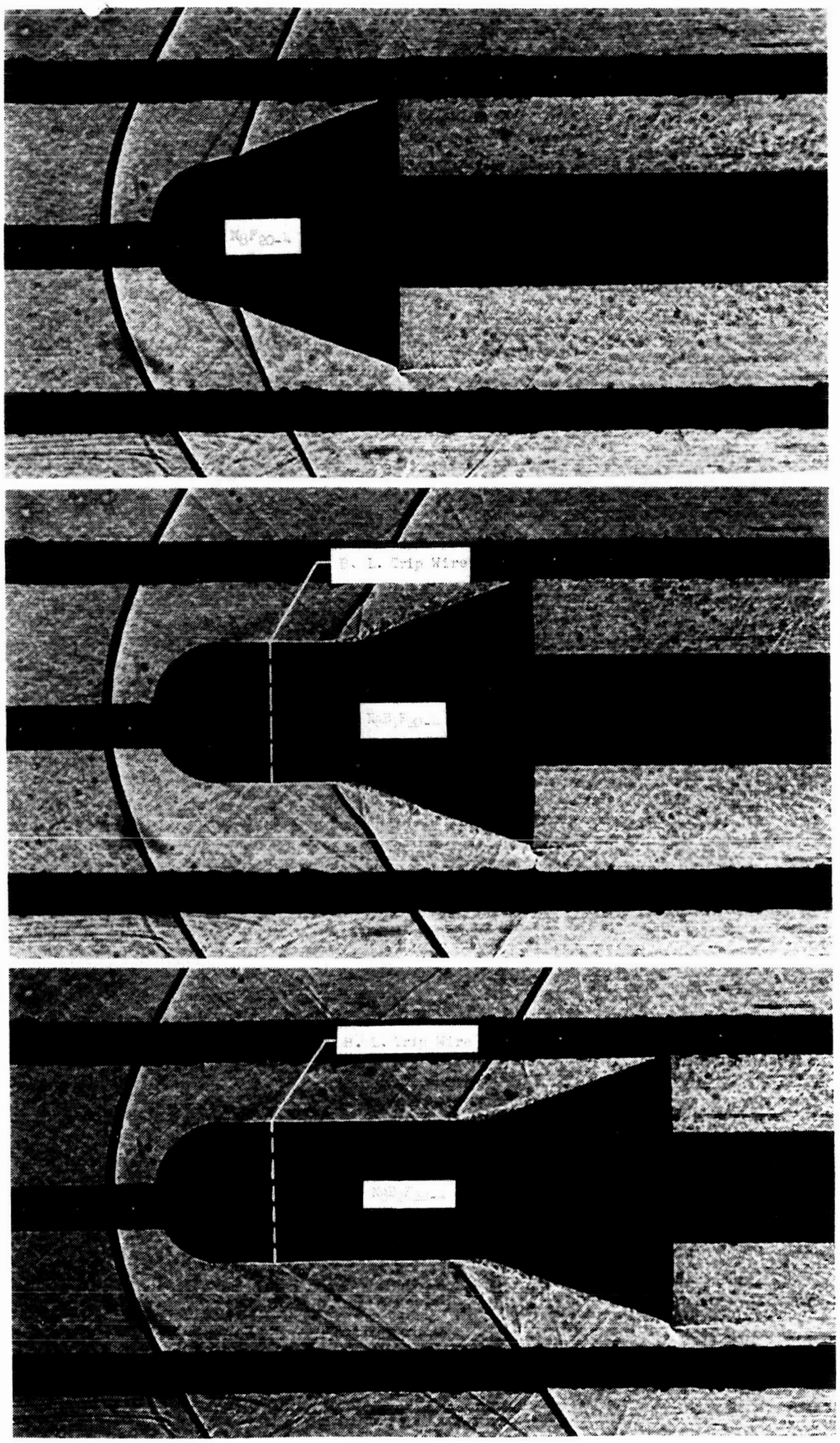


(b) Models with the $N_8$ nose.

Figure 13.- Concluded.